Universitat Autònoma de Barcelona

Doctoral Thesis

Gamma-ray emission of young stellar objects and discovery of superorbital variability at high energies

Author:
Daniela Hadasch

Supervisors:
Prof. Dr. Diego F. Torres
Prof. Dr. Lluis Font Guiteras

A thesis submitted in fulfilment of the requirements for the degree of Doctor of Physics

in the

Universitat Autònoma de Barcelona
Department of Physics

June 2013

Declaration of Authorship

I, Daniela HADASCH, declare that this thesis titled, 'Gamma-ray emission of young stellar objects and discovery of superorbital variability at high energies' and the work presented in it are my own. I confirm that:

- This work was done wholly or mainly while in candidature for a research degree at this University.
- Where any part of this thesis has previously been submitted for a degree or any other qualification at this University or any other institution, this has been clearly stated.
- Where I have consulted the published work of others, this is always clearly attributed.
- Where I have quoted from the work of others, the source is always given. With the exception of such quotations, this thesis is entirely my own work.
- I have acknowledged all main sources of help.
- Where the thesis is based on work done by myself jointly with others, I have made clear exactly what was done by others and what I have contributed myself.

Signed: _____

Date: _____

UAB

Abstract

Department of Physics

Doctor of Physics

Gamma-ray emission of young stellar objects and discovery of superorbital variability at high energies

by Daniela Hadasch

This thesis is structured in three parts: 1.) Observations of binary systems with the Fermi satellite and discovery of superorbital modulation at high energies. 2.) Studies of the so-called magnetars at high and at very high energies and finally 3.) we are giving prospects for the future of the field at very high energies.

Contents

Resumen

Se puede dividir esta tesis en tres partes:

1. **Estudios de la emisión gamma de los sistemas binarios LS I +61°303 y LS 5039 a altas energías con el *Fermi* Large Area Telescope (*Fermi*-LAT) y el primer descubrimiento de variabilidad superorbital a altas energías de la fuente LS I +61°303**

   Los sistemas binarios de rayos gamma son sistemas estelares cuyo espectro tiene su máximo a altas energías (sin tener en cuenta su emisión térmica). Ha sido detectada desde radio hasta rayos gamma (TeV), el sistema binario LS I +61°303 es muy variable en todas las frecuencias. Una característica de la variabilidad de este sistema es la modulación de su emisión a 26.496 días que coincide con su período orbital.

   En esta tesis mostramos por primera vez que la emisión gamma de LS I +61°303 presenta también una variabilidad superorbital con un período de 1667 días. Esta modulación es más presente en fases orbitales alrededor de apastro, aunque no introduce un cambio visible cerca de periastro. Además, se observa una aparición y desaparición de la variabilidad orbital en el espectro de potencias de los datos. Este comportamiento se puede explicar por una evolución cuasi-cíclica del disco ecuatorial de la estrella acompañante (estrella Be) cuyas características influyen en las condiciones para generar rayos gamma. Estos descubrimientos abren por primera vez la posibilidad de usar observaciones de rayos gamma para estudiar los discos de estrellas masivas en sistemas binarios excéntricos.

2. **Estudios de la emisión gamma de magnetares a altas y muy altas energías con el *Fermi*-LAT y con los telescopios Cherenkov MAGIC**

   Los magnetares son una clase particular de estrellas de neutrones que muestran emisión desde radio hasta unos centenares de keV. Se pueden caracterizar por sus explosiones de rayos X y por sus perdidas de energía, las cuales son demasiado pequeñas para justificar su luminosidad en rayos X. Por esta razón, la teoría más aceptada es que la emisión X de la estrella de neutrones está suministrada por el decaimiento y las inestabilidades de sus altos campos magnéticos. En esta tesis, estos objetos han sido estudiados por primera vez a altas y a muy altas energías con el *Fermi*-LAT y con los telescopios MAGIC. Hemos impuesto las primeras cotas a la posible emisión gamma de estos objetos. Además, este fuerte diagnóstico observacional fuerza una revisión del espacio de parámetros aplicable a la visibilidad del modelo de "outer gap" Cheng & Zhang (2001) and Zhang & Cheng (2002) para cada magnetar.

3. **Predicciones para la astronomía Cherenkov con los telescopis CTA**

   La siguiente generación de telescopios Cherenkov será CTA. Este experimento está ahora en la fase de diseño. En esta tesis, evaluamos las capacidades de CTA para estudiar la física no-térmica de sistemas binarios de rayos gamma. Eso requiere la observación de fenómenos a altas energías a tiempos y a escalas espaciales diferentes. Para hacer eso, hemos estudiado los sistemas binarios de rayos gamma en el contexto de la física conocida o esperada de estas fuentes.

   CTA será capaz de demostrar los procesos físicos detrás de la emisión gamma en sistemas binarios con una resolución espectral, temporal y espacial alta. Además crecerá el número de fuentes detectadas significativamente. Hemos observado que la sensibilidad de CTA conseguirá un muestreo de curvas de luz y espectros a escalas de tiempo muy cortas de alta calidad. Además, se podrá monitorear fuentes a tiempo largo usando una parte de los telescopios que todavía alcanzará una sensibilidad 2 o 3 veces mayor que cualquier instrumento actual operando a muy altas energías. En particular, es notable que CTA reducirá la indeterminación de los flujos e índices espectrales en unos cuantos factores.

Summary

This work can be divided into three parts:

1. **Study of the gamma-ray emission of the binary systems LS I +61°303 and LS 5039 at high energies with the *Fermi*-Large Area Telescope (LAT) and the first discovery of superorbital variability at high energies from the source LS I +61°303**

   Gamma-ray binaries are stellar systems for which the spectral energy distribution (discounting the thermal stellar emission) peaks at high energies. Detected from radio to TeV gamma rays, the gamma-ray binary LS I +61°303 is highly variable across all frequencies. One aspect of this system's variability is the modulation of its emission with the timescale set by the 26.496-day orbital period.

   In this thesis we show for the first time that the gamma-ray emission of LS I +61°303 also presents a sinusoidal variability at the known superorbital period of 1667 days. This modulation is more prominently seen at orbital phases around apastron, whereas it does not introduce a visible change close to periastron. It is also found in the appearance and disappearance of variability at the orbital period in the power spectrum of the data. This behavior could be explained by a quasi-cyclical evolution of the equatorial outflow of the Be companion star, whose features influence the conditions for generating gamma rays. These findings open for the first time the possibility to use gamma-ray observations to study the outflows of massive stars in eccentric binary systems.

2. **Study of the gamma-ray emission of magnetars at high and very high energies with the *Fermi*-LAT and the MAGIC Cherenkov telescopes**

   Magnetars are a peculiar class of neutron stars showing emission from radio up to some hundreds of keV. They can be characterized through their bursting behavior and through an energy loss rate, which is too small to power their X-ray luminosity. Therefore, it is believed that the X-ray emission of the neutron star is powered by the decay and the instabilities of their strong magnetic field. In this thesis, these objects are studied for the first time at high and very high energies with the *Fermi*-LAT and the MAGIC telescopes. We put the first constraints on their emission in this high energy regime. Furthermore, this strong observational diagnostic forces a revision of the parameter space applicable for the viability of the outer gap model of Cheng & Zhang (2001) and Zhang & Cheng (2002) to each magnetar.

3. **Prospects for the Cherenkov astronomy with the future Cherenkov Telescope Array (CTA)**

The next generation of Imaging Air Cherenkov Telescopes will be CTA. This experiment is nowadays in the design phase. In this thesis we evaluate the potentialities of CTA to study the non-thermal physics of gamma-ray binaries, which requires the observation of high-energy phenomena at different time and spatial scales. To do so we study gamma-ray binaries in the context of the known or expected physics of these sources.

CTA will be able to probe with high spectral, temporal and spatial resolution the physical processes behind the gamma-ray emission in binaries, significantly increasing as well the number of known sources. We found that the sensitivity of CTA will lead to a very good sampling of light curves and spectra on very short timescales. It will allow as well long source monitoring using subarrays, still with a sensitivity 2-3 times better than any previous instrument operating at VHE energies. In particular, it is noteworthy that CTA will reduce by a factor of a few the errors in the determination of fluxes and spectral indexes.

Chapter 1

High and Very High Energy γ-ray Astrophysics

Astroparticle physics is a relative quite new field that studies elementary particles of astronomical origin and their relation to astrophysics and cosmology. This new interdisciplinary and rapidly expanding area, which combines the experimental techniques and theoretical methods from both astronomy and particle physics, has been named *Astroparticle Physics*.

This work is situated in the field of γ-ray astronomy and the following introductory sections give answers to the questions:

1.1 What are γ-rays?

1.2 How are γ-rays produced?

1.3 Where are γ-rays coming from?

1.1 What are γ-rays?

The earth's atmosphere is permanently impinged by ionizing radiation discovered by the Austrian physicist Viktor Hess in 1912 [Hess 12]. These so-called primary cosmic rays consist of 86 % protons, 11 % α-particles, 1 % heavy nuclei and 2 % electrons. Furthermore, very small fractions of e^+ and $\bar{\mathrm{p}}$ are observed, which originate from interactions of the primary cosmic rays with interstellar gas. Also, neutral particles like ν's, $\bar{\nu}$'s (main sources are the sun and supernova explosions) and γ's (as diffuse galactic emission and emission from point sources, making up a fraction of cosmic rays as small as $<10^{-4}$) are present [Longair 92], [Kneiske 07].

Unlike the charged components of the cosmic radiation, cosmic ray photons are not deflected by magnetic fields and thus point back to their origins. Therefore, the knowledge of the direction of their production sites allows one to profit from them as messenger particles which can be used to study the physical properties of their (partially still enigmatic) sources and the acceleration mechanisms therein.

γ-rays are electromagnetic radiation of very short wavelength of $\lambda < 10^{11}$ m. These high energy photons have energies of more than 1 MeV up to several TeV. The definition of the different energy/wavelength bands of the electromagnetic spectrum is shown in Figure 1.1. This thesis deals with γ-rays in the so-called **H**igh and **V**ery **H**igh **E**nergy (HE and VHE) band, i.e. in the energy range 30 MeV-100 GeV and 100 GeV-100 TeV, respectively.

γ-rays can be detected by

- satellite telescopes and detectors (directly, used in this thesis),
- ground based **I**maging **A**tmospheric **C**herenkov **T**elescopes (IACTs) (indirectly, used in this thesis),
- water Cherenkov tanks (indirectly).

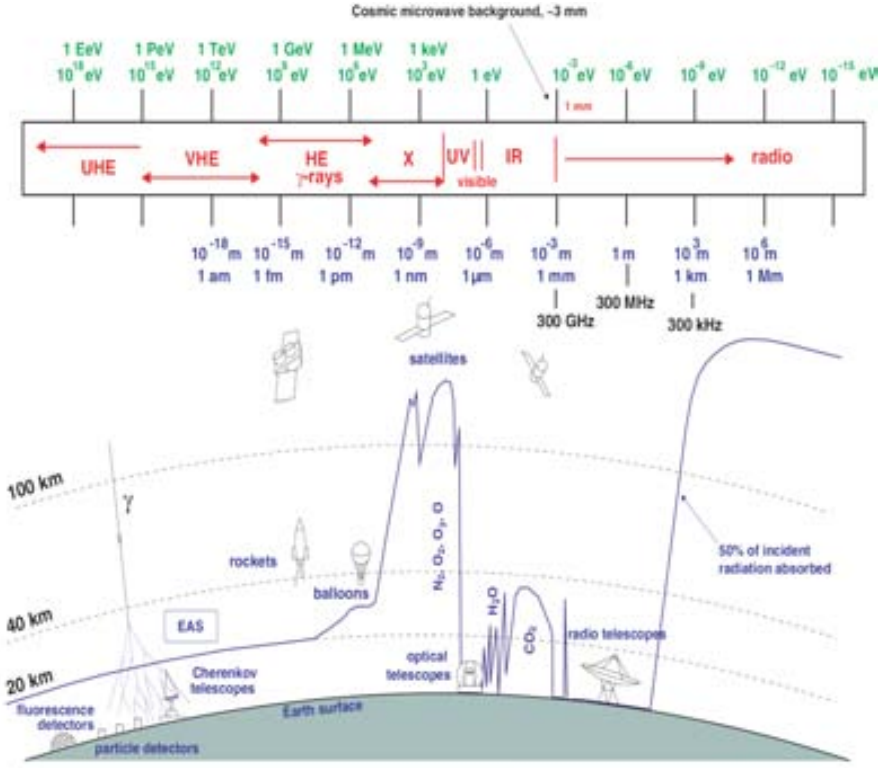

Figure 1.1 Atmospheric windows for electromagnetic radiation to observe the Universe [Longair 92]. Common definitions of the energy bands are written in red. The continuous blue line corresponds to the height, at which a detector can receive half of the total incoming radiation at a given wavelength.

1.2 How are γ-rays produced?

Astronomical objects emit energy in different types of processes. In classical astronomy, particularly in optical observations, the universe turns out to be dominated by thermal radiation which can be described by a blackbody radiation (Planck's formula). Yet,

already in the case of 1 MeV γ-rays, one would need temperatures in the order of $2{\cdot}10^9$ K (for comparison: the sun shows a core temperature in the order of 10^7 K) to explain their emission as thermal process demanding conditions, which could be met only in extreme fireballs (e.g. GRBs, section 1.3). Thus, the emission of γ-rays is dominated by non-thermal processes. The most relevant processes are shown in figure 1.2 and are briefly explained in the following sections. More detailed explanations can be found in [Longair 92], [Aharonian 04] and [Weekes 03].

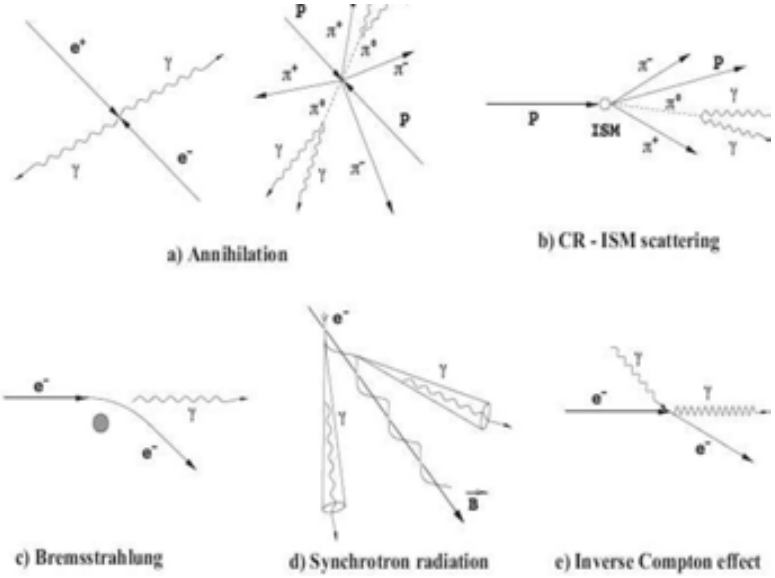

Figure 1.2 Schematic illustration of the main mechanisms of γ-ray production. The **I**nter**S**tellar **M**edium (ISM) or cosmic ray particles can be protons or heavy ions [Longair 92].

Electron-positron annihilation (Figure 1.2a) Wherever electrons e^- locally coexist with their antiparticle, the positron e^+, they rapidly annihilate into two high energy photons:

$$e^+e^- \rightarrow \gamma\gamma \tag{1.1}$$

When emitted at rest, the photons both have an energy of 0.511 MeV. One exciting result of γ-ray astronomy has been the detection of the 0.511 MeV electron-positron annihilation line from the direction of the Galactic Center [Longair 92]. Thermalized positrons interacting with cold electrons can give $3\,\gamma$. Their spectrum appears as a continuum in the MeV range, as described in [Aharonian 81], repeating the spectrum of the parent positrons, but steeper.

π^0 decay (Figure 1.2b) It is the major mechanism by which γ-rays are produced in hadronic interactions. Relativistic protons and nuclei produce high energy γ-rays in inelastic collisions with ambient gas due to the production and decay of secondary pions, kaons and hyperons. The neutral π^0-meson provides the main channel of conversion of the kinetic energy of protons to high energy γ-rays:

$$\pi^0 \longrightarrow \gamma\gamma \qquad (99\,\%) \tag{1.2}$$

$$\pi^0 \longrightarrow e^+e^-\gamma \qquad (1\,\%). \tag{1.3}$$

For the production of π^0-mesons, the kinetic energy of protons should exceed the threshold energy of $E_{\rm th} = 2m_\pi c^2(1+m_\pi/4m_{\rm p}) \approx 280\,{\rm MeV}$, where m_π =134.97 MeV is the mass of the π^0-meson. Neutral pions have a shorter lifetime ($8.4{\cdot}10^{-17}$ s) than charged π-mesons ($\approx 2.6{\cdot}10^{-8}$ s). At high energies, all three types of pions are produced with comparable probabilities. The main decay mode of charged pions is into a muon and its neutrino:

$$\pi^+ \longrightarrow \mu^+\nu_\mu \tag{1.4}$$
$$\pi^- \longrightarrow \mu^-\bar{\nu}_\mu \tag{1.5}$$

The second largest decay mode is into an electron and the corresponding neutrino:

$$\pi^+ \longrightarrow e^+\nu_{\rm e} \tag{1.6}$$
$$\pi^- \longrightarrow e^-\bar{\nu}_{\rm e} \tag{1.7}$$

The neutrino spectrum would be similar to the γ-ray spectrum from π^0-decay. However, at high energies, due to their long life time $\pi^\pm$'s will interact with other hadrons before decaying, which results in a smaller ν flux with respect to γ-rays.

Electron Bremsstrahlung (Figure 1.2c) Charged particles, usually electrons or protons, are accelerated in the electric field produced by a nucleus or ion. The trajectory of the particle is deviated and radiation is emitted. This effect is called *Bremsstrahlung*. It is, together with the pair production, one of the most important phenomena of the production of Cherenkov photons in the atmosphere and an important mechanism for the production of γ-rays within our Galaxy.

Synchrotron Radiation (Figure 1.2d) In the presence of magnetic fields, charged particles emit synchrotron radiation. Synchrotron radiation of accelerated electrons is one of the most important processes in the non-thermal Universe. The energy of the emitted photons has a peak, whose position is proportional to the transverse component of the magnetic field $\rm B_\perp$ and to the Lorentz factor $\gamma_{\rm e}$ of the electron: $E_{\rm max} = 5 \cdot 10^{-9} \cdot B_\perp \gamma^2$. In the context of VHE γ-rays, synchrotron radiation is believed to be the usual process for the generation of the seed photon field for Inverse Compton scattering. However, **U**ltra **H**igh **E**nergy **C**osmic **R**ays (UHECR) (electrons or protons) can emit synchrotron radiation directly in the VHE domain.

Inverse Compton (IC) Scattering (Figure 1.2e) This is the main production mechanism for VHE photons in the astroparticle sources. Relativistic electrons and positrons scatter off low energy photons and transfer parts of their energy to these photons. Depending on the electron-photon energy ratio, one distinguishes three cases to specify the cross-section for the IC-scattering:

$$E_{\rm e}E_\gamma \ll m_{\rm e}^2c^4 : \sigma_{\rm t} = \frac{8}{3}\pi r_{\rm e}^2 \quad \text{(Thomson cross-section)} \tag{1.8}$$
$$E_{\rm e}E_\gamma \approx m_{\rm e}^2c^4 : \sigma_{\rm KN} \quad \text{(exact Klein-Nishina cross-section)} \tag{1.9}$$
$$E_{\rm e}E_\gamma \gg m_{\rm e}^2c^4 : \sigma_{\rm KN} = \pi r_{\rm e}^2 \frac{1}{\epsilon}\left(\ln 2\epsilon + \frac{1}{2}\right),\ \epsilon = \frac{E_\gamma}{m_{\rm e}c^2} \tag{1.10}$$
(Klein-Nishina approximation)

It can be shown that in the latter case, the maximum energy gain for the photons is described by

$$E_{\max} \approx 4\gamma^2 E_\gamma \tag{1.11}$$

with Lorentz factor γ. In the Thomson regime, the emitted photons follow the spectral shape of the seed photons. In the Klein-Nishina regime, the resulting spectrum has a sharp cut-off, which is determined by the maximum energy of the participating electrons.

The hadronic process of π^0 decay and IC scattering are the most important sources of VHE γ-rays. In fact, it is a highly debated issue, which of the two processes is the dominant one. In case of the π^0 decay, this would point to hadronic accelerators and thus explain at least part of the origin of cosmic rays. Observation of VHE neutrinos from the same source would be the unambiguous proof of hadronic production. In case of HE γ-rays, the distinct feature of the π^0-decay γ-ray spectrum is the maximum at $E_\gamma = m_\pi c^2/2 \approx 67.5\,\mathrm{MeV}$. This so-called 'pion-decay bump' was recently detected in two supernova remnants, namely IC 443 and W 44 [Ackermann 13]. In case of IC scattering, leptonic accelerators would be favored, leaving the origin of cosmic rays an open issue.

1.3 Where are γ-rays coming from?

In the first order, there are two kinds of sources: galactic and extragalactic ones. In the following, a brief overview over the known γ-ray sources is given. In Figure 1.3, possible sources are illustrated.

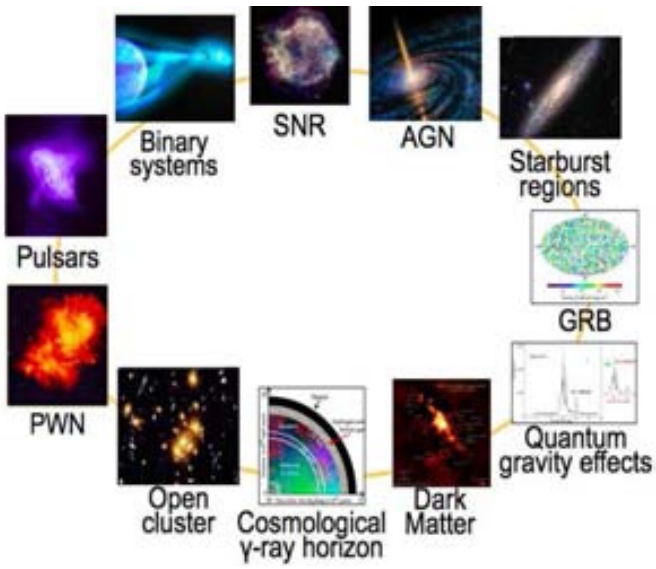

Figure 1.3 Illustration of the main scientific targets of HE and VHE γ-ray astrophysics [Sidro 08].

1.3.1 Galactic Sources

Supernova Remnants

When a star finishes burning its nuclear fuel and its mass is high enough ($> 1.4\,M_\odot$), one possible evolution of the system is related to the non-equilibrium between internal pressure and gravitational potential that makes the star collapse. The result is a huge explosion, the external shells are ejected formig a nebula, while the core becomes a compact object, i.e. a neutron star or a black hole, depending on the initial mass. In contrast to this process, the type Ia supernovae are explosions of white dwarfs in binary systems, where some sort of massaccretion or merging process is at work. Eventually, the white dwarf undergoes a runaway thermonuclear reaction that completely destroys the system.

Pulsars

Pulsars are rapidly-rotating, highly-magnetized *neutron stars* with masses of the order of the solar mass and radii of some ten kilometers. They represent the most dense state of stable matter known in the Universe and are surrounded by a plasma-filled magnetosphere. Pulsars have periods down to milliseconds and have been found to emit electromagnetic radiation in radio through the GeV energy band. It is generally accepted that the primary radiation mechanism in pulsar magnetospheres is synchrotron-curvature radiation. This occurs when relativistic electrons are trapped along the magnetic field lines in the extremely strong field of the pulsar. Secondary mechanisms include ordinary synchrotron and inverse Compton scattering.

Microquasars and Binary Systems

Gamma-ray binaries are binary systems comprised of an young, massive star and a compact object, such as a *black hole* or a *neutron star*. They display non-thermal emission across the electromagnetic spectrum from radio to VHE gamma-rays and their emission, in practically all bands, is modulated with a period equal to the orbital period. The variability of the ambient conditions as the emitter orbits around the young star provides a unique laboratory to test and improve our current understanding of particle acceleration, transport, emission and absorption in relativistic outflows. A deeper description of these systems can be found in Chapter 3.

Pulsar Wind Nebulae

Pulsar **W**ind **N**ebulae - PWN or plerions - are systems created in supernova explosions, in which a fast rotating magnetized neutron star (pulsar), emitting pulsed radiation, is the central object surrounded by the sweeped up material. The rotational energy of the pulsar is converted into a relativistic stream of particles (mostly electrons and positrons). The accelerated electrons of the PWN are an efficient source of VHE γ-rays, by IC upscattering of ambient photons, for example those which were produced by Compton scattering. HE γ-rays can be produced by the same process or through synchrotron radiation. The most famous and best studied PWN is known as the Crab Nebula which,

for its properties of a stable emitting source, is considered the GeV-TeV standard candle for astronomy. It is the first detected VHE source [Kildea 07].

Galactic Center

The Galactic center has been found to emit steady VHE γ-ray signal up to 30 TeV as reported by the CANGAROO [et al 04], H.E.S.S. [Aharonian 06], VERITAS [Kosack et al 04] and the MAGIC [et al 06] collaborations. It is very difficult to interpret the emission mechanisms since the region is packed with different potential sources and the angular resolution of the current instruments is insufficient to disentangle the exact location of the VHE γ-ray emission. Most probable scenarios involve emission due to a pulsar wind nebula or a close-by supernova remnant. More exotic scenarios include the central black hole as an accelerator or even annihilation of dark matter particles to reproduce the observed signal [Horns 05].

1.3.2 Extragalactic Sources

Starburst Galaxies

Star**B**urst **G**alaxies (SBG) are known for their extraordinary high **S**tar **F**omation **R**ate (SFR), which is highest near the core of these galaxies. The high SFR is triggered by an extraordinary high rate of supernova explosions (about ten times higher than that of normal galaxies). SBGs are identified by their high luminosity in the infrared and their extended emission regions in the radio and X-ray bands. The infrared emission comes from dust in the hot interstellar medium where the stars are forming. The enhanced rate of supernova explosions indicates that the cosmic ray density is greater and therefore, that they are detectable γ-ray sources [**?**].

Gamma Ray Bursts

Gamma **R**ay **B**ursts (GRB) are the most luminous emissions in the Universe in any wavelength band. It is believed that they are flashes of γ-rays coming from random directions at cosmological distances. During their short *life time* (from tens of milliseconds to few hundred seconds) the γ-ray emissions can be stronger than any other known γ-ray source, with a large variety of temporal profiles and emission spectra. The origin of the enigmatic GRBs is still under debate, even three decades after their discovery.

Active Galactic Nuclei

Active **G**alactic **N**uclei (AGN) represent a large population of compact extragalactic objects characterized with extremely luminous electromagnetic radiation produced in very compact volumes. At the center of the galaxy, there is a **S**uper**M**assive **B**lack **H**ole (SMBH) ($\sim 10^6$ to $\sim 10^{10}\,M_\odot$) the gravitational potential energy of which is the ultimate source of power of the system released in different forms - through the thermal emission of the accretion disk, as well as through non-thermal processes in the relativistic jets

that emanate perpendicular to the plane of the accretion disc. Particle acceleration takes place throughout the entire jet extending up to 10^{24} cm, i.e. well beyond the host galaxy. These particles interact with the ambient photons and magnetic fields and thus result in non-thermal (synchrotron and IC) emission components observed on different (sub-pc, kpc, and multi-hundred kpc) scales. Broad emission lines are produced in clouds orbiting above the accretion disc. They are located typically within the zone between 0.01 to 0.1 pc. The accretion disk and the broad-line region is surrounded by a thick dusty torus. Narrow emission lines are produced in clouds located much farther from the central engine, typically between 0.3 and 30 pc [Aharonian 04]. The production process of HE and VHE γ-rays is under debate: both leptonic and hadronic models seem to be able to describe the observational data well.

The distribution of all these sources detected at VHE energies are shown in Figure 1.4. In Figure 1.5 the sky seen with the *Fermi* Large Area Telescope above > 1 GeV after 4 years is presented. The dominant feature there is diffuse emission associated with the structure of the Milky Way. In the bottom plot of Figure 1.5 the fractions of the different sources are shown. More than half of the sources above 10 GeV are black-hole-powered active galaxies. More than a third of the sources are completely unknown, having no identified counterpart detected in other parts of the spectrum.

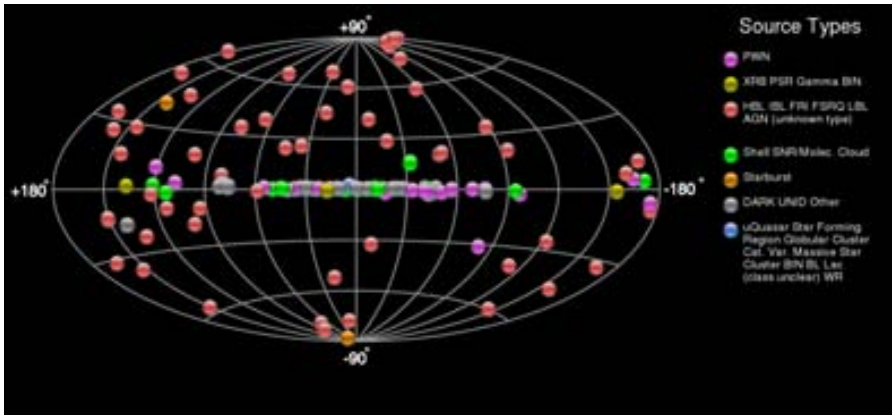

Figure 1.4 Sky map of all 145 detected VHE sources up to now [Wakely 13].

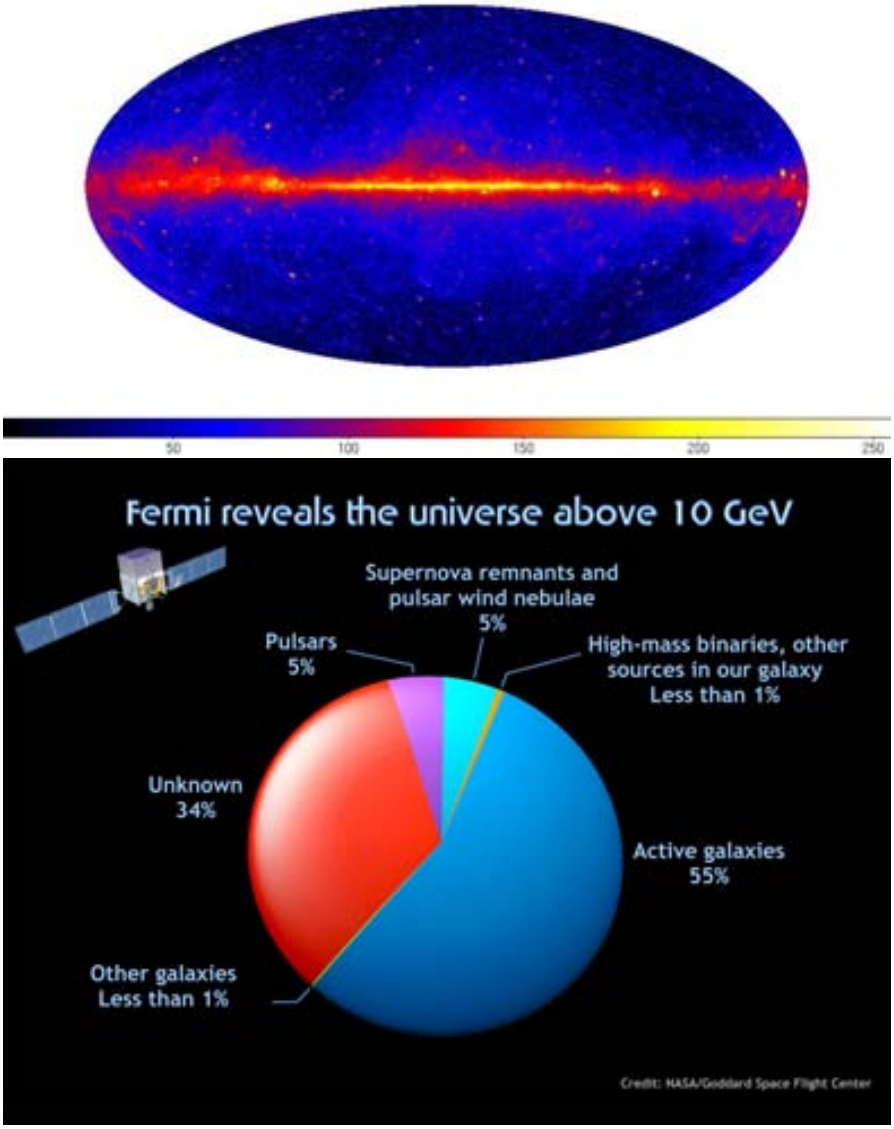

Figure 1.5 *Top:* All-sky image as seen with the *Fermi*-LAT after 4 years of data taking. All energies $> 1\,\mathrm{GeV}$ are included. The units are counts/pixel. Courtesy Seth Digel. *Bottom:* Distribution of the detected sources with the *Fermi*-LAT.

Chapter 2

High and Very High Energy γ-Ray Detection

AGILE

REFERENCE HESS, VERITAS (web pages)

The total electromagnetic spectrum cannot be observed directly from earth. In reality, it is only possible in two small detection windows, the optical and the radio (Figure 1.1). This is due to the fact, that the earth's atmosphere is transparent in these two windows only. It blocks all electromagnetic radiation of energies greater than 10 eV [Weekes 03].

One of the techniques to bypass this fact is the so-called Atmospheric Cherenkov technique that will be described in Section 2.1. With ground-based **I**maging **A**tmospheric **C**herenkov **T**elescopes (IACTs) a γ-ray window from about 100 GeV to 50 TeV can be explored. In this thesis data from the MAGIC experiment are used, which is shortly introduced in Section 2.1.1.

With space techniques, rockets, balloons and satellites, the detection window can be enlarged, too. The energy range from 20 GeV to 300 GeV is covered by one of the current instruments in orbit: the *Fermi* **L**arge **A**rea **T**elescope (*Fermi*-LAT). Data from this instrument are used in the framework of this thesis. The detection principle is described briefly in Section 2.2 and in Section 2.2.1 the *Fermi*-LAT is introduced.

2.1 Imaging Air Cherenkov technique

The Earth's atmosphere blocks all electromagnetic radiation that is more energetic than ultraviolet photons. To study higher energetic radiation we have to go to space to detect these γ-rays directly, but at energies above ~ 100 GeV neither this is an efficient option anymore since the fluxes are too small for the typical detection areas of satellites ($\leq 1m^2$). For example, for the strongest TeV source, the Crab Nebula, we would detect ~ 5 photons per year per square meter. Therefore, we have to come back to earth and use the whole atmosphere as an detector. This works in the following way.

A VHE primary **C**osmic **R**ay (CR) particle impinging on the earth's atmosphere interacts with the nuclei of the atmosphere's molecules at a height of typically 20-25 km

above sea level, depending on the energy of the CR particle. This primary particle iniciates the development of an **E**xtended **A**ir **S**hower (EAS), which can be induced by a γ-ray, an electron or a hadron. For the electromagnetic case - iniciated by a γ-ray or an electron - the three relevant processes are pair production, Bremsstrahlung and photoproduction where secondaries are produced. Is the shower iniciated by a charged cosmic ray it is dominated by hadronic interactions like pion and meson production, leading to a much larger transverse momentum. Furthermore, it has a wider lateral distribution and a more irregular spread than the electromagnetic shower. In Figure 2.1 sketches of γ-ray and hadron induced EASs are shown where this difference can be seen. This important fact is used in the data analysis in order to separate γ-ray induced showers from hadronic showers. IACT experiments are highly background dominated. On one γ-ray there come ~ 1000 hadronic particles making hadron-induced showers the main source of the background.

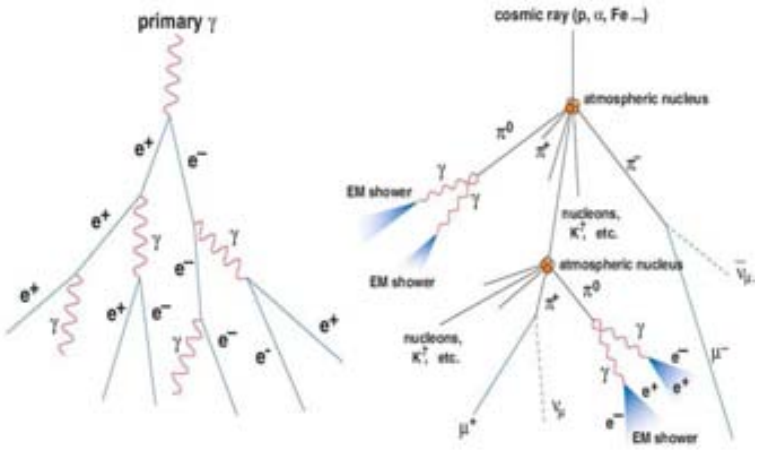

Figure 2.1 Sketch of the development of an EAS induced by a γ-ray *(left)* and by a charged cosmic nucleus *(right)* [Sidro 08].

Since the CR does not survive on its own in any case, we detect with ground-based detectors the Cherenkov light produced during the interaction of the secondary products with the atmosphere. When a particle moves in a dielectric medium at a velocity, which exceeds the speed of light in the medium, it produces Cherenkov light. Because of absorption and scattering in the atmosphere, the Cherenkov light arrives at the ground with a spectrum that peaks at wavelengths around 300-350 nm [Aharonian 04]. This light is very faint, with a density ranging from 100 to several 100 photons/m^2 (depending on the altitude) for a 1 TeV γ-ray photon. The Cherenkov light flashes produced by EAS are very brief, typically a few nsec.

The very faint Cherenkov light implies that the Cherenkov telescopes must have large optical reflectors to image the Cherenkov light onto a multi-pixel camera. The latter should be sensitive to the visible (closer to blue) light and the readout has to be sufficiently fast. Current instruments have reflection areas in the range of $\sim 150 - 600$m^2. In the MAGIC experiment, for example, the integration window of the signal accounts for 3 nsec, and the signal is sampled with 2 Gsamples per second, i.e. 6 times in this time interval.

There are three features which comprise the basis of an **I**maging **A**tmospheric **C**herenkov **T**elescope (IACT). These features are demonstrated in a characteristic image of a γ-ray induced shower obtained with an IACT camera (Figure 2.2):

- the total intensity of the image is a measure of the primary energy;
- the orientation of the image in the camera correlates with the arrival direction of the primary particle;
- the shape of the image contains information about the origin of the air shower (induced by a cosmic ray proton/ nucleus or by a γ-ray photon).

Photon positions on the camera correspond to directions of the incident Cherenkov photons. For a γ-initiated shower, whose axis is usually parallel to the telescope axis, photons emitted high in the atmosphere are reflected close to the camera center, while the shower tail image extends towards the camera edges. The quantity of collected light is then correlated in first order to the number of particles producing Cherenkov light of the EAS, falling inside the **F**ield **O**f **V**iew (FOV) of the camera.

Besides doing the background suppression based on different shape of the shower and also a different development in time, background suppression can be done on the trigger level very efficiently having several telescopes. The same shower is seen by various telescopes and only coincident events are selected. This also leads to a reduced energy detection threshold. Furthermore, the angular resolution improves leading to a more precise reconstruction of the direction of the primary particle. In Figure 2.3 the concept of stereoscopic observations is shown as well as the development of an electromagnetic and a hadronic cascade.

In this figure it can also be seen that the radius of the Cherenkov light pool on the ground is in the order of 100 m. Within this radius, the light pool is rather uniformly illuminated. As long as a Cherenkov detector is located somewhere in the Cherenkov light pool, it can detect the event. Therefore, a single Cherenkov detector can detect Cherenkov light from EAS of up to ~ 120 m impact distance. As a result, such a detector can have an effective collection area in the order of 10^4 m^2, which is much higher than for typical satellite-born instruments.

2.1.1 Current IACT experiments

Present instruments in the field of ground-based γ-ray astronomy are sensitive to photons with energies above $\sim$ 50-100 GeV. The pioneering experiment in this field was the Whipple telescope [Kildea 07], which in 1989 detected the first γ-ray signal from the Crab Nebula. Significant improvements afterwards achieved by HEGRA [Daum 97] through the introduction of stereoscopy, i.e. the simultaneous imaging of the same shower with multiple Cherenkov telescopes.

At the moment, there are three big IACT experiments running all over the world. The VERITAS (**V**ery **E**nergetic **R**adiation **I**maging **T**elescope **A**rray **S**ystem) experiment has an array of four 12 m optical reflectors and is located in Arizona. Since 2003, the H.E.S.S. (**H**igh **E**nergy **S**tereoscopic **S**ystem) experiment located in Namibia is in operation, consisting of four single 13 m diameter telescopes. In 2012 this array was

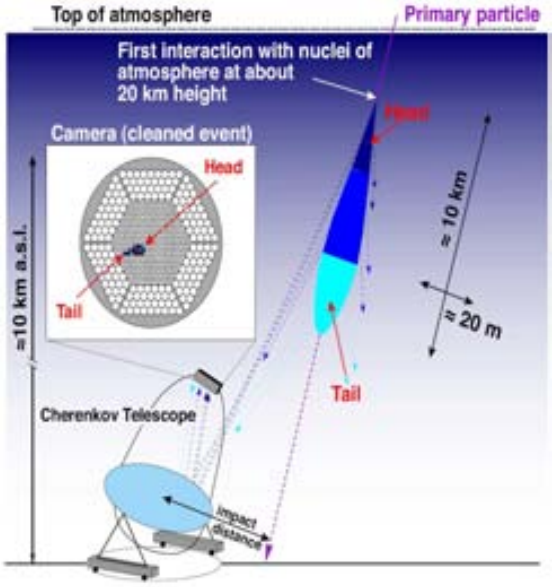

Figure 2.2 A schematic view on the isogonal image of an extended air shower by using its Cherenkov light. The air shower is approximated by a light cylinder. The image in the camera has an elliptical shape with a certain semi-major and semi-minoraxis. The so-called *head* and *tail* of the shower are mapped into the camera image [Mazin 07].

upgraded with a much larger fifth telescope of 28 m diameter and operates since then as H.E.S.S. II.

In the framework of this thesis data from the MAGIC (**M**ajor **A**tmospheric **G**amma-ray **I**maging **C**herenkov) experiment are used. The MAGIC Collaboration operates two 17 m diameter imaging atmospheric Cherenkov telescopes (the MAGIC Florian Goebel Telescopes) at the Roque de los Muchachos (2200m a.s.l.) on the Canary Island of La Palma. The first telescope was built in 2004 and operated in standalone mode until 2009. Then a second MAGIC telescope at a distance of 85 m from the first one was built. From then on they constitute the MAGIC telescope stereoscopic system, which is sensitive to γ-rays with energies from 50 GeV (with a special trigger setup from 25 GeV) up to 30 TeV. The aim of this project was to achieve the lowest energy threshold among all IACTs of the third generation and the possibility to move the telescope within seconds to any sky position. The latter is needed to quickly react on Gamma Ray Burst alerts and point the telescope as fast as possible to the sky position of a burst. To reach this aim, the mirrors are mounted on a light weight space frame structure made of carbon fiber reinforced plastic tubes ($\sim$5 tons). Due to this light weight construction, the MAGIC telescopes can be repositioned in any direction within less than 30 seconds. In Figure 2.4 a picture of the two telescopes with the counting house in the center, where the readout electronic is hosted, is shown. Details on the performance of the telescopes can be found in [Albert 08] and [Aleksić 12].

The current IACTs will be in operation at least for two to five years more, until the future generation of IACTs comes. This will be the **C**herenkov **T**elescope **A**rray (CTA), which is introduced in Chapter5.

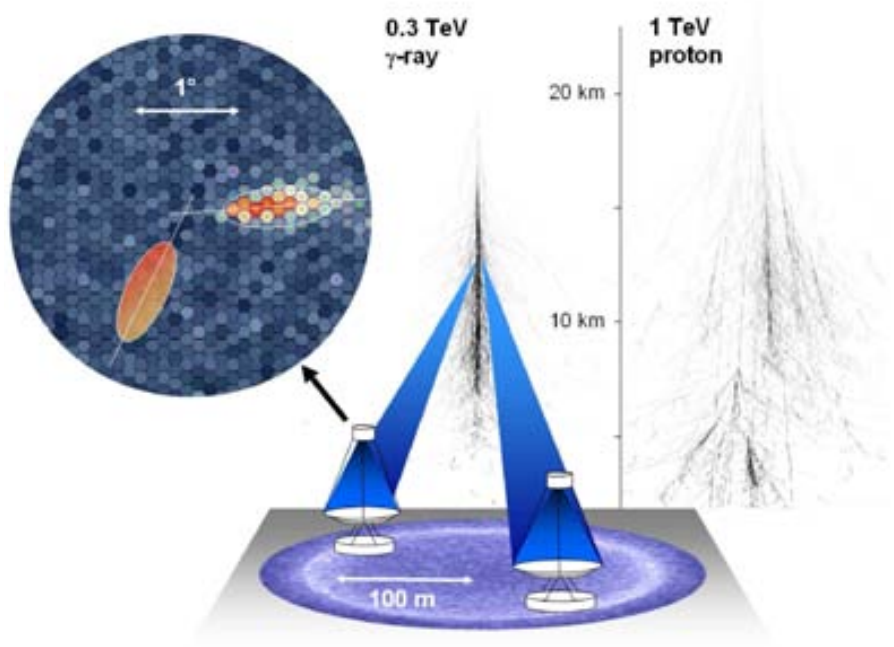

Figure 2.3 Sketch of the principle of stereoscopic observations. Represented is the development of an EAS initiated by an 0.3 TeV γ-ray and the corresponding image seen by both telescopes superposed in one camera. Like this the direction of the primary particle can be determined. On the right the development of a hadronic cascade induced by an 1 TeV proton is shown for comparison [Hinton 09].

2.2 Principles of a pair conversion telescope

As mentioned above, one possibility to detect radiation with energies higher than that of ultraviolet photons, is to go to space, where we do not have any absorption through the atmosphere. Pair conversion telescopes are the prefered technique for the MeV-GeV energy range since pair production is the dominating photon interaction process for energies higher than 10 MeV. The principle of this technique is to force the γ-ray to interact with matter and to produce an $e^+ - e^-$ pair. The measurement of the direction and energy of the electron and of the positron allows to reconstruct the direction and energy of the original photon; furthermore the topology of the process provides a clear signature for background rejection. Of course, the produced electrons themselves can produce photons through Bremsstrahlung via interaction with nuclear Coulomb fields. As long as the nextgeneration particles remain well above the pair-production threshold - in the case of photons - or critical energy - in the case of electrons -, the shower continues to develop exponentially. Figure 2.5 shows a schematic view of a pair conversion telescope. The following three main components are shown there:

- Anticoincidence shield: for identifying and rejecting the background due to cosmic rays which typically outnumber the γ-rays by up to 5 orders of magnitude.
- Tracker/ Converter: consisting of high Z material in which γ-rays can convert into an $e^+ - e^-$ pair interleaved with position sensitive detection planes, that record the

Figure 2.4 The two MAGIC telescopes located on La Palma. Courtesy D. Mazin.

passage of charged particles, thus measuring the tracks of the particles resulting from pair conversion.

- Calorimeter: measuring the energy deposition due to the electromagnetic particle shower that develops from the incident charged particles, which result from pair conversion in the tracker.

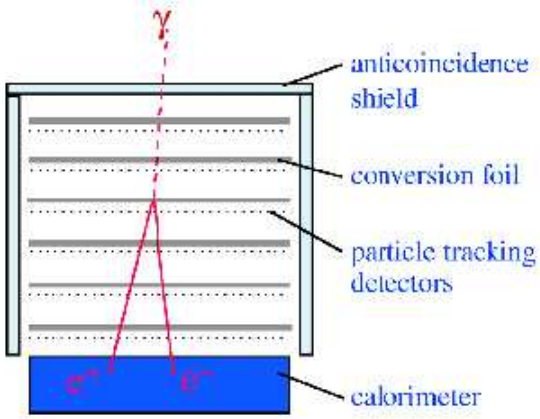

Figure 2.5 Diagram of a pair-production telescope showing an incident gamma-ray entering the telescope. Image credit: NASA/Sonoma State University/Aurore Simonnet

2.2.1 Current instruments

One of the current instruments in orbit is the AGILE (Astro-rivelatore Gamma a Immagini LEggero) satellite. Launched in 2007, it is sensitive in the gamma-ray energy range 30 MeV-30 GeV with a monitor in the X-ray band 18-60 keV. It is operating in a low inclination (2.5°) low-Earth orbit at 540 km altitude. The AGILE Gamma-Ray Imaging Detector (GRID) is a pair- tracking telescope based on a tungsten-silicon tracker.

In this work we are using data taken with the second experiment in orbit, the *Fermi* satellite. The *Fermi* satellite was launched in June 2008 into a circular orbit at 565 km altitude (96 min period) and 25.6° inclination with respect to the Earth's equatorial plane. In August 2008 the LAT started to take scientific data in survey mode. In this mode, the observatory is rocked north and south on alternate orbits to provide a more uniform coverage, so that every part of the sky is usually observed for ∼30 minutes every ∼3 hours. The satellite has two instruments on board:

- the **G**amma-ray **B**urst **M**onitor (GBM) sensitive in the energy range from a few keV to ∼ 30 MeV and
- the **L**arge **A**rea **T**elescope (LAT) sensitive to photons from ∼20 MeV to >300 GeV.

With the GBM one of the key scientific objectives of the mission, the determination of the high-energy behavior of gamma-ray bursts and transients can be ensured. All data presented in this work are coming from the LAT, the main instrument based on solid-state technology, obviating the need for consumables and greatly decreasing instrument dead-time. It is an electron-positron pair production telescope, as described above. The converter features 16 foils of heavy material (tungsten) interleaved with solid state silicon trackers. The calorimeter is important to measure the energy deposition of the $e^+ - e^-$ pairs and to generate an image of the cascade profile and measure the shown maximum to provide a very important background discriminator and an estimator of the electromagnetic cascade fluctuation. It consists of CsI(Tl) crystals read by photodiodes. The Anticoincidence Detector is composed by 89 tiles of plastic scintillator tiles. Each tile is read by means of two wavelength-shifting fibers interleaved in it by two photomultiplier tubes. As shown in Figure 2.6, the LAT consists of an array of 16 towers with the trackers/converters and the calorimeter modules mounted in a 4×4 mass alluminium Grid structure, surrounded by a segmented anticoincidence detector, a thermal blanket and a micro-meteor shield. It has a large ∼2.4 sr field of view (at 1 GeV) and an effective area of ∼8000 cm^2 for energies >1 GeV after event reconstruction and background rejection. A more detailed description of the *Fermi* -LAT can be found in [Atwood 09].

The *Fermi*-LAT is at the moment the only existing satellite covering the energy range from tens of MeV up to some hundreds of GeV. After this mission, which will take some more years depending on the funding, we will be blind to the sky at this energy range, since no successor will come that soon.

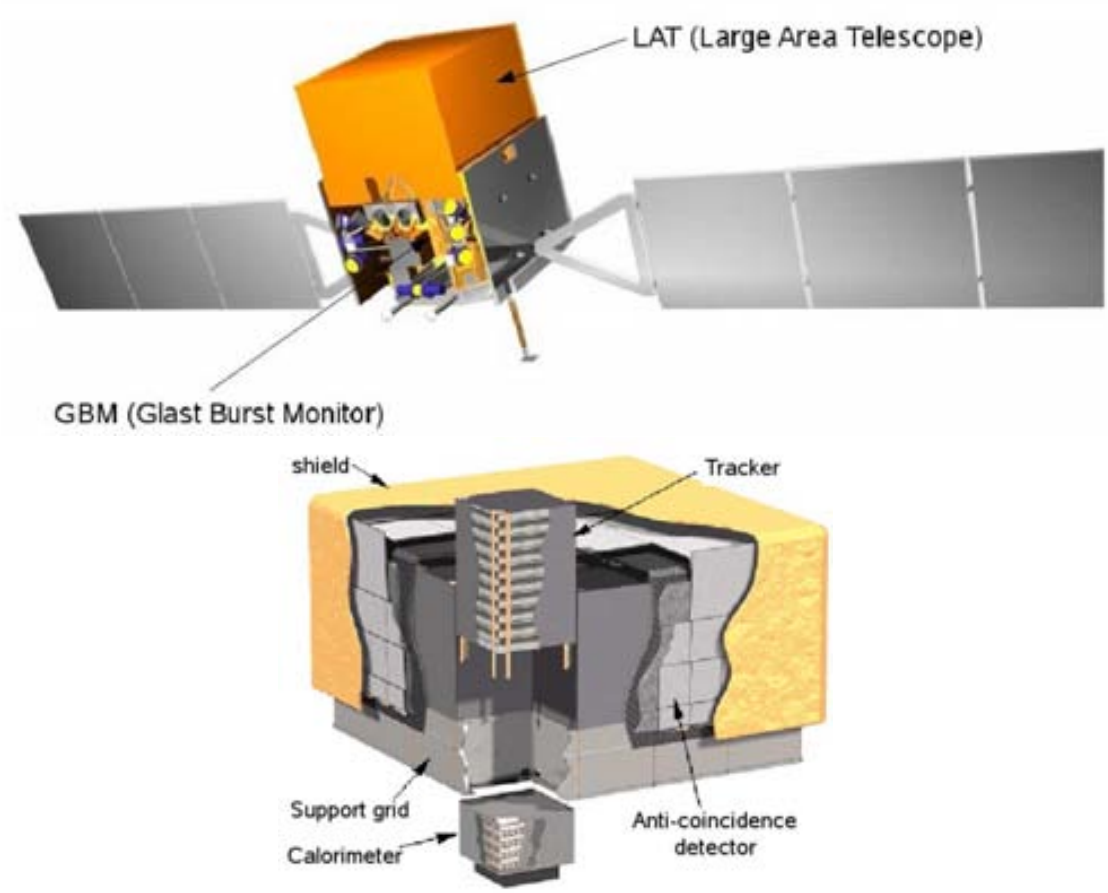

Figure 2.6 *top:* Schematic view of the *Fermi* spacecraft with both the Large Area Telescope (LAT) and the GLAST Burst Monitor (GBM) are shown. *Bottom:* LAT modular structure.

Chapter 3

PART I: Gamma-ray binaries

CITATIONS TO BE CONVERTED INTO BIBTEX!!! FIGURES AND TABLE TO BE ADJUSTED

3.1 Overview and Motivation

From the known 114 **H**igh **M**ass **X**-ray **B**inaries (HMXBs) (Liu et al. 2006) with O/B stars in sky, we only know 5 of them as γ-ray binaries. These systems emit their largest part of the luminosity (discounting the thermal stellar emission) at high ($\geq$100 MeV), gamma-ray energies (see e.g., [**?** **?**]), being therefore a member of the class of gamma-ray binaries.

- LS I +61°303
- LS 5039
- PSR B1259−63
- 1FGL J1018.6−5856
- HESS J0632+057
- Cyg X-3

Table 3.1 Known HMXBs and their characteristics

	LS I +61°303	LS 5039	PSR B1259−63	1FGL J1018.6−5856	HESS J0632+057	Cyg X-3
Orbital period	26.5 days	3.9 days	3.4 years	16.6 days	321 days	4.8 hrs
Star type	Be star	O star	Be star	O star	Be star	Wolf-Rayet s
Compact object	unkown	unknown	pulsar (48 ms)	unknown	unknown	Likely black h
Distance (kpc)	2.0 kpc	2.5	2.3	5.4	1.5	∼7
Eccentricity	0.54	0.35	0.87	unknown	0.83	unknown
Persistent/ Transient	Persistent	Persistent	Transient	Persistent	?	Transient
GeV emission	yes	yes	yes	yes	no	yes
TeV emission	yes	yes	yes	no (?)	yes	no

Cygnus X-1 just hint of flare with MAGIC observations. But recently Fermi detection, doubtful... Cygnus X-3 flaring in GeV, no detection in MAGIC (cite) HESS J0632+057 seen by MAGIC and VERITAS triggered through flare, only upper limits at GeV (paper in prep.) 1FGL J1018.6−5856 first gamma-ray binary discovered through GeV observations, later also seen in radio. Counterpart seen with H.E.S.S.? (cite Emma talk from barcelona workshop) PSR B1259−63 seen at GeV and TeV when compact object passes disc LS 5039 copy from paper LS I +61°303 copy from paper and a bit more. LS I +61°303 is one of the few x-ray binaries that have been detected from radio to TeV gamma rays (see [**?**] and references therein). It is perhaps the most intriguing one due to the high variability and richness of its phenomenology at all frequencies. LS I +61°303 consists of a Be star of approximately 10 solar masses, and a compact object. Be stars are rapidly rotating B-type stars showing hydrogen Balmer lines in emission in the stellar spectrum, and which lose mass to an equatorial circumstellar disc. The nature of the compact object in LS I +61°303 has been much debated over the past few years. Pulsar wind interaction (see e.g., [**?** **?** **?** **?**]) and microquasar jets (see [**?**] for a review) have been proposed as the origin of the non-thermal emission. The recent detection of two short (< 0.1 s), highly-luminous ($> 10^{37}$ erg s^{-1}), thermal flares [**?**] have given support to the hypothesis that the compact object in LS I +61°303 is a neutron star, for only highly-magnetized neutron stars have been found to behave in this way.

To date there are only a handful of X-ray binaries that have been detected at high (HE; 0.1–100 GeV) or very high-energies (VHE; >100 GeV): LS I +61°303 [**?** **?** Abdo 09], LS 5039 [**?** **?**], PSR B1259−63 [**?** **?**], Cyg X−3 [**?**], Cyg X−1 [**?** **?**]. Recently, two new binaries were found: 1FGL J1018.6−5856, with a period of 16.6 days found in the GeV regime [**?**] and HESS J0632+057 [**?** **?** **?**], for which a period of ∼320 days was detected in X-rays (Bongiorno et al. 2011). Of these sources only LS I +61°303, LS 5039 and PSR B1259−63 share the property of being binaries detected at both GeV and TeV energies. The other systems have been unambiguously detected only in one band, either at GeV or at TeV, see, e.g., the case of Cyg X−3 in **?**]. In the case of Cyg X−1, with the hint of TeV detection itself being at the level of 4 standard deviations (4σ), claims of detection at GeV energies by the Astrorivelatore Gamma a Immagini Leggero (AGILE) remain uncertain with concurrent *Fermi* Large Area Telescope (LAT) observations [**?**]. It is yet uncertain whether these spectral energy distribution (SED) differences reflect an underlying distinct nature, or are just a variability signature in different bands.

The nature of the binary compact object in LS I +61°303, LS 5039 , HESS J0632+057 and 1FGL J1018.6−5856 is as yet undetermined [**?**]. Both neutron star (e.g. PSR B1259−63) and probable black hole (e.g. Cyg X−3) binary systems have been detected at GeV energies and so both types of compact object are viable in the undetermined systems. Recently the Burst Alert Telescope (BAT) onboard Swift reported a magnetar-like event which may have emanated from LS I +61°303 [**?** **?**]. If true this would be the first magnetar found in a binary system.

3.2 2.5 years monitoring of LS 5039 and LS I +61°303 with the *Fermi* Large Area Telescope

The *Fermi* Large Area Telescope (LAT) reported the first definitive GeV detections of the binaries LS I +61°303 and LS 5039 in the first year after its launch in June, 2008. These detections were unambiguous as a consequence of the reduced

positional uncertainty and the detection of modulated γ-ray emission on the corresponding orbital periods. An analysis of new data from the LAT, comprising 30 months of observations, identifies a change in the γ-ray behavior of LS I +61°303. An increase in flux is detected in March 2009 and a steady decline in the orbital flux modulation is observed. Significant emission up to 30 GeV is detected by the LAT; prior datasets led to upper limits only. Contemporaneous TeV observations no longer detected the source, or found it -in one orbit- close to periastron, far from the phases at which the source previously appeared at TeV energies. The detailed numerical simulations and models that exist within the literature do not predict or explain many of these features now observed at GeV and TeV energies. New ideas and models are needed to fully explain and understand this behavior. A detailed phase-resolved analysis of the spectral characterization of LS I +61°303 in the GeV regime ascribes a power law with an exponential cutoff spectrum along each analyzed portion of the system's orbit. The on-source exposure of LS 5039 is also substantially increased with respect to the prior publication. In this case, whereas the general γ-ray properties remain consistent, the increased statistics of the current dataset allows for a deeper investigation of its orbital and spectral evolution. The following chapter is based on the work [Hadasch 12].

3.2.1 The observed sources

The early LAT reports of GeV emission from LS 5039 and LS I +61°303 were based upon 6–9 months of survey observations [Abdo 09**?**]. Both sources were detected at high significance and were unambiguously identified with the binaries by their flux modulation at the corresponding orbital periods, 26.4960 days for LS I +61°303 [**?**] and 3.90603 days for LS 5039 [**?**]. The modulation patterns were roughly consistent with expectations from inverse Compton scattering plus γ-γ absorption models, and were anti-correlated in phase with pre-existing TeV measurements [e.g., **?** **?**]. The anti-correlation of GeV–TeV fluxes is in fact a generic feature of these models, where the GeV emission is enhanced (reduced) when the highly relativistic electrons seen by the observer encounter the seed photons head-on (rear-on); [e.g., see **?** **?** **?** **?**]. *Fermi*-LAT measurements provided a confirmation of these predictions.

The spectra of both sources were best modeled with exponential cutoffs in their high-energy spectra, at least along part of the orbit. Specifically, an exponential cutoff was statistically a better fit to the SED compared with a pure power law at phases surrounding the superior conjunction (SUPC) of LS 5039 and in the orbitally averaged spectrum of LS I +61°303. Statistical limitations of the data prevented the determination or the ruling out of an exponential cutoff in any part of the orbit of LS I +61°303 or in the inferior conjunction (INFC) of LS 5039 . The spectral energy distributions with the exponential cutoffs that were reported were reminiscent of the many pulsars the LAT has detected since launch [**?**], although this was far from a proof of their pulsar nature. To date no pulsations have been found at GeV energies, or at any other wavelengths, despite deep dedicated searches (see e.g., Rea et al. 2010, 2011).

Since *Fermi* was launched, both the Major Atmospheric Gamma-ray Imaging Cherenkov Telescopes (MAGIC) and the Very Energetic Radiation Imaging Telescope Array (VERITAS) have performed observations of LS I +61°303. No TeV detection was reported after October 2008, until the source unexpectedly reappeared, once, at periastron [**?** **?**]. At the same time, a hard X-ray multi-year analysis [**?**] and a long-term X-ray campaign on LS I +61°303 using the *Rossi X-ray Timing Explorer (RXTE)* has been conducted covering the whole extent of the LAT observations [see **?** **?**]. In addition, simultaneous

and archival data from long-term monitoring of radio and Hα emission is available for comparison in a multi-wavelength context. In this work the results of the analysis of 30 months of LAT survey observations of both LS I +61°303 and LS 5039 are presented. The long-term flux variations of the sources, as well as variations in the amplitude of their orbital flux modulation are investigated. The possible spectral variability for both systems are explored and finally these observations are interpreted in the context of the source behavior at other frequencies.

3.2.2 Analysis settings

The data were reduced and analyzed using the Fermi Science Tools v9r20 package[1]. The standard onboard filtering, event reconstruction, and classification were applied to the data [Atwood 09]. The high-quality "diffuse" event class was used together with the "Pass 6 v3 Diffuse" instrument response functions (IRFs). Time periods when the target source was observed at a zenith angle greater than 105° were excluded to limit contamination from Earth limb photons. Where required in the analysis, models for the Galactic diffuse emission (*gll_iem_v02.fit*) and isotropic backgrounds (*isotropic_iem_v02.txt*) were used[2].

3.2.3 Spectral analysis methods

The binned maximum-likelihood method of `gtlike`, included in the ScienceTools, was used to determine the intensities and spectral parameters presented in this paper. We used all photons with energy >100 MeV in a circular region of interest (ROI) of 10° radius centered at the position of LS I +61°303 and LS 5039 , respectively. For source modeling, the 1FGL catalog [**?**], derived from 11 months of survey data, and the first *Fermi* pulsar catalog [**?**] were used; all sources within 15° of the ROI center were included. The energy spectra of point sources included in the catalog within our ROI are modeled by a simple power law,

$$\frac{\mathrm{d}N}{\mathrm{d}E} = N_0 \left(\frac{E}{E_0}\right)^{-\Gamma} \tag{3.1}$$

with the exception of known γ-ray pulsars, which were modeled by power laws with exponential cutoffs described by:

$$\frac{\mathrm{d}N}{\mathrm{d}E} = N_0 \left(\frac{E}{E_0}\right)^{-\Gamma} \exp\left[-\left(\frac{E}{E_{\mathrm{cutoff}}}\right)\right]. \tag{3.2}$$

The spectral parameters were fixed to the catalog values except for the sources within 3 degrees of the candidate location. For these latter sources, the flux normalization was left free. All of the spectral parameters of the two subject binaries were left free for the fit. Source detection significance is determined using the Test Statistic value, $TS = -2\ \ln(L_0/L_1)$ which compares the likelihood ratio of models including, e.g., an additional source, with the null-hypothesis of background only [**?**].

[1] See the Fermi Space Science Center (FSSC) website for details of the Science Tools: http://fermi.gsfc.nasa.gov/ssc/data/analysis/

[2] Descriptions of the models are available from the FSSC: http://fermi.gsfc.nasa.gov/ssc

To estimate the systematic errors, which are mainly caused by uncertainties in the effective area and energy response of the LAT as well as background contamination, we use the so-called "bracketing" IRFs. These are IRFs with effective areas that bracket those of our nominal IRF above and below by linearly connecting differences of (10%, 5%, 20%) at log(E/MeV) of (2, 2.75, 4) respectively.

3.2.4 Timing analysis methods

Lightcurves are extracted using aperture photometry, taking an aperture radius of 1° and using the `gtbin` tool. The exposure correction is performed with the tool `gtexposure` assuming the spectral shape of the source to be a power law with an exponential cutoff (see §§ 3.2.5.1, 3.2.6.1). These lightcurves are not background subtracted. The folded lightcurves shown in the subsequent sections are derived by performing `gtlike` fits for each phase bin. Therefore, all of them are effectively background subtracted. We check that both methods for generating lightcurves, aperture photometry and `gtlike` fits, are consistent with each other when the former lightcurves are background-subtracted too.

The primary method of timing analysis employed searches for periodic modulation by calculating the weighted periodogram of the lightcurve [**?** **?** **?**]. The lightcurve is constructed by summing, for each photon, the estimated probability that the photon came from the source of interest. The probability will be both spatially and spectrally dependent. Because this technique allows for the correct weighting of each photon it intrinsically improves the signal-to-noise and allows the use of a larger aperture. This method has successfully been applied to increasing the LAT sensitivity for the detection of pulsars [**?**]. However, in the basic form of this technique, the weight for any particular energy/position is fixed. This means that changes in source brightness will not be reflected in the weights and can result in incorrect probabilities. The calculation of probabilities was performed using the tool `gtsrcprob` and the same source model file derived from the 1FGL catalog and used in the spectral analysis. Since the exposure of the time bins was variable, the contribution of each time bin to the power spectrum was weighted based on its relative exposure. Period errors are calculated using the method of **?**].

3.2.5 LS 5039 Results

LS 5039 is located in a complicated region toward the inner Galaxy with high Galactic diffuse emission and many surrounding γ-ray sources. In particular, the LAT detected a bright (8.7×10^{-7} ph cm^{-2} s^{-1} above 100 MeV) γ-ray pulsar, PSR J1826−1256, $\sim 2°$ away from LS 5039 . Following the analysis performed in the earlier LAT paper [**?**] we discarded events whose arrival times correspond to the peaks of the pulsar cycle of PSR J1826−1256 in order to minimize the contamination from the pulsar. The excluded pulse phase of PSR J1826−1256 is $0.05 < \phi_p < 0.2$ and $0.625 < \phi_p < 0.775$ (see Fig. 37 in **?**]), which results in a loss of 30% exposure on LS 5039. To account for the loss, a scaling factor of 1/0.7 is multiplied to fluxes obtained with maximum likelihood fits.

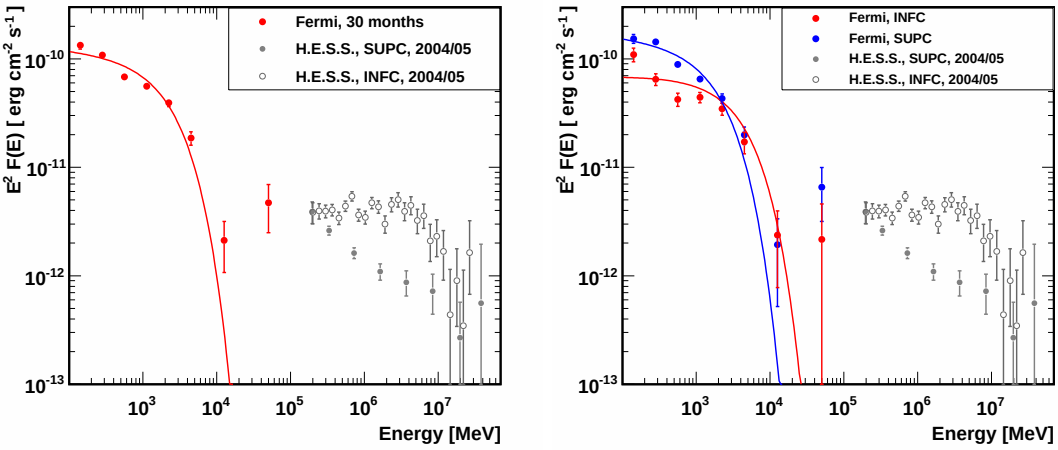

Figure 3.1 *Left:* Spectral energy distribution of LS 5039 as observed by the *Fermi*-LAT (red). The gray open and filled circles are H.E.S.S. spectra in INFC and SUPC, respectively [**?**] and are not simultaneous with the GeV measurements. *Right: Fermi*-LAT and H.E.S.S. spectra of LS 5039 in SUPC (blue) and INFC (red).

3.2.5.1 Orbitally averaged spectral analysis

The orbitally-averaged spectrum of LS 5039 was initially investigated by fitting a power law and a power law with an exponential cutoff to the data. We compare two models utilizing the likelihood ratio test [**?**], i.e. for the ratio $2 \times \Delta log(Likelihood)$ we assume a χ^2-distribution to calculate the probabilities taking into account the corresponding degrees of freedom [**?**]. In this case, the significance of a spectral cutoff was assessed by comparing the likelihood ratio between the power law and cutoff power law cases, which is $-2\ \ln(L_{\rm PL}/L_{\rm cutoff}) = 94.9$, where $L_{\rm PL}$ and $L_{\rm cutoff}$ are the likelihood value obtained for the spectral fits with a power law and a cutoff power law, respectively. This indicates that the simple power law model is rejected at the 9.7σ level in favor of the cutoff power law. The best-fit parameters for the cutoff power law model are $\Gamma = 2.06 \pm 0.06_{\rm stat} \pm 0.11_{\rm syst}$ and $E_{\rm cutoff} = 2.2 \pm 0.3_{\rm stat} \pm 0.5_{\rm syst}$ GeV with a flux of $F_{>100\ \rm MeV} = (6.1 \pm 0.3_{\rm stat} \pm 2.1_{\rm syst}) \times 10^{-7}$ cm^{-2} s^{-1} integrated above 100 MeV. Using a cutoff power-law spectral model, the maximum likelihood fit yields a test statistic of TS = 1623 for the LS 5039 detection; equivalent to $\sim 40\ \sigma$. We also tried a broken power-law spectral model for LS 5039 in addition to an exponentially cutoff power law. We found the broken power law gives lower TS values than the exponentially cutoff power-law case.

Spectral points in each energy band were obtained by dividing the dataset into separate energy bins and performing maximum likelihood fits for each of them. The resulting spectral energy distribution (SED) is plotted in Figure 3.1 together with the best-fit cutoff power law model. Interestingly, the SED shows significantly higher flux (one spectral data point) at $\gtrsim 10$ GeV than the expected flux from the best-fit cutoff power law, possibly suggesting another component at high energies.

One idea explored for these sources (especially, for LS 5039 , see e.g., Torres 2010) is that the γ-ray emission could be understood as having two components: one would be the

magnetospheric GeV emission from a putative pulsar and the other from the inter-wind region or from the pulsar wind zone. The latter would be unpulsed and would vary with the orbital phase, the former would be steady and pulsed. The current data for LS 5039 would indeed allow for this possibility, especially because of the possible high energy component found in the GeV spectrum.

To test the significance of the additional component, we added to the model a power-law source at the location of LS 5039 in addition to the cutoff power law source. Model A is a power law with a cutoff and model B a power law with a cutoff plus an additional power law. Thus, model B has two more free parameters compared to model A. According to the likelihood ratio test, the probability of incorrectly rejecting model A is 6.1×10^{-6} (4.5σ).

The best-fit parameters for the putative additional component are $\Gamma = 1.6 \pm 0.4_{\rm stat} \pm 0.3_{\rm syst}$ and $F_{>10\ \rm GeV} = (1.6 \pm 0.6_{\rm stat} \pm 0.7_{\rm syst}) \times 10^{-10}$ cm^{-2} s^{-1}. The addition of the high-energy component slightly affects the parameters of the cutoff power law. The best-fit parameters for the latter are $\Gamma = 2.02 \pm 0.06_{\rm stat} \pm 0.10_{\rm syst}$ and $E_{\rm cutoff} = 2.0 \pm 0.3_{\rm stat} \pm 0.4_{\rm syst}$ GeV with a flux of $F_{>100\ \rm MeV} = (6.0 \pm 0.3_{\rm stat} \pm 1.9_{\rm syst} \times 10^{-7}$ cm^{-2} s^{-1} integrated above 100 MeV.

3.2.5.2 Phase-resolved analysis

Following the H.E.S.S. analysis by **?**] as well as the previous one, the whole dataset was divided into two orbital intervals: superior conjunction (SUPC; $\phi < 0.45$ and $0.9 < \phi$) and inferior conjunction (INFC; $0.45 < \phi < 0.9$). The SUPC and INFC data were analyzed in the same way as the orbitally averaged data. Being consistent with our previous paper, the power-law assumption for the SUPC spectrum is rejected with $-2\ \ln(L_{\rm PL}/L_{\rm cutoff}) = 81.2$, or at a rejection significance of $\sim 9\sigma$. The best-fit parameters are $\Gamma = 2.07 \pm 0.07_{\rm stat} \pm 0.08_{\rm syst}$, $E_{\rm cutoff} = 1.9 \pm 0.3_{\rm stat} \pm 0.3_{\rm syst}$ GeV, and $F_{>100\ \rm MeV} = (7.8 \pm 0.4_{\rm stat} \pm 1.9_{\rm syst}) \times 10^{-7}$ cm^{-2} s^{-1}.

Although a single power law was not rejected for INFC in our previous analysis using 10 months of data [**?**], a cutoff power law is preferred also for INFC with the present dataset. The likelihood ratio for the INFC data is $-2\ \ln(L_{\rm PL}/L_{\rm cutoff}) = 21.7$, which corresponds to 4.7σ. The parameters for the INFC spectrum are $\Gamma = 1.99 \pm 0.13_{\rm stat} \pm 0.07_{\rm syst}$, $E_{\rm cutoff} = 2.6 \pm 0.7_{\rm stat} \pm 0.9_{\rm syst}$ GeV, and $F_{>100\ \rm MeV} = (3.9 \pm 0.4_{\rm stat} \pm 1.5_{\rm syst}) \times 10^{-7}$ cm^{-2} s^{-1}. Therefore, the SUPC and INFC spectral shapes are completely consistent with one another within the errors. The only difference is the normalization and hence the total flux. On the other hand, the spectrum for INFC (red points in the right panel of Figure 3.1) seems to exhibit additional structure below 1 GeV. The limited statistics and the large contribution of diffuse emission at low energies, however, prevents solid conclusions on whether a more complicated fit (e.g. a double broken power law or a broken power law with a cutoff) would be preferred.

We also searched for emission from the high-energy component in the SUPC and INFC spectra. However, the TS of the additional components compared with a power law with exponential cutoff are only 13.6 and 10.9 for SUPC and INFC, respectively, and do not confirm a second spectral component. The SUPC and INFC SEDs were obtained using the same method as the orbitally averaged spectra and are plotted in the right panel of Figure 3.1.

3.2.5.3 Lightcurve

Figure 3.2 shows the lightcurve for LS 5039 over 30 months derived by performing `gtlike` fits on time bins which contain 6 orbital cycles each. The lightcurve for LS 5039 does not show any significant flux changes. Constructing the periodogram of the weighted photon lightcurve yields a significant detection of a periodicity at 3.90532 ± 0.0008 days. This is consistent with the known orbital period of LS 5039 . The Lomb-Scargle power spectrum of LS 5039 is shown in Figure 3.3. The stability of the orbital modulation was investigated and no significant variation in the modulation fraction as a function of time was found.

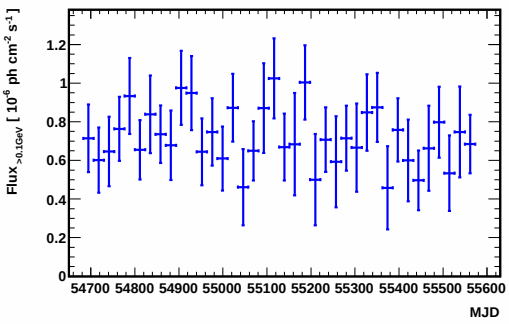

Figure 3.2 Light curve of LS 5039 in time bins of six orbital cycles between 100 MeV-300 GeV. One orbit is 3.90532 days long.

3.2.6 LS I +61°303 Results

3.2.6.1 Orbitally averaged spectral analysis

We have derived the spectrum of orbitally-averaged LAT data, i.e., without any selection criteria (cuts) concerning the orbital phase, for the LS I +61°303 system. The spectral points and corresponding best-fit using the updated dataset described in § **??**

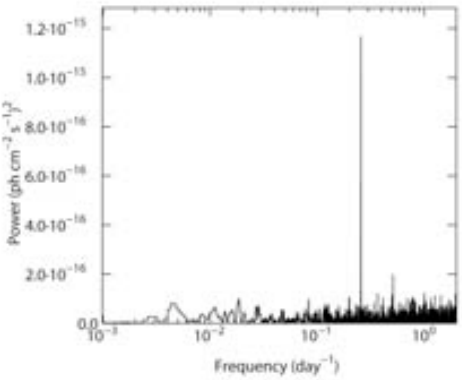

Figure 3.3 Lomb-Scargle power spectrum of the whole GeV data set on LS 5039 .

are shown in Figure 3.4, together with previously derived results from the LAT and TeV observations. Two sets of TeV data are plotted: we show the non-simultaneous data points obtained by the Cherenkov telescope experiments MAGIC and VERITAS. (These data correspond to phases around 0.6–0.7 and represent several orbits observed in the period 2006–2008, before *Fermi* was launched). Additionally, we show the latest measurements performed by VERITAS, which established a 99% C.L. upper limit.[3] The new VERITAS upper limit spans several orbits during which, simultaneously with our LAT data, no detection was achieved. The LAT data along the whole orbit are still best described by a power law with an exponential cutoff. The TS value for a source emitting γ-rays at the position of LS I +61°303 with an SED described by a power law with an exponential cutoff is highly significant. The relative TS value comparing a fit with a power law and a fit with a power law plus an exponential cutoff clearly favors the latter, at the $\sim 20\sigma$ level. The photon index found is $\Gamma = 2.07 \pm 0.02_{\rm stat} \pm 0.09_{\rm syst}$; the flux above 100 MeV is $(0.95 \pm 0.01_{\rm stat} \pm 0.07_{\rm syst}) \times 10^{-6}\,{\rm ph\,cm^{-2}\,s^{-1}}$, and the cutoff energy is $3.9 \pm 0.2_{\rm stat} \pm 0.7_{\rm syst}$ GeV. Results for the obtained TS values for each fit to different datasets are listed in Table 3.2 and all fit parameters obtained for the exponentially cutoff power law models are listed in Table 3.3.

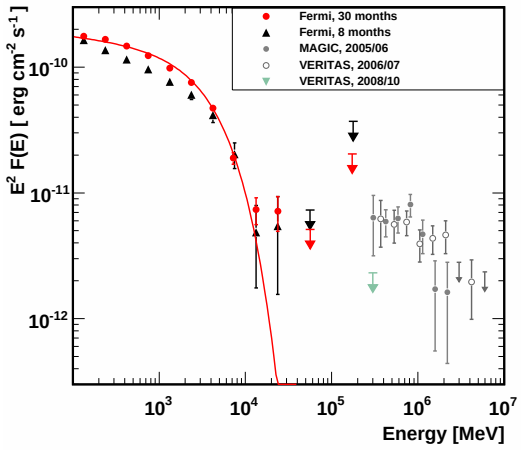

Figure 3.4 The overall 30-months LS I +61°303 spectrum (red) in comparison with the earlier published one (black) over 8 months is shown. TeV data points taken by MAGIC and VERITAS are shown in gray. They are not simultaneously taken with the GeV data. The VERITAS upper limit (in green) is.

Figure 3.4 shows that the data point at 30 GeV deviates from the model by more than 3σ (power law with cutoff, red line). Although in our representation it is only one point, it is in itself significant, with a TS value of 67 corresponding to $\sim 8\sigma$. Therefore, and similarly to the case of LS 5039 , with the caveat of having only one point determined in the SED beyond the results of the fitted spectral model, we investigate the possible presence of a second component at high energies. As in the case for LS 5039 , we use the likelihood ratio test to compare two models: Model A is a power law with a cutoff and model B a power law with a cutoff plus an additional power law. According to this test, the probability of incorrectly rejecting model A is 5.7×10^{-15} (7.8σ). The TS value for this extra power

[3] We derive this differential upper limit by using the VERITAS-reported integral flux upper limit for phases 0.6–0.7 [**?**] assuming a differential spectral slope of 2.6.

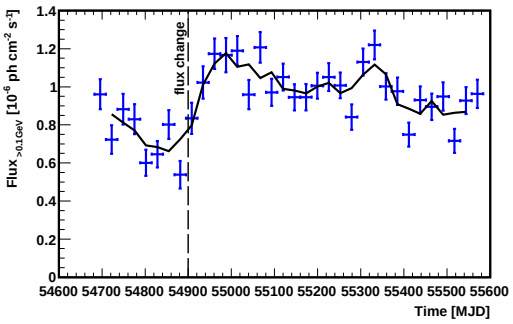

Figure 3.5 Lightcurve of LS I +61°303. Each point represents one orbit of 26.496 days, whereas the black solid line represents the 3-bin smoothed light curve. The black dashed line marks the moment of the flux change in March 2009.

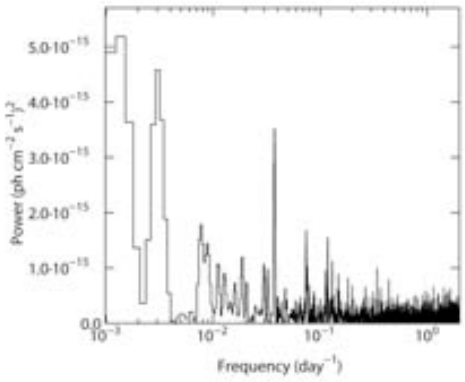

Figure 3.6 The Lomb-Scargle periodogram of the whole LS I +61°303 GeV data set. The orbital period is clearly visible.

law component as a whole is 172, larger than in the case of LS 5039 , and its parameters are $\Gamma = 2.5 \pm 0.3_{\rm stat}$ and $F_{>10\ \rm GeV} = (3.5 \pm 0.6_{\rm stat}) \times 10^{-10}$ cm^{-2} s^{-1}. The addition of the high-energy component affects the parameters of the cutoff power law. The best-fit parameters for the latter, when including the former, are $\Gamma = 2.00 \pm 0.03_{\rm stat}$ and $E_{\rm cutoff} = 2.7 \pm 0.3_{\rm stat}$ GeV with a flux of $F_{>100\ \rm MeV} = (0.88 \pm 0.08_{\rm stat}) \times 10^{-6}$ cm^{-2} s^{-1}. Compared with the cutoff energy of 3.9±0.2 GeV we obtain after fitting only a power law with an exponential cutoff to the data, the cutoff energy decreases when the additional high-energy power-law component is introduced.

An alternative model to accommodate the deviating high-energy point in the spectrum is a fit with a broken power-law. This is further discussed in Section 3.2.6.4.

3.2.6.2 Lightcurve

In Figure 3.5 the lightcurve for LS I +61°303 over 30 months is shown using orbital time bins. The black dashed line represents the point in time when a flux change occurred for LS I +61°303; this ocurred in March 2009. In Figure 3.6 we present the power

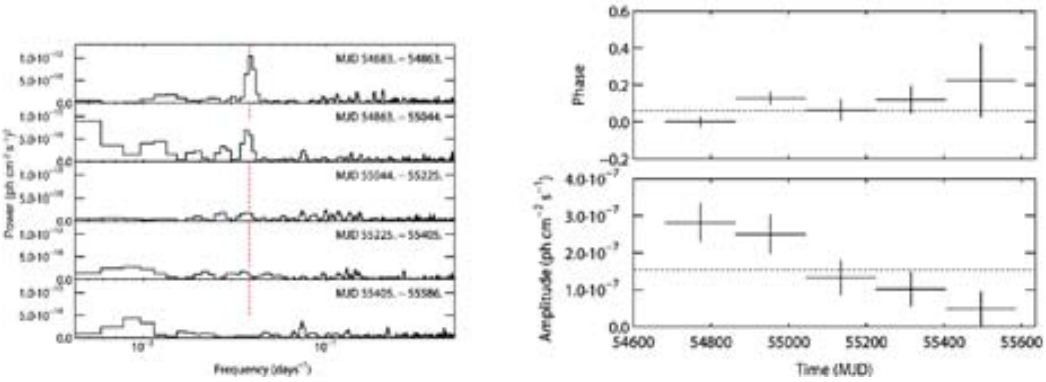

Figure 3.7 *Left:* The Lomb-Scargle periodograms of the LS I +61°303 30 months lightcurve split into five consecutive segments; the earliest is at the top. The red dashed line indicates the known orbital period. *Right:* The change in the amplitude and phase of the orbital flux modulation calculated by fitting a sine wave to each of the lightcurve segments.

Table 3.2 *TS* values for LS I +61°303 for different spectral shapes (see Section 3.2.6.3 for details)

Data set	Power law + exponential cutoff TS	Power law TS	Broken power law TS
30 months of data	23995	23475	23970
Data before March 2009	3404	3314	3415
Data after March 2009	20714	20283	20699
Inferior conjunction (geometrically)	12548	12326	12512
Superior conjunction (geometrically)	11711	11422	11700
Inferior conjunction (angle cut)	6670	6562	6665
Superior conjunction (angle cut)	6083	5986	6063
Periastron	11656	11450	11636
Apastron	12377	12059	12361

Table 3.3 Parameters for LS I +61°303 from spectral fitting with power law with exponential cutoff (see Section 3.2.6.3 for details)

Data set	Photon index Γ	Cutoff energy [GeV]	Flux >100 MeV [$\times 10^{-6}$ ph cm^{-2} s^{-1}]
First 8 months of data	$2.21 \pm 0.04_{(\mathrm{stat}} \pm 0.06_{\mathrm{syst}}$	$6.3 \pm 1.1_{\mathrm{stat}} \pm 0.4_{\mathrm{syst}}$	$0.82 \pm 0.03_{\mathrm{stat}} \pm 0.07_{\mathrm{syst}}$
30 months of data	$2.07 \pm 0.02_{\mathrm{stat}} \pm 0.09_{\mathrm{syst}}$	$3.9 \pm 0.2_{\mathrm{stat}} \pm 0.7_{\mathrm{syst}}$	$0.95 \pm 0.01_{\mathrm{stat}} \pm 0.07_{\mathrm{syst}}$
Data before March 2009	$2.08 \pm 0.04_{\mathrm{stat}} \pm 0.09_{\mathrm{syst}}$	$4.0 \pm 0.6_{\mathrm{stat}} \pm 0.7_{\mathrm{syst}}$	$0.75 \pm 0.03_{\mathrm{stat}} \pm 0.07_{\mathrm{syst}}$
Data after March 2009	$2.07 \pm 0.02_{\mathrm{stat}} \pm 0.09_{\mathrm{syst}}$	$3.9 \pm 0.3_{\mathrm{stat}} \pm 0.7_{\mathrm{syst}}$	$1.00 \pm 0.01_{\mathrm{stat}} \pm 0.07_{\mathrm{syst}}$
Inferior conjunction (geometrically)	$2.14 \pm 0.02_{\mathrm{stat}} \pm 0.09_{\mathrm{syst}}$	$4.0 \pm 0.4_{\mathrm{stat}} \pm 0.7_{\mathrm{syst}}$	$1.07 \pm 0.02_{\mathrm{stat}} \pm 0.07_{\mathrm{syst}}$
Superior conjunction (geometrically)	$2.02 \pm 0.03_{\mathrm{stat}} \pm 0.09_{\mathrm{syst}}$	$3.9 \pm 0.3_{\mathrm{stat}} \pm 0.7_{\mathrm{syst}}$	$0.85 \pm 0.02_{\mathrm{stat}} \pm 0.07_{\mathrm{syst}}$
Inferior conjunction (angle cut)	$2.17 \pm 0.03_{\mathrm{stat}} \pm 0.09_{\mathrm{syst}}$	$4.1 \pm 0.5_{\mathrm{stat}} \pm 0.7_{\mathrm{syst}}$	$1.11 \pm 0.03_{\mathrm{stat}} \pm 0.07_{\mathrm{syst}}$
Superior conjunction (angle cut)	$2.15 \pm 0.03_{\mathrm{stat}} \pm 0.09_{\mathrm{syst}}$	$5.0 \pm 0.7_{\mathrm{stat}} \pm 0.7_{\mathrm{syst}}$	$0.91 \pm 0.02_{\mathrm{stat}} \pm 0.07_{\mathrm{syst}}$
Periastron	$2.14 \pm 0.02_{\mathrm{stat}} \pm 0.09_{\mathrm{syst}}$	$4.1 \pm 0.4_{\mathrm{stat}} \pm 0.7_{\mathrm{syst}}$	$1.01 \pm 0.02_{\mathrm{stat}} \pm 0.07_{\mathrm{syst}}$
Apastron	$2.01 \pm 0.03_{\mathrm{stat}} \pm 0.09_{\mathrm{syst}}$	$3.7 \pm 0.3_{\mathrm{stat}} \pm 0.7_{\mathrm{syst}}$	$0.90 \pm 0.02_{\mathrm{stat}} \pm 0.07_{\mathrm{syst}}$

spectrum of LS I +61°303 derived from the total weighted photon lightcurve. The power spectrum clearly detects the orbital flux modulation with a period of 26.71 ± 0.05 days. This is consistent with the known orbital period of LS I +61°303 [**?**]. The lightcurve clearly shows long-term variability. We searched for changes in the orbital modulation of LS I +61°303 by dividing the aperture photometry lightcurves into 6-month segments and calculating the power spectrum of each segment, as shown in the left panel of Figure 3.7. The amplitude of the orbital modulation is estimated by fitting a sine wave

fixed to the orbital period to each of the lightcurve segments; the results, as seen in the right panel of Figure 3.7, clearly show a decreasing trend in the orbital modulation with time.

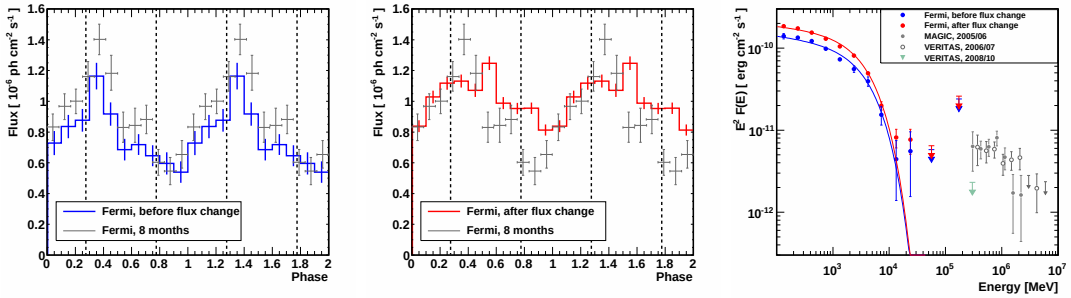

Figure 3.8 *Left:* Folded lightcurve (100 MeV-300 GeV) of LS I +61°303 before the flux change (blue), when the modulation is still clearly visible, compared with the earlier published 8-months dataset shown in gray. *Middle:* Folded lightcurve (100 MeV-300 GeV) after the flux change, in March 2009 (red). The modulation gets fainter. For comparison, the previous published lightcurve is also plotted in gray. *Right:* Comparison of the spectra derived before (blue) and after (red) the flux change in March 2009.

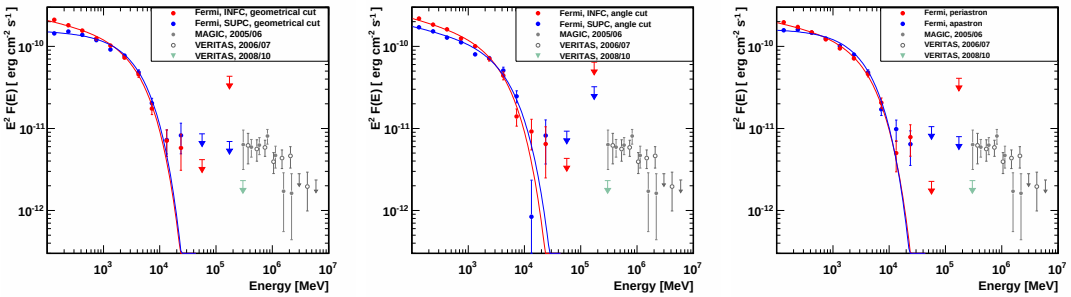

Figure 3.9 Spectra of LS I +61°303 for different phase bins during the orbit are shown. *Left:* Spectra for the geometrical cut of the orbit in superior (blue) and inferior (red) conjunction. *Middle:* Spectra for the angle based cut in superior and inferior conjunction. *Right:* Spectra derived for periastron (red) and apastron (blue).

LS I +61°303 is one of the brightest sources in the γ-ray sky and towers above all other emitters in its neighborhood. This allows us to compute a lightcurve with an orbital binning (26.496 days per bin) which is shown in Figure 3.5. Even by eye it is clear that the source is highly variable on orbital time scales and longer. The longer term trends are evident by looking at a plot of the 3-orbit rolling average (black line in Fig. 3.5). During the first eight orbits the flux decreases by a factor of $\sim$2. Then, in March 2009, the flux appears to increase over the course of several orbits; we take the transition point of this increase to be MJD 54900.

The flux increases significantly by 33$\pm$4%, rising from a baseline of $(0.75 \pm 0.03_{\rm stat} \pm 0.07_{\rm syst}) \times 10^{-6}\,{\rm ph\,cm^{-2}\,s^{-1}}$ obtained from the first 8 months of data to $(1.00 \pm 0.01_{\rm stat} \pm 0.07_{\rm syst}) \times 10^{-6}\,{\rm ph\,cm^{-2}\,s^{-1}}$ which is the average flux of the remaining 1.7 years of the data. Comparing the flux levels averaged over the same time span, 8 months before

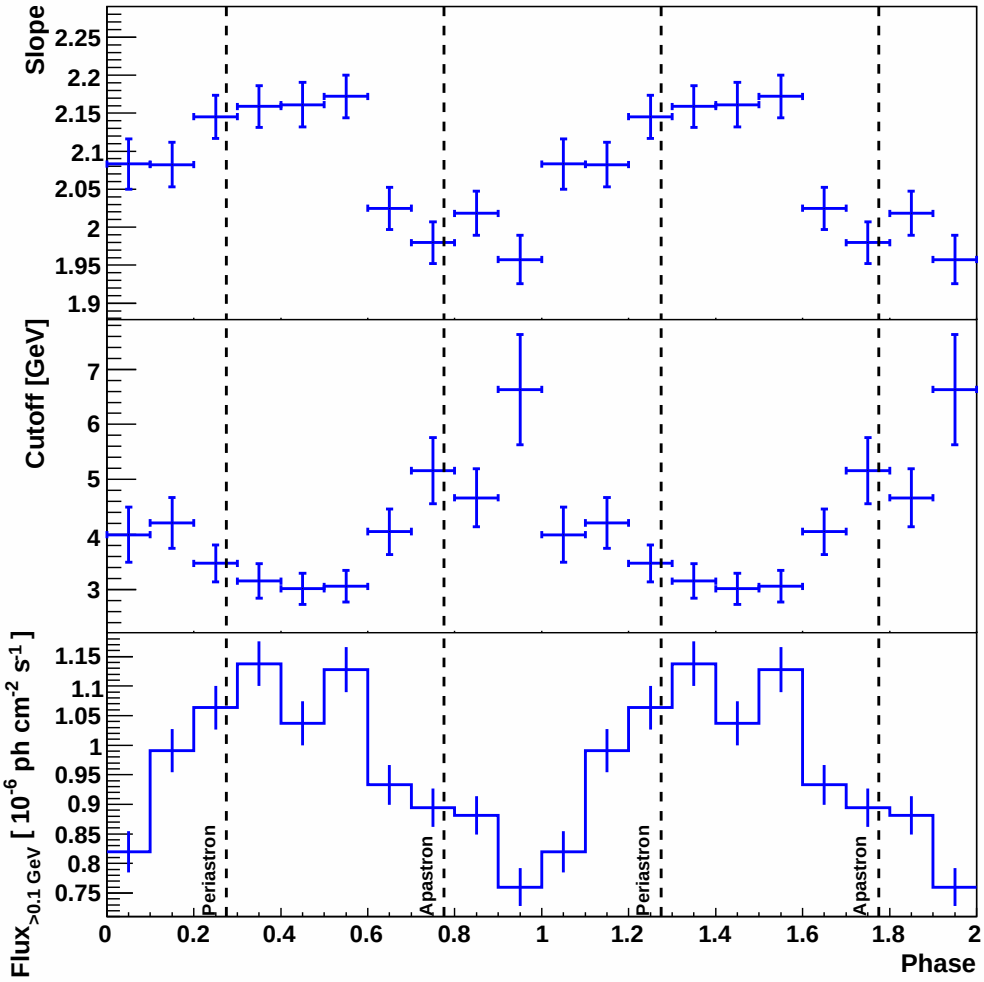

Figure 3.10 The modulation of the spectral parameters of LS I +61°303 on the total 30 months lightcurve. For details see Section 3.2.6.3

and 8 months after the flux change, we obtain a ∼40% increase. After this flux change the flux decreases again slowly over the remaining 1.7 years. The complexities of the short timescale, orbit-to-orbit variability make it impossible to characterise the exact properties of the transition from the 'lower' to 'higher' flux states. The transition likely took place over several orbits, however, for simplicity throughout the remainder of this analysis we use a transition time of MJD 54900.

We graphically show the flux change in Figure 3.8, by plotting the folded lightcurves before and after the transition in March 2009. The data points are folded on the **?**] period, with zero phase at MJD 43,366.275. Before the transition, the modulation was clearly seen and is compatible with the already published phasogram, whereas afterwards, the amplitude of the modulation diminishes. We quantify this behavior by measuring the flux fraction below. Note that the datasets corresponding to the reported results [Abdo 09] and what we here referred to as *before the flux change* span almost exactly the same time range, with the consequence of our current analysis essentially reproducing that previously published. The time span covered by our earlier publication

coincidentally finished just prior to the onset of the flux change. The spectra derived before and after this flux change are shown in Figure 3.8, where the increase in flux is also obviously visible.

3.2.6.3 Phase resolved spectral analysis

The statistics of the current dataset allow us to divide the orbit in different phase ranges and to compute the corresponding spectra for different phase bins. We have divided the orbit into INFC and SUPC phase ranges in two different ways. First, we have split the LS I +61°303 orbit in two halves based on its geometry, as visualized, for instance in Aragona et al. (2009). The SUPC phase range is defined as from phase 0.63 to phase 0.13; INFC is defined correspondingly, as the remaining half. We also adopted another way to separate between INFC and SUPC based on the angle between the compact object, the star, and the observer. Therefore, the orbit is not divided in two halves in this way, but in one piece when the compact object is in front of the star (corresponding to INFC): 0.244 – 0.507; and in another phase range with the same duration, centering at the exact SUPC phase: 0.981 – 0.244. As can be seen in Figure 3.9, the spectra obtained with the different cuts do not differ significantly and all spectral parameters are compatible within their corresponding errors (see Table 3.3). We find that the flux difference between INFC and SUPC is of order of 20%. For these different datasets, representing only portions of the orbit, we modeled the source with a pure power law and with a power law with an exponential cutoff. The ΔTS value comparing both fits for the angular based cut is 108 (INFC), which means that the probability of incorrectly rejecting a power law with respect to an an exponential cutoff is 2.8×10^{-25} (10σ). For SUPC the ΔTS value is 97, which leads to a probability of 6.9×10^{-12} (6.8σ) to wrongly reject the cutoff power law. Hence, the exponential cutoff is preferred over the pure power law also for two parts of the orbit, namely INFC or SUPC.

We have also divided the orbit into phase ranges corresponding to periastron (half of the orbit around phase 0.275) and apastron (the other half, around phase 0.775), based just on the distance between the compact object and the star. In this case, neither a significant difference between the flux values for the two phase bins nor a difference in the spectral shape is visible. These results can also be seen in Figure 3.9. This is probably the result of dividing the orbit into phase ranges which contain both bin phases corresponding to INFC and SUPC.

We also studied the spectral behavior of the source in phase bins of 0.1. For this study we modeled LS I +61°303 with a power law with cutoff for each phase-bin individually. The spectral parameters obtained are shown in Figure 3.10. Note that we fixed in the model the index at 2.07 to study the orbital behavior of the cutoff energy and we fixed the cutoff energy at 3.9 GeV to study the behavior of the index, since both parameters are correlated. These values are, respectively, the results arising from the fit over the whole dataset. A clear orbital modulation of the flux and spectral shape are seen. Through the periastron passage the spectrum gets softer and the flux is maximum, whereas around apastron the spectrum becomes harder and the flux reaches its minimum.

3.2.6.4 Spectral fitting

Both the orbitally-averaged spectrum and the spectra of the several datasets mentioned were also fit with a broken power law, in addition to the pure and exponentially cutoff power law. All the TS values for the different fits are listed in Table 3.2. It is evident that the power law with an exponential cutoff or the broken power law always describe the spectral shape better than a pure power law does. To be precise, when comparing the exponentially cutoff with the pure power law, the ΔTS values span the range from 90 to 520; with the former being always statistically preferred. Fitting a broken power law gives almost the same results. The ΔTS values span the range from 77 to 494 and we find break energies in the range of 0.4 to 1.7 GeV. All of the fits to the various data sets with an exponentially cutoff power law have slightly better TS values with fewer degrees of freedom than a broken power law suggesting that the former model is a better description of the data than the latter one. The exponentially cutoff power law describes nicely the curvature of the spectrum especially at low energies. At higher energies, above the spectral break, the broken power law fits all the spectral points, even the highest one which might be considered possibly part of a second component. Statistically we cannot distinguish which of these two fitting models describes best the data as a whole, but only that both of them are preferred over a pure power law.

3.2.6.5 2.5 years of contemporaneous Radio and GeV data

We have also compared the Fermi data with simultaneous radio data from the Owens Valley Radio Observatory (OVRO) and the Arcminute Microkelvin Imager (AMI) array (Cambridge, UK). Since the launch of Fermi in June 2008, the OVRO 40 m single-dish telescope, that is located in California (USA), has conducted a regular monitoring program of Galactic binaries (e.g. Cyg X−3, **?**]). The OVRO flux densities are measured in a single 3 GHz wide band centered on 15 GHz. A complete description of the OVRO 40 m telescope and calibration strategy can be found in **?**]. Furthermore, we also use complementary observations provided by AMI, consisting of a set of eight 13 m antennas with a maximum baseline of $\sim$ 120 m. AMI observations are conducted with a 6 GHz bandwidth receivers also centered at 15 GHz. See **?**] for more details on the AMI interferometer, that is mostly used for study of the cosmic microwave background. By folding these radio data no super-orbital modulation could be seen, which could be due to the poor coverage of a whole super-orbit. A direct comparison of the GeV and the radio data is shown in Figure 3.11 where the flux over time is plotted. No correlation of the data points can be seen either. In summary, we did not find any correlation between the GeV and the radio band, either in archived nor in simultaneous data.

3.2.6.6 Summary

After analyzing a dataset comprising 2.5-years of *Fermi*-LAT observations of the two binaries LS 5039 and LS I +61°303, we note several changes with respect to the initial reports of **(author?)** [Abdo 09**?**]. These were produced either because the accumulation of a longer observation time allowed us to make distinctions that were earlier impossible (valid for both sources), or because the behavior of the source changed (valid for LS I +61°303). On one hand, the statistics are now sufficient to divide the dataset of both sources in INFC and SUPC and to show that a power law with a cutoff describes

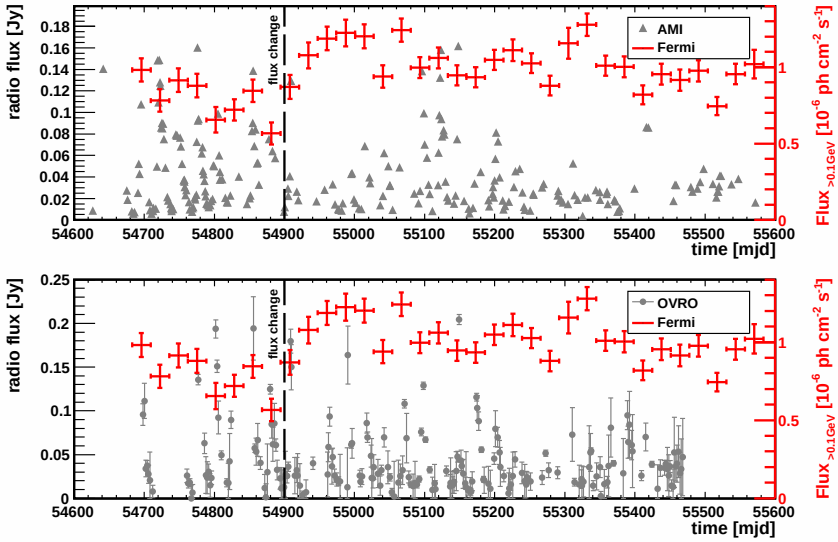

Figure 3.11 Lightcurve of LS I +61°303. Each point represent one orbit of 26.496 days. The black dashed line marks the moment of the flux change in March 2009, together with the simultaneously taken radio data by the AMI and OVRO instruments (both operating at 15 GHz) are shown in gray.

the spectra obtained in both conjunctions better than a pure power law. The cutoff is similar to that found in the many other GeV pulsars discovered by *Fermi*-LAT. However, we have found that both LS 5039 and LS I +61°303 show an excess of the high energy GeV emission beyond what is expected from an exponentially cutoff power law. While the high energy data are significantly in excess of the exponentially cutoff power law there are insufficient statistics at these high energies to model the excess with an additional spectral component.

The process(es) generating such a component in the case of LS 5039 and LS I +61°303 is unclear and may even be different in the two sources. However, such a second component would present a possible connection between the GeV and TeV spectra in both sources. Collecting more data and therefore more statistics will allow to prove or discard it in the future. The lack of datapoints at high energies, also affects, particularly in the case of LS I +61°303, the distinction between an exponentially cut and a broken power law. Currently, both are certainly preferred over a pure power law, but differences in the significances provided between the former are minor.

We have noted that whereas LS 5039 shows stable emission over time and also a stable orbital modulation, LS I +61°303 shows a change in flux in March 2009. Afterwards the orbital modulation decreases and the orbital period could not be detected in the GeV data. A more detailed study on this behavior can be found in Section 3.3.

3.3 LS I +61°303 Longterm Gamma-Ray Variability

As mentioned in the previous chapters, the gamma-ray binary LS I +61°303 is highly variable across all frequencies, detected from radio to TeV gamma rays. Besides the

orbital modulation of $\sim$ 26.4960-days, which was already found at high and very high energies, in the following chapter we present the first discovery of superorbital variability at high energies. This sinusoidal variability is present at the known superorbital period of 1667 days. It is more prominently seen at orbital phases around apastron, whereas it does not introduce a visible change close to periastron. It is also found in the appearance and disappearance of variability at the orbital period in the power spectrum of the data. This behavior could be explained by a quasi-cyclical evolution of the equatorial outflow of the Be companion star, whose features influence the conditions for generating gamma rays. These findings open the possibility to use gamma-ray observations to study the outflows of massive stars in eccentric binary systems. This chapter is based on the publications [Li 11, Li 12] and the work in preparation [Hadasch 13].

3.3.1 Data and Analysis settings

The analysis presented here makes use of all data taken from the beginning of scientific operation of *Fermi*-LAT on 2008 August 4 until 2013 March 24 The data were analyzed using the LAT *Science Tools* package (v9r30), which is available from the *Fermi* Science Support Center. The analysis used the *P7v6* version of the instrument response functions. Only events passing the "Source" class cuts are used in the analysis. All gamma rays with energies > 100 MeV within a circular region of interest (ROI) of 10° radius centered on LS I $+61^\circ$303 were extracted. Furthermore, to reduce the contamination from the Earth's upper atmosphere time intervals when the Earth was in the field of view were excluded, specifically when the rocking angle of the LAT was greater than 52° or when parts of the ROI were observed at zenith angles $> 100^\circ$. The gamma-ray flux of LS I $+61^\circ$303 plotted in the lightcurves of this work are calculated performing the binned or the unbinned maximum likelihood method, depending on the statistics, by means of the Science Tool `gtlike`. The spectral-spatial model constructed to perform the likelihood analysis includes all the sources of the second catalog of *Fermi*-LAT [**?**] (hereafter 2FGL) within 15° of LS I $+61^\circ$303. The spectral parameters were fixed to the catalog values, except for the sources within 3° of LS I $+61^\circ$303. For these latter sources, the flux normalization was left free. LS I $+61^\circ$303 was modeled with a power-law with exponential cut-off spectral shape. All its spectral parameters were allowed to vary (see [**?**] for further details). The models adopted for the Galactic diffuse emission (gal_2yearp7v6_v0.fits) and isotropic backgrounds (iso_p7v6source.txt) were those currently recommended by the LAT team.[4]

Systematic errors mainly originate in the uncertainties in the effective area of the LAT, as well as in the Galactic diffuse emission model. The current estimate of the uncertainties of the effective area is 10% at 100 MeV, decreasing to 5% at 560 MeV and increasing to 10% at 10 GeV and above. We assume linear extrapolations, in log space, between the quoted energies. The systematic effect is estimated by repeating the likelihood analysis using modified instrument response functions that bracket the "`P7SOURCE_V6`" effective areas. Specifically, they are a set of IRFs in which the effective area has been modified considering its uncertainty as a function of energy in order to maximally affect a specific spectral parameter. In order to conservatively take into account the effect due to the uncertainties of the Galactic diffuse emission model, the likelihood fits are repeated changing the normalization of the Galactic diffuse model artificially by $\pm 6\%$. We have

[4] Descriptions of the models are available from the FSSC: http://fermi.gsfc.nasa.gov/

found flux systematic errors (for energies above 100 MeV) on the order of 9%, similar to the ones reported in [**?**].

3.3.2 Results

Orbital modulation of the GeV flux can be understood as a consequence of changing conditions for generation and absorption of gamma rays, which are mostly determined by the orbital geometry; e.g., the viewing angle to the observer and the position of the compact object with respect to the stellar companion. Unless other physical conditions change, we do not expect long-term variability of the emission level at a fixed orbital configuration.

Figure 3.12 shows the orbitally-folded lightcurve of LS I +61°303 from 2008 August 4 to 2013 March 24. In this Figure, the total observation time is divided in intervals of the same duration; each panel represents an equal time period of 169.2 days (or roughly 6.4 orbits of the system).

It shows a trend for the maximum of the gamma-ray emission in each orbit to appear at orbital phases near periastron (phases around 0.3). The minimum of the gamma-ray emission, instead, seems to be consistently located at orbital phases near the apastron (phases around 0.8), as in [**?**]. Despite these trends, Figure 3.12 also shows that LS I +61°303 presents significant variability at fixed orbital positions.

Here, we want to explore the possibility that the observed long term gamma-ray variability could be related to the superorbital period of 1667±8 days as reported in radio [**?**]. This same period was also found in optical [**?** **?**], and X-ray [**?** **?**] emission.

The period of the superorbital variability of LS I +61°303 has been best determined (with the longest coverage in time) in a radio campaign lasting 23 years (1977-2000), and was found to be 1667±8 days [**?**], a value found at other frequencies.

Figure 3.13 shows the long-term evolution of the average gamma-ray flux; we use the superorbital period of [**?**] to translate time to superorbital phase. The probability that this evolution is a random result out of a uniform distribution is $< 1.1 \times 10^{-12}$ (χ^2, *ndf* = 75.8, 9).

To check for a possible long-term modulation of the gamma-ray flux at fixed orbital positions, we have separated the data in orbital bins, and plotted the fluxes against the superorbital phase, as shown in Figure 3.14. From orbital phase 0.1 to 0.5, including the periastron region of LS I +61°303, there is no significant variation along the superorbital phase. When LS I +61°303 departs from periastron (see the panels for the orbital phase 0.5 and onwards), a sinusoidal variability along the superorbital phase appears. The amplitude of the variation is maximal before and after apastron.

The black line in each of the panels of Figure 3.14 represents a sinusoidal function fit to the data points. The period of this function has been kept (in all panels) at the value of the superorbital period found in radio (1667 days). Thus, the function we use to fit the data has three parameters: average flux level, amplitude, and phase. We have also fitted a constant line for comparison.

Table 3.4 shows the quality of the fitting results corresponding to Figure 3.14. It has the following columns: the system's orbital phase, the corresponding χ^2 and numbers

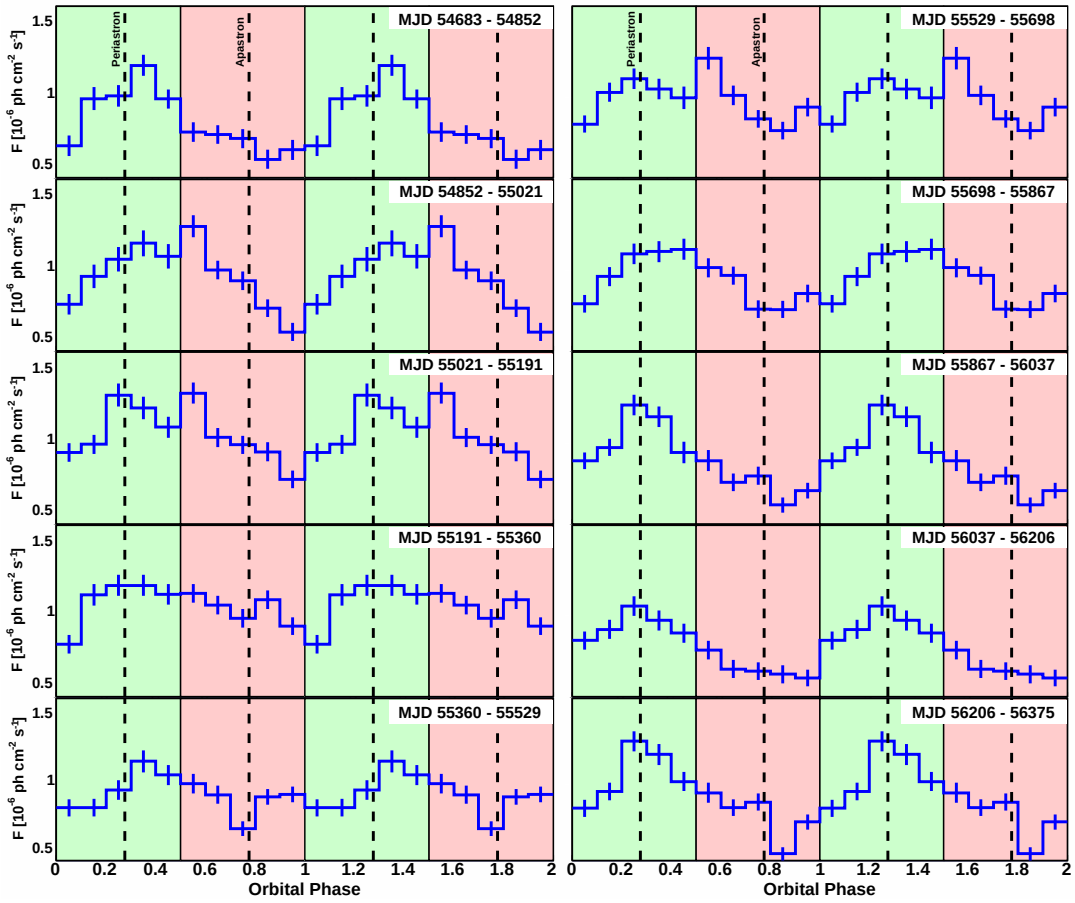

Figure 3.12 Gamma-ray flux from LS I +61°303 folded on the orbital period. The data are repeated over two cycles for clarity. Photons with energies above 100 MeV, as measured by *Fermi*-LAT are considered. The measurements covers the period from 2008 August 4 to 2013 March 24, from the top left panel to the bottom right. Each panel spans 169.2 days. The position of periastron and apastron are marked with dashed vertical lines (the ephemeris of Ref. [**?**] is used). The two background colors correspond to the periastron (orbital phases 0.0–0.5) and apastron (orbital phases 0.5-1.0) regions of the orbit.

of degrees of freedom as well as the probability that the data are described by either a constant or a sinusoidally varying flux, and finally the probability that the improvement found when fitting a sinusoid instead of a constant is produced by chance. To obtain the latter we consider the likelihood ratio test [**?**]. The test is performed by computing the ratio $2 \times \Delta log(Likelihood)$ for the two hypotheses (constant and sinusoidal) and assuming that for a chance coincidence the ratios are χ^2-distributed according to the corresponding degrees of freedom between the two hypotheses [**?**]. Thus, if the hypothesis of a constant is true, the likelihood ratio $R = -2\ln(L(constant)/L(sine))$ is approximately χ^2-distributed with N degrees of freedom, where N is the difference between the number of the free parameters of two hypotheses. The probability that one hypothesis is preferred over the other is defined as $P = \int_0^{R_{meas}} p(\chi^2)d\chi^2$ where $p(\chi^2)$ is the χ^2 probability density function and R_{meas} the measured value of R. The constant hypothesis will be rejected (and the sinusoidal will be accepted) if P is greater than the confidence level, which is set to 95%. In Table 3.4, the last column states the probability that the fit improvement (of a sine over a constant) is happening by chance (thus, $1-P$).

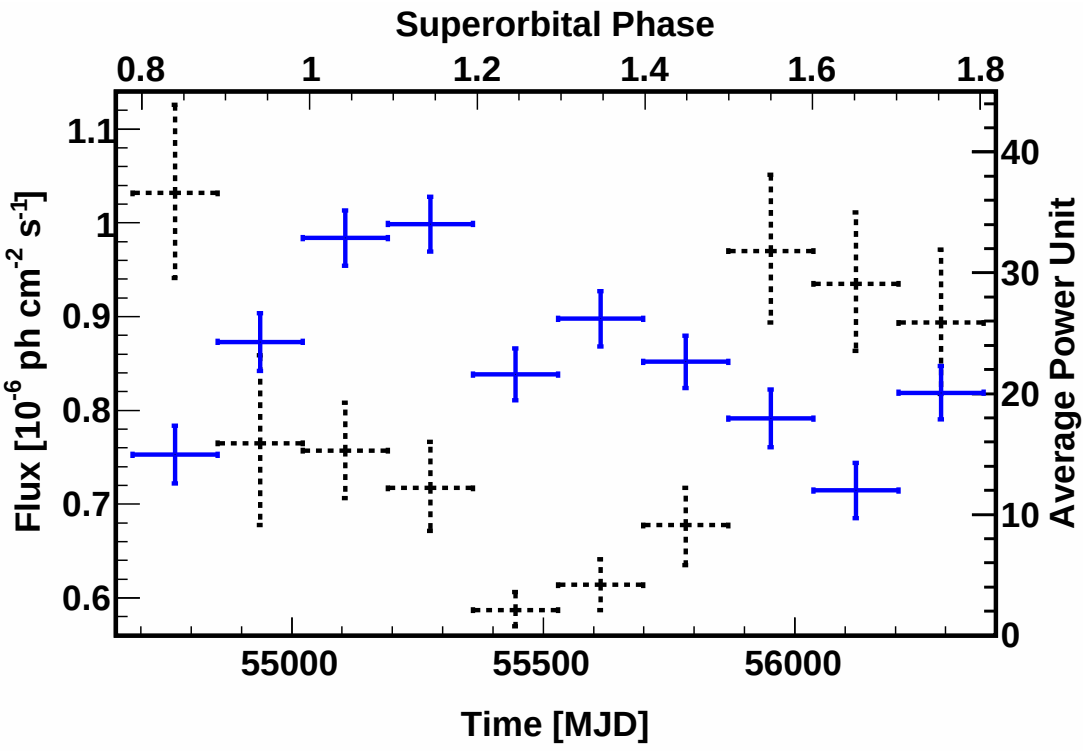

Figure 3.13 Long-term evolution of the average gamma-ray flux (above 100 MeV) from LS I +61°303 (blue points, left y-axis scale). The superorbital phase is shown in the top axis. The right y-axis scale and the black dashed points show the long-term evolution of the power at the orbital period found in the Lomb-Scargle periodogram. A significance of 3σ (5σ) corresponds to about 6 (15) Average Power Units.

These results confirm what has been gathered by eye-inspection above: No strong variability is found at orbital phases 0.0–0.5, while it is clearly present in the range 0.5–1.0. Concurrently, data at the orbital phases 0.0 to 0.5 are not significantly better-represented by a sine than by a constant. However, this is not the case for the data at the orbital phases 0.5 to 1.0. The probability that the sinusoidal fit improvement occurs by chance is less than 1.0×10^{-7} at orbital phases 0.5–0.6, 0.6–0.7, 0.8–0.9, and 0.9–1.0; and 1.4×10^{-5} at orbital phases 0.7-0.8. Whereas the sinusoidal variation is always a better fit in this part of the orbit, the amplitude of the fit is maximal in orbital phases before and after the apastron.

Table 3.5 shows the sinusoidal fit parameters corresponding to the right-hand panels of Fig. 3.14. The functional form of the fit is $F_0 + A \times \sin((t - T_0)/T - \phi) \times 2\pi)$. Here, T_0 and T are the zero time (T_0 = MJD 43366.275) and the period (always kept fixed at 1667 days in all panels) of the superorbit, respectively (both as in [**?**]), t is the time, F_0 is the average flux level, A is the amplitude, and ϕ represents the phase shift in the superorbit. The choice of a sinusoidal function for fitting the data is not based on any *a priori* physical expectation; the superorbital variability could be periodic but have a different shape. However, any periodic function could be described by a series of sines. Thus, fitting with just one sinusoidal function as done above is motivated by the relatively low number of data points.

We have also searched for the orbital periodicity in gamma-rays in the power spectrum of our data. Our previous analysis of 2.5 years [**?**] has shown that the power spectrum

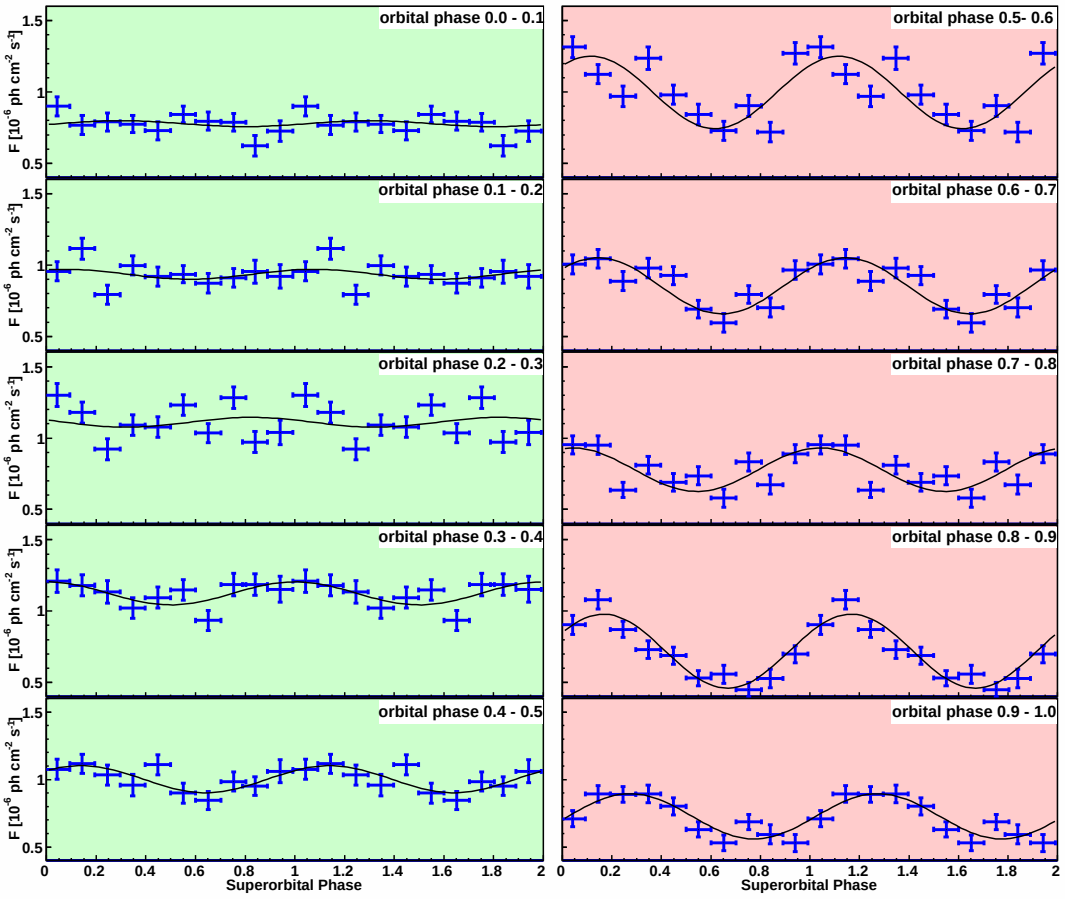

Figure 3.14 The evolution of the gamma-ray flux (above 100 MeV) from LS I +61°303 at fixed orbital phases as a function of the superorbital phase. The data points are repeated over two superorbital periods for the sake of clarity. The left panels represent the region of the orbit near periastron (located at phase ~ 0.3, see Figure 3.12) where the data are compatible with no superorbital variability beyond 3σ. The right panels, instead, are regions close to apastron. The black line in each of the panels is a sinusoidal function fit to the data points, with a fixed period of 1667 days.

peak at the orbital signal disappeared as time advanced. We have now found that along the time covered by our observations, the power spectrum peak is significant only at superorbital phases $\sim 0.5 - 1.0$. At other superorbital phases, the peak is absent or has a significance less than 3σ. These results are shown in Figure 3.13.

In order to test for the appearance/disappearance of the orbital signature in gamma-rays, we subdivided the data into the same time intervals as considered before for Figure **??** (intervals of 169.2 days each), and applied the periodogram technique [**?** **?**] to each of them. To calculate the power spectrum the event selection was restricted to a ROI of 3° centred on LS I +61°303, and the good time intervals were recalculated. The selected events were used to create a lightcurve of weighted counts over exposure with equally spaced time bins of 2.4 hours width. The weight associated to each event corresponds to the probability that the gamma-ray was emitted by LS I +61°303, rather than by nearby sources or has a diffuse origin. The weights are calculated using the *Science Tools*'s `gtsrcprob`, adopting the best spectral-spatial models obtained by the binned

Table 3.4 Quality of the fitting results corresponding to Figure 3.14. For details on the columns shown, see text.

Orbital Phase	χ^2, ndf (constant)	Constant Fit Probability	χ^2, ndf (sine)	Sine Fit Probability	Prob. improvement by chance
0.0–0.1	10, 9	3.2×10^{-1}	10, 7	1.9×10^{-1}	1.0
0.1–0.2	13, 9	1.8×10^{-1}	12, 7	1.1×10^{-1}	1.0
0.2–0.3	27, 9	1.4×10^{-3}	26, 7	5.0×10^{-4}	0.7
0.3–0.4	13, 9	1.6×10^{-1}	8, 7	3.6×10^{-1}	7.0×10^{-2}
0.4–0.5	15, 9	9.9×10^{-2}	6, 7	5.4×10^{-1}	1.2×10^{-2}
0.5–0.6	84, 9	2.8×10^{-14}	23, 7	2.0×10^{-3}	$< 1.0 \times 10^{-7}$
0.6–0.7	50, 9	8.1×10^{-8}	10, 7	2.2×10^{-1}	$< 1.0 \times 10^{-7}$
0.7–0.8	41, 9	6.1×10^{-6}	18, 7	1.0×10^{-2}	1.4×10^{-5}
0.8–0.9	100, 9	2.4×10^{-17}	8, 7	3.0×10^{-1}	$< 1.0 \times 10^{-7}$
0.9–1.0	50, 9	9.1×10^{-8}	10, 7	2.2×10^{-1}	$< 1.0 \times 10^{-7}$

Table 3.5 Sinusoidal fitting parameters for the apastron region panels of Figure 3.14.

Orbital Phase	F_0 [10^{-6} ph cm^{-2} s^{-1}]	A [10^{-6} ph cm^{-2} s^{-1}]	ϕ
0.5–0.6	1.00±0.03	0.25±0.03	0.87±0.03
0.6–0.7	0.85±0.02	0.20±0.03	0.90±0.02
0.7–0.8	0.78±0.02	0.15±0.03	0.79±0.03
0.8–0.9	0.72±0.03	0.26±0.03	0.92±0.03
0.9–1.0	0.73±0.02	0.17±0.03	0.02±0.04

likelihood fits described in the previous section. Before calculating the power spectrum, we also applied to the lightcurve the exposure weighting described in [**?**].

Figure 3.15 shows the power spectra calculated in each of the time intervals. The vertical line marks the orbital period (as in [**?**]). The y-axis in the periodograms is given in average power units, which converts the original spectrum in units of (ph cm^{-2} s^{-1})^2 by normalizing it with the average of the power over all the frequencies $< P >$. In this way, the units are directly linked to the significance of the peak, which for a peak of power $\bar{P}$ is computed as $\mathrm{Prob}(P > \bar{P}) = \exp(-\bar{P}/ < P >)$ [**?**]. These average power values are plotted in Fig. 3.13. A significant peak is detected at the orbital period, but not in all time intervals. Note that in some of the panels of Figure 3.15 there appears to be a shift of the 26.5-day peak, even though it is within the fundamental frequency ($1/T_{obs}$) of the orbital period. A claim that the period shift of these peaks is significant would then imply a severe oversampling of the Fourier resolution, which for the duration of this dataset is 3.84 days. The shifted peaks are not significant either in the single-trial (looking for an specific frequency) or in the all-trials probability analysis of these power spectra.

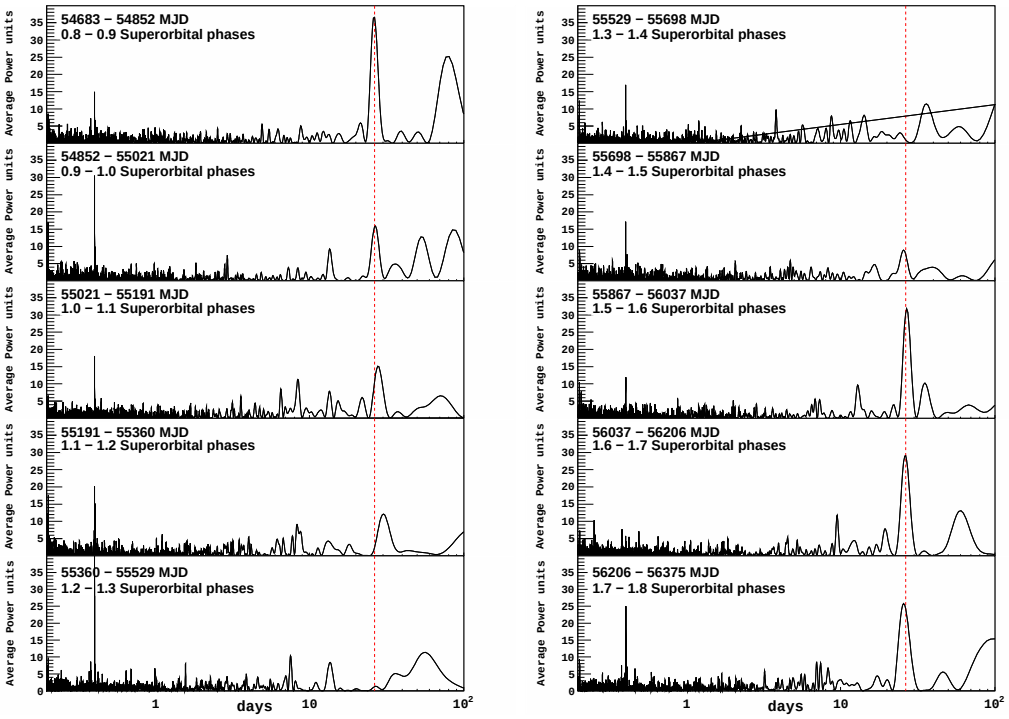

Figure 3.15 Periodogram of the gamma-ray data for different time intervals. The dashed line marks the orbital period of LS I +61°303.

3.3.3 Interpretation

In order to connect the discovered gamma-ray observational pattern to conditions that vary over the superorbit, a quasi-cyclical expansion and shrinking of the circumstellar disc of a Be star may offer an alternative (e.g., [**?**]). The sizes of the stellar discs of Be stars are hypothesized to correlate with the equivalent width (EW) of the Hα emission line (e.g., [**?**]). In eccentric binary systems, though, the disc size must be rather understood as a radius of influence, for the neutron star con expel part of the matter in the disc, effectively truncating it and producing a spiral shape for the matter outflow [**?**].

In the longest-running campaign observing LS I +61°303 the maximum of the Hα EW has been found in a broad region around superorbital phase 0.2 (see [**?**], also [**?** **?**] and references therein). Thus, the X-ray [**?**] as well as the gamma-ray emission are enhanced at superorbital phases where maximal values of the Hα EW have been measured.Concurrently, the power spectrum peak at the orbital period is less significant. This suggests that the disc may play a role in modulating both the gamma and the X-ray signals. One possibility could be that an increase in the mass loss rate, size, and density of the Be disc leads to an increase of the mass accretion onto the compact object, modifying the conditions by which GeV and X-ray emission are produced.

From the results in Figure 3.14, one may conclude that in the periastron region, when the emission from the system is subject to essentially no superorbital variability, the conditions for the generation of gamma rays in the GeV range must not significantly change. We can thus assume that the compact object could be inside or severely affected by the Be disc matter when it is closer to the companion star (i.e., at orbital phases 0.0 to 0.5), for all superorbital phases. If this is the case, even when the EW of the Hα

line (and thus the radius within which the disc influences) changes by a factor of a few along the superorbital period[5], this does not necessarily imply a significant change in the gamma-ray modulation above the sensitivity of *Fermi*-LAT when the compact object is near periastron. However, in a two-component model typically assumed for Be stellar winds (an equatorial wind generating the disc, and a polar outflow) the conditions in the apastron region (e.g., the pressure exerted by the wind, or the mass gravitationally captured by the compact object) could change by more than 3 orders of magnitude if one or the other component dominates (see, e.g., [**?**] and references therein). In such a case, it is reasonable to suppose that the GeV emission would be affected at an observable level.

We notice from Figure 3.14 that between the orbital phase ranges 0.9–1.0 and 0.0–0.1 there is a significant change of the long-term behavior of the gamma-ray emission. Closer to periastron the flux evolution flattens. We can then estimate the radius at which the matter in the disc of the Be star produces a stable influence with time by computing the system separation at orbital phase ~ 0.1. Using the ephemeris given by [**?**], we obtain a separation of $\sim 9R_s$, where R_s is the stellar radius of the Be star. On the other hand, from the fact that the maximal amplitude of the superorbital variability is before and after the apastron of the system, the system separation at orbital phases 0.7 and 0.9 ($\sim 13R_s$) could also have a physical meaning. It is a qualitative upper limit to the influence of the matter in the equatorial outflow when maximally enhanced by the long-term change of the stellar mass-loss rate.

The ratio between what appears to be the maximal and the stable radii of influence of the disc matter is consistent with a possible increase of the EW of the Hα line. Outer radii of discs in binaries are expected to be truncated by the gravitational influence of their compact companions; at the periastron distances in systems of high eccentricity, and by resonances between the orbital period and the disc gas rotational periods in the low-eccentricity systems [**?**]. LS I +61°303 is a system between these two cases. The effects of the Be star's rotation, which have only recently started to be taken into account, may modify this conclusion, predicting disc sizes in excess of 10 R_s [**?**]. Assuming the relation between disc size and the EW of the Hα by [**?**], and not taking into account rotation effects, typical values of the EW of LS I +61°303 would lead to an estimation of the disc radius of the order of the periastron distance [**?**]. Simulations indicate that tidal pulls at periastron can lead to the development of large spiral waves in the disk that can extend far beyond the truncation radius and out to the vicinity of the companion (see e.g., [**?** **?**]), promoting accretion [**?**]. The gamma-ray data apparently provide a window to measure the extent of these waves, at different phases of the superorbit. LS I +61°303 is also particular in that, contrary to other binaries, it shows persistent Hα line emission along decades, which may imply an accumulation of matter in the orbital plane.

Depending on the period and dipolar magnetic field, a highly-magnetized neutron star can transition between states along the orbital evolution of LS I +61°303, changing its behavior from propeller (near periastron) to ejector (near apastron) along each orbit [**?** **?** **?**]. These changes of state can be affected by the superorbital variability, since for a larger disc-influence radius, the system will remain in the same environment for a longer time [**?**]. The orbital variability is consequently reduced, leading to the disappearance

[5] The mass-loss rate variations from the Be star in LS I +61°303 were estimated as the ratio between maximal and minimal values of its radio emission (a factor of ∼5 was determined by [**?** **?**]) or its Hα measurements, which span factors of ∼1.5 to 5 [**?** **?** **?** **?**].

Table 3.6 Reduced χ^2 for fitting different models to the modulation fraction and the peak flux in X-rays.

	Constant	Linear	Radio	Shifted
Modulation Fraction	88.2 / 7	38.0 / 6	42.1 / 6	1.1 / 5
Peak Flux	212.8 / 7	114.8 / 6	91.8 / 6	4.9 / 5

of the orbital peak in the power spectrum [**?**]. The data presented in this report will put the details of this model to the test while opening the gamma-ray window for studying the discs of Be binaries.

3.3.4 Multi-wavelength context

3.3.4.1 X-rays

Table 3.7 Quality of the fitting results corresponding to Figure **??**. For details on the columns shown, see text.

Data Set	Constant Fit Probability	χ^2, ndf (constant)	Sinus Fit Probability	χ^2, ndf (sine)	Prob. improv. by chance
average γ-ray flux	1.1×10^{-12}	75.9, 9	0.63×10^{-1}	13.4, 7	8.7×10^{-12}
peak γ-ray flux	1.6×10^{-1}	13.1, 9	2.3×10^{-1}	9.3, 7	1.5×10^{-1}
mod. flux fraction	1.4×10^{-3}	27.0, 9	4.3×10^{-1}	6.9, 7	4.5×10^{-5}

LS I +61°303 has also been monitored with the *R*XTE–Proportional Counter Array (PCA) and as mentioned before, also in this energy range the superorbital modulation was unveiled. The analysis of PCA data was performed using HEASoft 6.9 and the data were filtered following the standard *R*XTE-PCA criteria. The flux and count rate values are given for an energy range of 3–30 keV. The on-source time amounts to 684.3 ks, and it is uniformly distributed in the system's orbital (between 60 and 80 ks per each 0.1 of orbital phase bin) as well as in the system's super-orbital phase (around 60 ks per each 0.1 of super-orbital phase bin, except at super-orbital phase 0.8, where an intensive campaign increased the exposure to 120 ks) as defined by the radio observations (Gregory 2002, PUT REF CORRECTLY!). The superorbital modulation is visible binning the X-ray data in six-month time bins (or approximately 6.8 orbits of the system). We take the average and the peak X-ray flux in that period and compute the modulated flux fraction. The latter is defined as $(c_{max} - c_{min})/(c_{max} + c_{min})$, where c_{max} and c_{min} are the maximum and minimum count rates in the 3–30 keV orbital profile of that period, after background subtraction. Results are shown as the red points in Figure **??**. Table 3.6 presents the values of the reduced χ^2 for fitting different models to the modulation fraction and the peak flux in X-rays. It compares the results of fitting a horizontal line, a linear fit, and two sinusoidal functions. One of the latter has the same period and phase of the radio modulation (from Gregory 2002, labelled as 'Radio' in Table 3.6, dotted line in Figure **??**). The other sine function has the same period as in radio but allowing for a phase shift from it (a solid red line in Figure **??**, labelled as

'Shifted' in Table 3.6). It is clear that there is variability in the data (and thus that a constant fit is unacceptable), as well as that the sinusoidal description with a phase-shift is better than the linear one, which is obvious by visual inspection of Figure **??**. The phase shift derived by fitting the modulated fraction is 281.8 ± 44.6 days, corresponding in phase to ∼ 0.2 of the 1667±8 days super-orbital period. The phase shift derived by fitting instead the maximum flux is 300.1 ± 39.1 days, and results compatible with the former.

A similar analysis we did with the γ-ray data set as described in Chapter XXX. We plot the peak flux, the average flux and the modulated flux fraction (blue points in Figure **??**) into the same plot together with the corresponding X-ray data. To the γ-ray data we fitted two different models: a constant and a sinusoidal function. The fit results are summarized in Table 3.7. From there it can clearly be seen that for the average flux and the modulated flux fraction a fit with a sinusoidal is preferred over a fit with a constant. In the case of the peak flux both, a constant or a sine, describe the data well. Furthermore, in both cases the peak of the sine occurs earlier in the superorbit than the sine of the X-ray data. Anyway, comparing these three parameters in the high energy and the X-ray band has to be made with care since they can be driven by totally different effects.

We studied if there is anything special concerning the half year time binning chosen to present the former results. It is interesting to note that the smaller the time bin the larger it is the scattering around the sinusoidal fit, which can be understood as an effect of the increasing similarity between the time bin itself and the orbital period of the system (of 26.4960±0.0028, Gregory 2002). Indeed, orbit-to-orbit variability is known to exist in our data, and can be similar or larger than the super-orbital induced variability at times (e.g., see the variations found for the same phase-bin in contiguous orbits in Figure 4 of Torres et al. 2010 in the case of X-rays and Figure xxx in the case of γ-ray). Thus, the shorter the time bin, the less likely it is that the super-orbital induced variation could be detected, which may be sub-dominant to the local-in-time changes. On the contrary, as soon as the integrated time bin is large enough in comparison with the orbital period of LS I +61°303, the super-orbital variability is consistently observable. This is the case for X-rays as well as for γ-rays.

We notice that the X-ray long-term monitoring (2007–2011) on LS I +61°303 started about 7 years later from the end of the campaign used to determine the super-orbital period in radio (1977–2000, see Gregory 2002). We will assume then that the radio-determined super-orbital modulation of the source is, although possibly variable, active today with similar features as the ones claimed a decade earlier. This appears possible given that recent reports of variation in the orbital radio maxima are of only ∼0.1 in phase (see Trushkin & Nizhelskij 2010). Under such assumptions, we showed that there is a phase shift between the radio and the X-ray super orbital modulation.

Interestingly, this shift is the same as the one hinted at between the radio and the Hα line (Zamanov et al. 1999, Zamanov & Martí 2000). Indeed, the optical observations that covered the period 1989–1999 were fitted with a period of ∼1584 days (Zamanov et al. 1999), a value reported prior to the work by Gregory (2002), where the super-orbital period was refined to 1667±8 days. To investigate further the long-term modulation of LS I +61°303 at optical wavelengths and how it compares with the current findings in X-rays, we took the Hα data from Table 4 of Paredes et al. (1994), Table 1 of Zamanov et al. (1999), and Figure 1 of Zamanov et al. (2000), and as stated in Zamanov et

al. (1999), considered an error of 10% for all the equivalent widths. We performed an analysis similar to the one done for X-rays in the previous section, and derived and optical phase lag of 290.1±16.7 days with respect to the radio phase. Thus, the optical phase lag is coincident with the one derived at X-rays, although the observations at the two bands are about 8 years apart. This effect is nicely visible in Figure 3.17, where the dashed line shows the behavior of the Hα data along the superorbit. A clear correlation between the sine describing the Hα data and the sine describing the peak X-ray flux and the modulated flux fraction is evident. The stellar disk of Be stars are well known to grow larger as the equivalent width of the Hα emission line increases (e.g., Hanushik et al. 1988; Grundstrom & Gies 2006). The optical variability has been most likely attributed to the cyclic variation of Be circumstellar disk. Thus, the possible coincidence with the X-ray phase lag suggests that the stellar disk may play an important role also for the X-ray emission, and probably for the higher-energy non-thermal emission of LS I +61°303 too.

The coincidence between the X-ray and optical shift with respect to the 1667 days radio modulation has to be taken with the necessary prudence prompted by it being based on non-simultaneous observations. In particular, it seems that the optical observations present the largest degree of variation in time. We checked that in addition of the Hα measurements mentioned above, there are more recent ones in the works of e.g., Liu et al. (2005), Grundstrom et al. (2007), Zamanov et al. (2007), and McSwain et al. (2010). However, the latter span 0.51 (at best, being usually much shorter) of the super-orbital period, and as such we can not directly use them for a comparison in long-terms. Nevertheless, they seem to hint at that the Hα variability is not strictly periodic or at least at a changing amplitude.

Based (among other reasons discussed in Torres et al. 2011) on the analysis of a the *Swift*-BAT detection of a short, magnetar-like burst from the direction of LS I +61°303, we have proposed that the system's compact object is a high magnetic field, slow period pulsar. In that case, we proved that the LS I +61°303-system would most likely be subject to a flip-flop behavior, from a rotationally powered regime (in apastron, also known as ejector), to a propeller regime (in periastron) along each of the system's eccentric orbits. The multi-wavelength phenomenology can be put in the context of the former model, and in particular, also the highest energy TeV emission, which has also shown low and high states which are apparently modulated by the same super-orbital period as well. Within this model, we notice that an increase in the accreted mass onto the compact object (unavoidably linked to the mass-loss rate of the star) by a factor of a few[6] can put the system in a permanent propeller stage along the orbit, including at the apastron region. This change of behavior for such an small change in mass loss rate can be the reason behind the evolution of the modulated fraction. Indeed, using the formulae in Torres et al. (2011), and considering to simplify that the condition $R_m = R_{lc}$, where R_m stands for the magnetic radius and R_{lc} for the light cylinder, establishes both the out-of-ejector and into-ejector condition, one sees that the period–mass-loss–magnetic field relation for the apastron of LS I +61°303 is $(P/1\ \mathrm{s}) \sim a \times 15 (B/10^{14}\ \mathrm{G})^{4/7} (\dot{M}_*/10^{18}\ \mathrm{g\ s^{-1}})^{-2/7}$ where a represents a constant of order 1, and we have assumed an eccentricity of 0.6 and a semi-major axis of 6×10^{12} cm. For periods shorter than the former, the system is in an ejector phase. For larger periods, it is in a propeller stage (see Torres et al. 2011

[6]Estimations of the cyclical variations in the mass loss-rate from the Be star in LS I +61°303 are given as the ratio between maximal and minimal values obtained either from radio emission (a factor of 4 was determined by Gregory & Neish 2002) or from Hα measurements, which span from a factor of 5.6 (Gregory et al. 1989) to 1.5 (Zamanov et al. 1999).

for details). High values of magnetic field and slow periods would make the transition possible: a cyclical change by a factor of a few in $\dot{M}_*$ can make the system to abandon the ejector phase in apastron. For instance, under a variation by a factor of 4 in $\dot{M}_*$, a case that leads to a super-orbital induced transition is given by a magnetic field of 5×10^{13} G, and a typical period of magnetars (~ 7 s). This may also happen for smaller values of the magnetic field but only in the case of a relatively long period. For instance, again under a variation by a factor of 4 in $\dot{M}_*$ and for $B = 10^{12}$ G, the period should be between 700 ms and 1s in order for the system to flip-flop in the super-orbital evolution, although no known pulsar in these parameter ranges has a rotational energy in excess of 10^{36} erg s^{-1} (ATNF Catalogue version: 1.43), which would be needed to account for the multi-wavelength output of the system. Note in particular that the behavior of the LS I +61°303 system containing a pulsar with $B \sim 10^{12}$ G and $P < 700$ ms would be unaffected by the cyclical variation of the mass-loss rate: it would act as an ejector in apastron along the whole super-orbital period.

The flip-flop mechanism can then be used to qualitatively explain why LS I +61°303 has entered in a low TeV state (see, e.g., Acciari et al. 2010) when at the maximum of the radio super-orbital variability, but perhaps also to explain why the modulated X-ray flux fraction varies as we found in Figure **??**. When the mass-loss rate is low, the inter-wind shock formed at the collision region between the pulsar and the stellar wind would be present at the broad apastron region (and so will the TeV emission there), disappearing at periastron. In this situation, there are two contributors to the X-ray emission along the orbit, expected to be roughly at the same level (e.g., Zamanov et al. 1999); the shock at apastron and the propeller at periastron, and the modulated fraction is consistently low. When at the maximum of the mass-loss rate, the inter-wind shock may not form, and abundant TeV particles would not be produced since shocks at the magnetic radius are unable to reach TeV energies. Thus there is only one process generating the X-ray emission along the system's orbit, the propeller, and the modulated fraction is then maximum. The exact position of the X-ray maximum along each of the orbits would depend on the local-in-time conditions of the accreted mass onto the compact object, which established the relative weight of the two X-ray contributors, and it is thus expected to vary beyond the super-orbital trend in short timescales, and not always be located at periastron. However, given that the Hα cycle represents the cyclical modulation of the mass loss rate, it would be natural to expect that the X-ray emission be correlated with it in long timescales (i.e., with how much mass is falling towards the compact object, e.g., see Bednarek 2009 or Bednarek & Pabich 2011).

Zamanov et al. (2001) already discussed when the radio emission is expected to peak in each of the system orbits: The switch on of the ejector phase will activate the pulsar wind, creating a cavern around the neutron star which will start to expand. This means that the radio outburst will peak with some delay after the change of regimes, which is supposed to happen somewhere after the periastron, when the accretion rate onto the compact object diminishes enough. In a cyclical variability of the mass loss rate of the star, the ejector-propeller transition moves in phase: at lower mass loss rates, the ejector will switch on earlier, and the radio outburst will peak at earlier orbital phases than at higher mass loss rates. A generic TeV and radio anti-correlation is thus expected since the more mass fuels the propeller phase the more violent the radio outburst will be, and the less effectively the inter-wind shock will generate TeV particles.

The colored boxes in Figure **??** represent the times of the TeV observations that covered the broadly-defined apastron region (from Albert et al. 2006, 2008, Anderhub et al.

2009, Aleksic et al. 2011; Acciari et al. 2008, 2009, 2010). Those boxes colored in green denote the times for which the observations led only to imposing an upper-limit or to a detection with a flux that is about 3 times less than the one obtained at the discovery observations of 2006 (Albert et al. 2006), which defines the low state. The yellow boxes stand for those observations for which the level of the TeV emission was roughly compatible with the original discovery. There is a trend for finding a low TeV state towards the maximum of the super-orbital low-frequency cycles. This is perhaps more clearly seen in Figure 3.18, where we plot the peak flux per orbit in TeV (all of them happening in the 0.6–1.0 orbital phase range) as a function of superorbital phase, together with radio and Hα data. However, the scarcity (and non-simultaneity) of the TeV coverage precludes reaching a definite conclusion on whether there is an anti-correlation of the TeV emission with the radio or with the Hα curves. It would seem, however, that the TeV emission is rather anti-correlated with the radio flux and not with Hα, but this could not be quantitatively proven with the data at hand, especially given the caveats of dealing with non-contemporaneous observations. A simultaneous optical-TeV campaign is needed to establish the nature of the anti-correlation.

3.4 Pulsed fraction for high mass X-ray binaries

TO DO: CONVERT TO BIBTEX! Text has to be revised...What to show? I just did the table, not the analysis...

> The characterization of the compact objects hosted in the two TeV binaries LS I +61°303 and LS 5039 is now one long-standing question in high-energy astrophysics. In this chapter a summary of the search for pulsation of the possible X-ray pulsars in these two systems is given. Any periodic or quasi-periodic signal in the 0.3–0.4 and 0.75–0.9 orbital phases, and in a frequency range of $0.005 - 175$ Hz was found. An average pulsed fraction 3σ upper limit for the presence of a periodic signal was derived and compared with pulsed fractions from known isolated rotational-powered pulsars with detected X-ray pulsations. This chapter is based on [Rea 11].

In [Rea 10b](Paper I) it was reported on a $\sim$ 95 ks Chandra observation of LS I +61°303 aimed at gathering the most stringent limit on (or detecting) the pulsed fraction (PF) of any X-ray signal from a putative energetic pulsar. In that paper an X-ray pulsed fraction for LS I +61°303 of less than 10% (depending on the frequency and on the energy band) was inferred, while the compact object was close to the apastron of its $\sim$26 days orbit around the Be companion. Searches for pulsations from a young neutron star in massive binaries have in general many more chances of success in the X-ray than in the radio band. In fact, if the putative young neutron star is accreting, radio pulsed emission is expected to be halted by the accretion process, while if not accreting a) the X-ray pulsar beam is larger than the radio one, and b) the strong companion wind might well prevent the detection of radio pulsations because of free-free absorption and the large and highly variable Dispersion Measure (DM) induced by the wind (see e.g., Zdziarski et al. 2008).

Deep searches for pulsations have been performed in the radio band at several frequencies, with the hope of detecting a fast spinning radio pulsar as in the case of the other TeV binary, PSR B1259–63 (Johnston et al. 1999, 2005). However, no radio pulsation has been detected so far from any of these two sources. In that respect it is crucial to note that at periastron PSR B1259–63 does not show radio pulsations. Its periastron

(given the large orbit, 3.4 year period) has about the same dimension of the major axis of LS I +61°303's orbit (26 days period) and it is way larger than LS 5039 's obit (4 days period), hence it is reasonable to expect that no radio pulsed emission is observed from these much compact binaries.

Before the *Chandra* observations reported in [Rea 11] for LS 5039 and in [Rea 10b] for LS I +61°303, archival observations which could give reliable upper limits on pulsations for a possible fast spinning pulsars ($P \leq 100$ ms) hosted in LS I +61°303 and LS 5039 were not very constraining, coming mainly from *R*XTE and *XMM–Newton* observations. In particular the high background of these instruments (especially *R*XTE) limited the pulsed fraction sensitivity of these observations. For LS I +61°303 the deepest pulsed fraction limit was derived from a 41 ks *XMM–Newton* observation (Sidoli et al. 2006), which was $< 28\%$, in the 12–200 ms period range. Note that the *R*XTE monitoring observations performed in 1996 gave an upper limit of only 32% in the 1–200 ms range, in fact, even though *R*XTE's timing resolution and collecting area was much larger than *XMM–Newton*, the much higher background contamination is limiting the sensitivity to weak signals, resulting in a larger pulsed fraction limit[7]. Similarly, for LS 5039 the deepest limits for the presence of a fast pulsar were derived from a 50 ks *R*XTE observation performed in 2003, giving an upper limit of the pulsed fraction of $< 30\%$.

After collection of ∼70 ks of *Chandra* data on LS 5039 during the phases 0.3–0.4 and 0.75–0.9 in the energy range of 0.3–10 keV, no periodic or quasi-periodic signal was found. Therefore, 3σ upper limits on the sinusoid amplitude pulsed fraction (PF) as a function of frequency, computed according to Vaughan et al. (1994) and Israel & Stella (1996), between PF <13–21% were computed. Calculating the same limits as a function of the energy band, which given the lower number of counts causes the energy-dependent PF limits to be slightly larger than those derived using the whole datasets.

3.4.1 Comparison of the limits with X-ray pulsed fractions of known pulsars

The deep PF upper limits for LS 5039 and I for LS I +61°303, were used to draw a comparison between the X-ray emission of the putative pulsar in these TeV binary systems, with that of accreting pulsars in HMXBs, and isolated rotational-powered pulsars. In the HMXB case, after a thorough search in the literature, the large variability of such pulsed fractions (from a few % to 90%) as a function of luminosity and energy even in a single binary system, did not allow to draw any confident conclusion from the comparison with the limits. The large variability of the PF in these systems is probably due to the variable accretion rate, and accretion column geometry.

On the other hand, in Tab. 3.8 and Fig. 3.20 it is reported on the comparison between the X-ray PF values of all isolated rotational-powered pulsars where this value has been measured, and the limits there are for LS I +61°303 and LS 5039 . All pulsed fractions here are calculated as:

$$\frac{N_{max} - N_{min}}{N_{max} + N_{min}}$$

[7]For that observations, Harrison et al. (2000) claim a limiting pulsed fraction of ∼6%. However they considered the total count rate without correcting for the cosmic and instrumental background, which if corrected increases substantially the upper limit on the detectable pulsed fraction.

Name	log $\dot{E}_{rot}$ erg/s	log $L_x{}^{tot}$ erg/s	B-field G	Period ms	PF	Reference
B0531+21 (Crab)	38.65	37.04	3.78e+12	33.40	99.3%	Becker et al. 2002; Tennant et al. 2001; Li et al. 2
B0833-45 (Vela)	36.84	32.83	3.38e+12	89.29	6.6%	Becker et al. 2002; Halpern et al. 2001; Li et al. 2
B0633+17 (Geminga)	34.51	31.10	1.63e+12	237.09	40%	Becker et al. 2002; Caraveo et al. 2004
B1509-58 (MSH 15-52)	37.25	34.29	1.54e+13	150.23	67%	Becker et al. 2002; Kuster et al. 2002; Li et al. 20
B1929+10	33.59	30.00	5.18e+11	226.51	39.0%	Becker et al. 2002; Słowikowska et al. 2005
PSR B0950+08	32.75	29.92	2.44e+11	253.1	33.0%	Zavlin et al. 2004
B1821-24	36.35	33.24	2.25e+09	3.05	100%	Becker et al. 2002; Rutledge et al. 2004
B0656+14	34.58	32.98	4.66e+12	384.87	29%	Becker et al. 1997; Chang et al. 2001
B0540-69	38.17	36.39	4.98e+12	50.37	50%	Becker et al. 1997; Kaaret et al. 2001
J2124-33	33.55	30.35	3.22e+08	4.93	17%	Becker et al. 1997; Bogdanov et al. 2008
B1055-52	34.48	33.42	1.09e+12	197.10	25%	Becker et al. 2002; De Luca et al. 2005
J0218+4232	35.37	32.75	4.29e+08	2.32	63%	Becker et al. 2002; Kuiper et al. 2002; Mineo et al.
PSR J1617-5055	37.20	33.26	3.10e+12	69.33	47%	Becker et al. 2002; Kargaltsev et al. 2009
PSR J0030+0451	33.53	30.56	2.25e+08	4.86	33%	Becker et al. 2002
B1937+21	36.04	31.66	4.09e+08	1.55	92%	Becker et al. 2002; Nicastro et al. 2002
J0205+6449	37.42	32.31	3.61e+12	65.67	72%	Becker et al. 2002; Murray et al. 2002
J2229+6114	37.34	33.25	2.03e+12	51.62	19%	Becker et al. 2002; Halpern et al. 2001
J1930+1852	37.08	34.53	1.03e+13	136.85	2.5%	Becker et al. 2002; Leahy et al. 2008a; Lu et al. 2
J1811-1926	36.80	30.29	1.71e+12	64.67	26%	Becker et al. 2002; Torii et al. 1999
J0537-6909	38.68	36.30	9.25e+11	16.11	48%	Becker et al. 2002; Marshall et al. 1998, Wang et al.
J1420-6048	37.00	29.35	2.41e+12	68.18	35%	Becker et al. 2002; Roberts et al. 2001
PSR J1838-0655	36.70	30.92	1.89e+12	70.5	4.8%	Gotthelf et al. 2008; Lin et al. 2009
PSR J1846-0258[a]	36.9	34.89	4.86e+13	325.7	14%	Kuiper et al. 2009; Leahy et al. 2008b
PSR J1119-6127	36.40	33.00	4.10e+13	407.7	51%	Gonzalez et al. 2005
B0355+54	34.65	30.92	8.39e+11	156.38	43%	McGowan et al. 2007
B0628-28	32.17	30.00	3.01e+12	1244.42	50%	Tepedelenlıoğlu et al. 2005; Li et al. 2008
J1124-5916	37.07	34.53	1.02e+13	135.31	28%	Hughes et al. 2004; Li et al. 2008
B1706-44	36.53	32.65	3.12e+12	102.46	30%	McGowan et al. 2004; Li et al. 2008
J1747-2958	36.39	34.38	2.49e+12	98.81	29%	Hickox et al. 2009; Li et al. 2008
B1951+32	36.56	33.54	4.86e+11	39.53	1.8%	Chang et al. 1997; Li et al. 2008
J1357-6429	36.49	32.30	7.83e+12	166.1	73%	Zavlin et al. 2007

Table 3.8 Parameters for all isolated rotational-powered pulsars with detected X-ray pulsations. The $\dot{E}_{\rm rot}$ is the rotational power as derived from the rotational period and its derivative; $L_x{}^{tot}$ is the total X-ray luminosity, and the PF is defined here as $\frac{N_{max}-N_{min}}{N_{max}+N_{min}}$, where N_{max} and N_{min} are the maximum and minimum number of counts in the folded light-curve. We refer to the quoted papers for more details on $L_x{}^{tot}$ and PF, which were always in an energy range close to 0.3–10keV. The values of the the rotational power ($\dot{E}_{rot}$), B and the period were all derived from the ATNF pulsar catalog (Manchester et al. 2005). See also Fig. 3.20.

[a]Note that PSR J1846-0258 has shown magnetar–like activity (Gavriil et al. 2008; Kumar & Safi-Harb 2008), hence it should also have magnetic power contributing to its X-ray emission, rather than being "only" rotational powered.

where N_{max} and N_{min} are the maximum and minimum number of counts in the X-ray folded light-curve, respectively. It was tried to use the same X-ray band for all sources, although not for all of them the PF value was reported in the 0.3-10 keV energy range as wanted. In these few cases where only the 0.3–2 keV or 2–20 keV range were available (as e.g. for J1930+1852 which was observed by *R*XTE), it was checked that the PF values had only a marginal dependence with energy, and assumed that the same value did hold also for the 0.3–10keV energy range. Furthermore, for those sources for which in the original paper the PF was given using a different definition, the values were extraced from the pulse profile directly, such to compare PF values derived as coherently as possible. In Fig. 3.20 the values reported in Tab. **??** are plotted, using red circles for pulsars being associated with a TeV source (see also Mattana et al. 2009), and black triangles for pulsars with no detected TeV counterpart. Note that the TeV emission is mainly related to the presence of a pulsar wind nebula sustained by the energetic pulsar.

The luminosities reported in Fig. 3.20 for LS I +61°303 and LS 5039 are 7.6 and 7.5 $\times$ 10^{33}erg s^{-1} (assuming a distance of 2.3 kpc and 2.5 kpc, respectively), and were derived from the average source flux reported in [Rea 10b] and [Rea 11], hence they refer to the orbital phase ranges where such observations were performed.

At variance with what was stated in [Rea 10b], although it is true that isolated rotational powered pulsars have on average PF larger than the limits found for TeV binaries, the current detailed analysis on their X-ray pulsed fractions using a coherent definition of $\frac{N_{max}-N_{min}}{N_{max}+N_{min}}$ for all pulsars, does not seem to show a trend of higher PF values for sources with TeV counterparts.

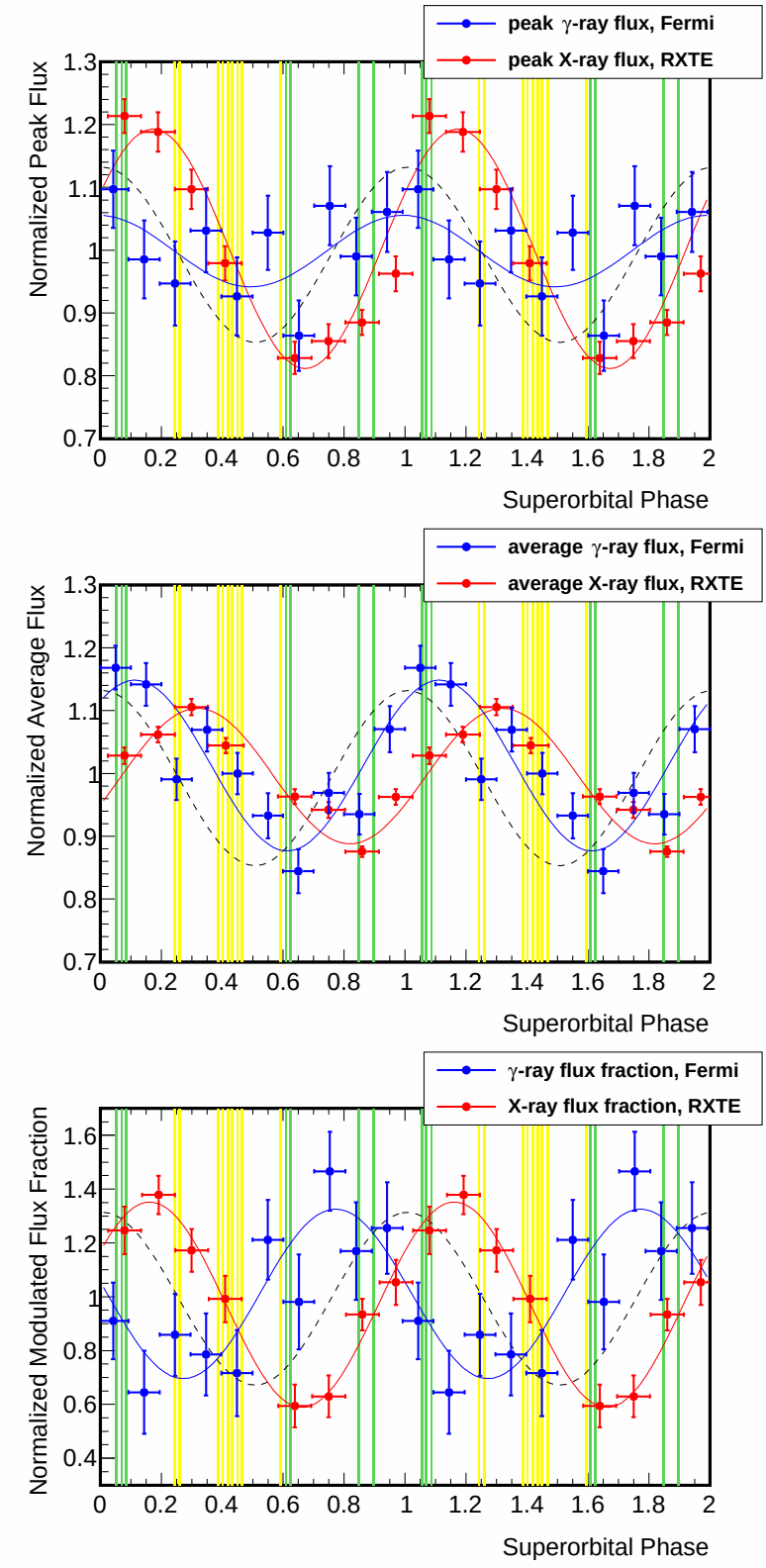

Figure 3.16 dashed line = radio.

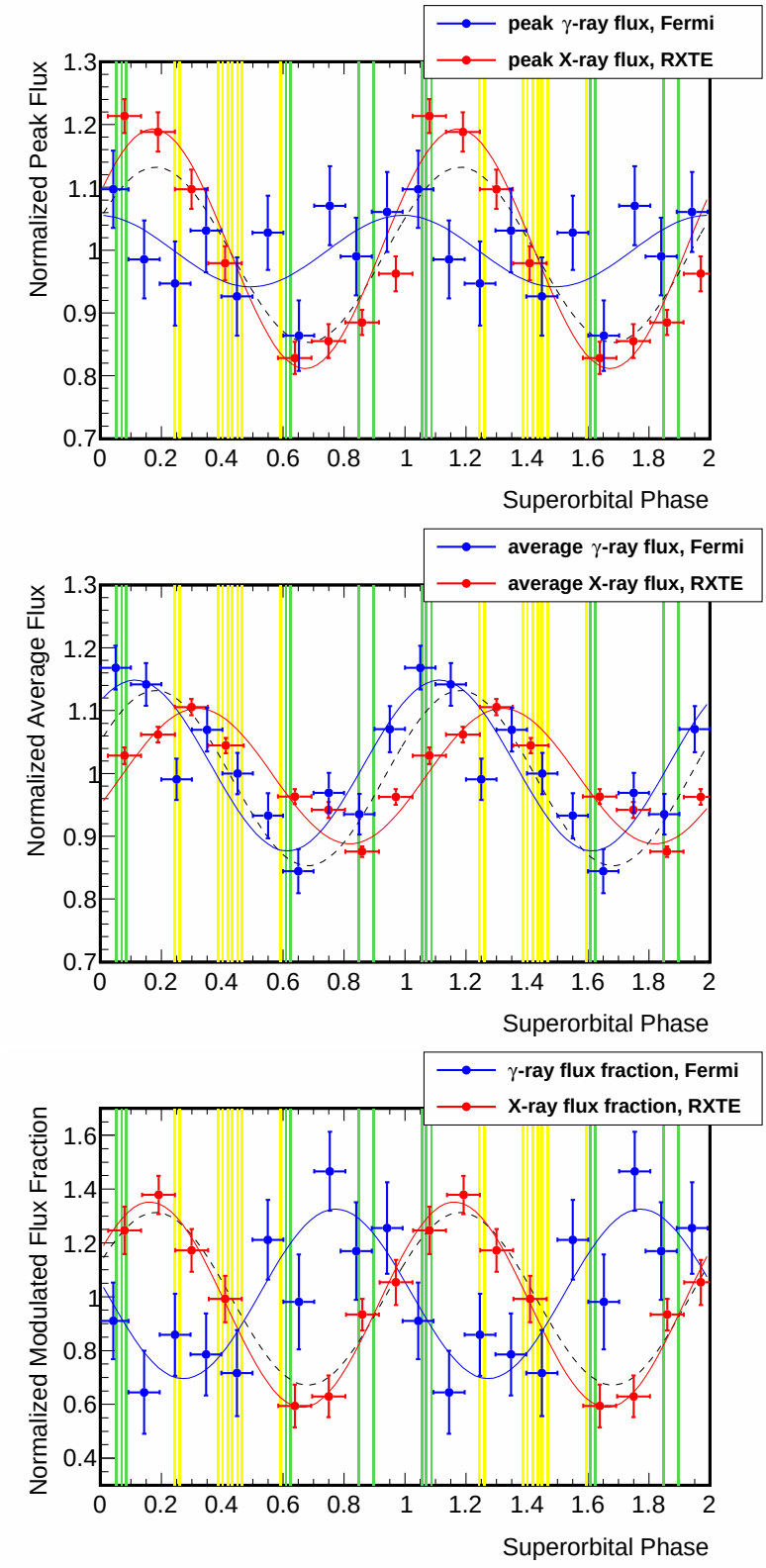

Figure 3.17 dashed line = halpha

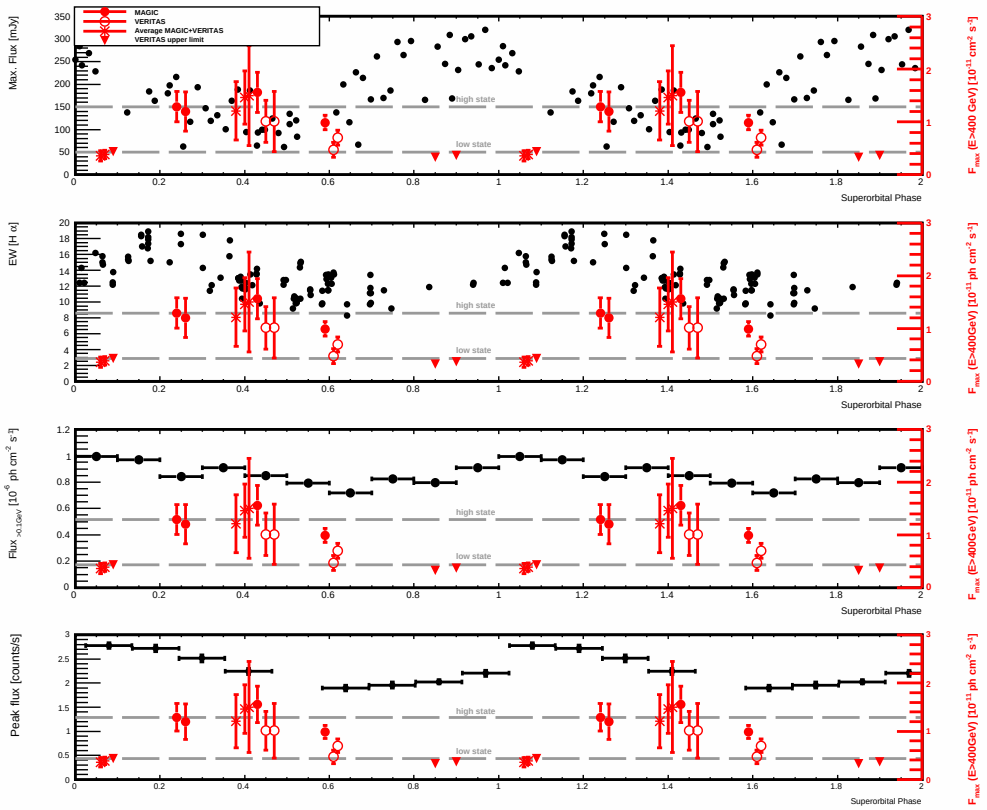

Figure 3.18 Peak flux per orbit in TeV shown in red (all of them happening in the 0.6–1.0 orbital phase range) as a function of superorbital phase, together with radio (top panel) and Hα (bottom panel) data(black) as described in the text. The upper gray dashed line stands for the TeV flux level at discovery of the source in 2006, whereas the lower dashed line stands for 1/3 of this flux value. Two super-orbital phases are shown for clarity. Whenever there are both MAGIC and VERITAS compatible observations for the same orbit, they are averaged.

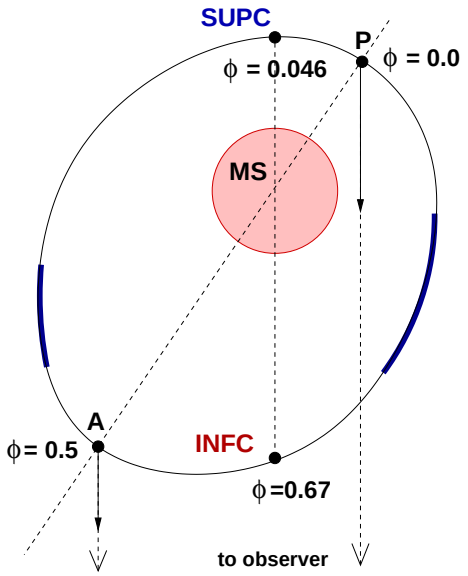

Figure 3.19 *Left panel*: LS 5039 's geometry considering the orbital solution of Aragona et al. (2009), and the phases for Inferior conjunction (INFC), Superior conjunction (SUPC), periastron (P), and apastron (A) are marked accordingly, but the inclination is not taken into account in the plot. The orbit (black solid line) and the massive star (MS; in orange) are roughly to scale. The blue thick line indicates the orbital phases spanned by our two *Chandra* observations.

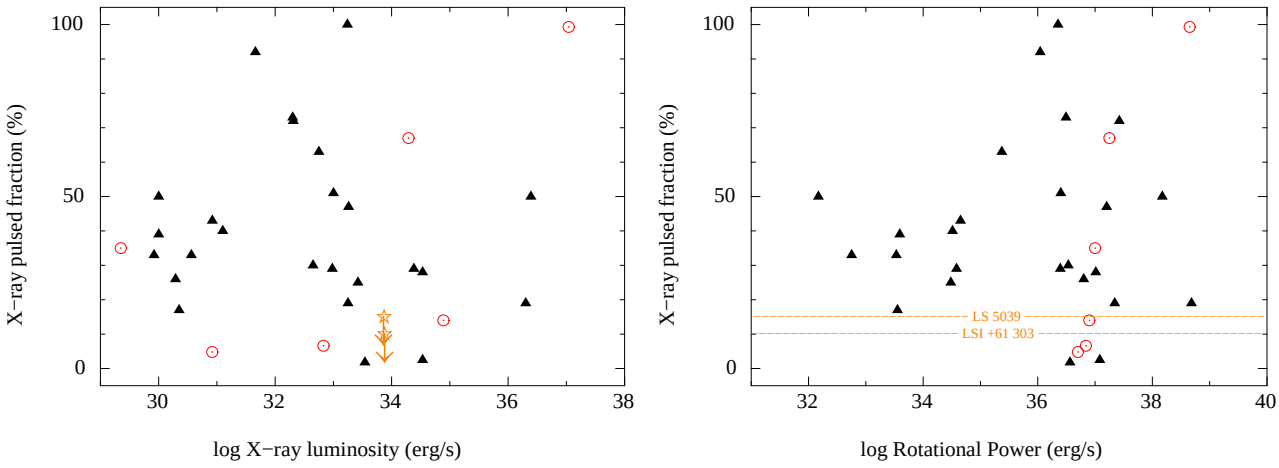

Figure 3.20 *Left panel*: Pulsed fractions versus total X-ray luminosity. *Right panel*: Pulsed fractions versus rotational power. See also Tab. 1. Circles stand for sources with associated TeV conterparts. Down arrows and horizontal lines refer to the upper limits for LS I +61°303 and LS 5039 . See § 4.2 for details.

Chapter 4

PART II: Magnetars

4.1 Overview and motivation

Magnetars are a peculiar class of neutron stars. Historically, there exist two classes of magnetars [Woods 06]: the Soft Gamma Repeaters (SGRs), discovered through their bursting activity [Kouveliotou 98], and the Anomalous X-ray Pulsars (AXPs) characterized by a strong persistent soft X-ray emission [Mereghetti 95]. During the last years it was observed that not only SGRs but also AXPs can undergo high emission states. Through further observations it became clear that the two groups share their characteristic properties and are now recognized as part of the same class [Kaspi 03, Rea 09, Mereghetti 09, Israel 10].

The differences but also the similarities to ordinary radio pulsars can be seen in Figure 4.1. There, all known magnetars are shown together with the ordinary radio pulsars in the so-called P–$\dot{P}$ diagram. Almost all of the about 20 known magnetars have strong dipolar magnetic fields ($\sim 10^{14} - 10^{15}$ Gauss) which are $\sim 10 - 1000$ times higher than the average value in radio pulsars, and higher than the quantum electrodynamic field strength, $B_{\rm QED} = m_e^2 c^3 / e\hbar \sim 4.4 \times 10^{13}$ G, which is shown as the grey dash-dotted line in Figure 4.1. They have bright X-ray luminosities ($L_{\rm x} \sim 10^{32} - 10^{36}\,{\rm erg\,s^{-1}}$), strong soft (0.1 – 10 keV) and hard X-ray (10 – 300 keV) emission, rotation periods longer than most ordinary pulsars ($\sim$ 2–12 s) and period derivatives of $\sim 10^{-13}$–10^{-11} s/s. Pulsed radio emission was detected from a few of them [Camilo 06].

Recently, one of the key properties of magnetars has been revised. [Rea 10a] found a neutron star with magnetar properties owing a surface dipolar magnetic field as low as a few times 10^{12} G, which is in line with rotation-powered pulsars and below the quantum critical field ($B_{\rm Q}$) mentioned above. Another example of this kind is the transient Swift J1822-1606 discovered in July 2012 [Rea 12]. These discoveries show that a surface dipolar magnetic field larger than $B_{\rm Q}$ is not needed anymore to define an object a magnetar. Now even many normal pulsars can turn out as magnetars at anytime through burst activities.

The nature of the X-ray emission coming from magnetars, typically best modeled with a blackbody plus a power law and an additional power law at higher energies, cannot be explained in terms of the common scenarios for the radio pulsar or the X-ray binary pulsar populations. The emission is too high to be supplied by the rotational energy

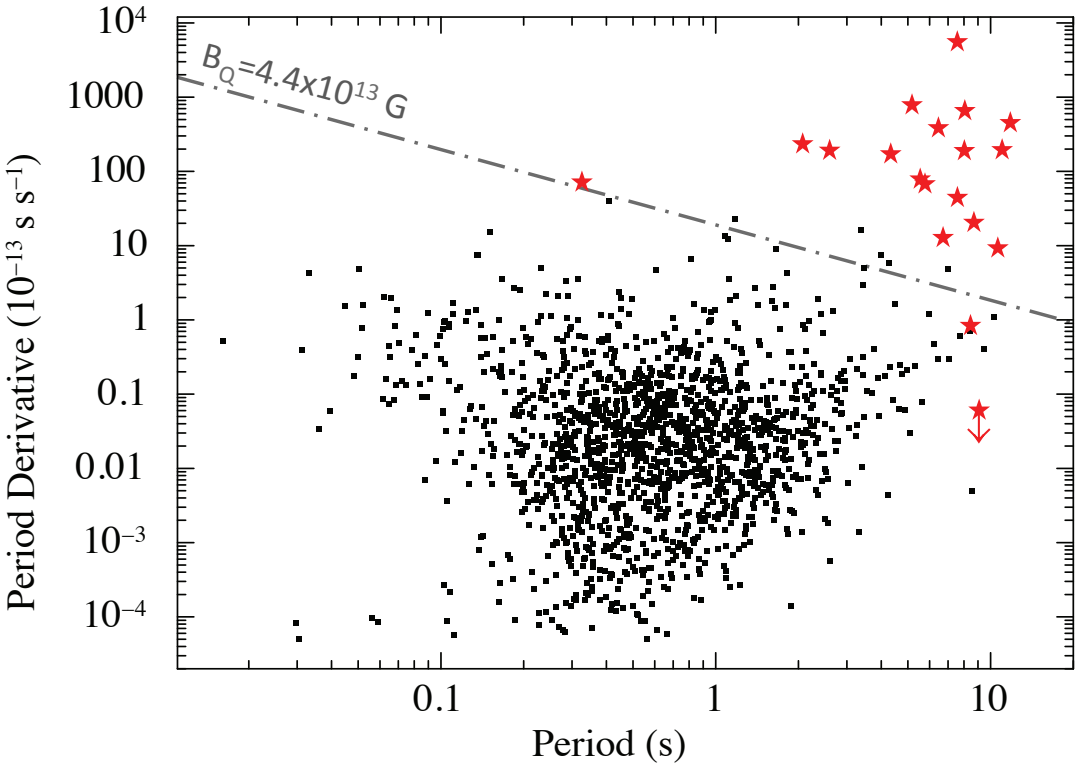

Figure 4.1 P–$\dot{P}$ diagram for all known isolated pulsars. Black squares represent normal radio pulsars, and red stars are all pulsars showing magnetar-like emission. The two newly discovered low-B magnetars: Swift J1822.3–1606 (Rea et al. 2012), and SGR 0418+5729 are also reported, as well as the electron quantum magnetic field (dash-dotted grey line). Figure taken from [Rea 13].

alone (as in radio pulsars) and no evidence for a companion star has been found so far to support an accretion scenario (as in the X-ray binary systems). The most successful model was up to now the "magnetar" model, in which the X-ray emission of the neutron star is believed to be powered by the decay and the instabilities of their strong magnetic field [Duncan 92, Thompson 93, Thompson 95].

The apparent dichotomy between the strong magnetic field magnetars and weaker field ordinary pulsars may arise from having different progenitors. The most popular idea is that magnetars are thought to form through a magnetic amplification via an alpha-dynamo which was active during the proto-neutron star phase lasting maximum 10 s after the supernova explosion [Duncan 92, Thompson 93, Thompson 96]. For this process to be at work, the proto-neutron star rotational period is required to be between 0.6–3 ms [Thompson 96]. This scenario requieres a supernova explosion which is one order of magnitude more energetic than normal supernovae. This is so far not supported by the observations of supernova remnants (SNRs) a few magnetars are associated with [Vink 06]. What remains unexplained is where the huge rotational energy at birth ($\sim 5 \times 10^{52}$ erg) that magnetars should have in excess with respect to normal radio pulsars goes. Since SNRs surrounding magnetars were not measured in X-rays to be more energetic than those hosting normal pulsars, with this work is was aimed at testing whether this additional energy at birth could have gone in TeV emission.

Neither of the known magnetars are detected at energies above hundreds of keVs.

Our current knowledge of their spectra at much higher energies (>0.5 MeV) is very limited. Archival studies of *COMPTEL* observations were used to place upper limits on the emission of a few magnetars in the 0.75-30 MeV range, of $\sim 10^{-10}$erg s^{-1}cm^{-2}at a 2σ level (Kuiper et al. 2006). Very poor so far is the knowledge concerning their behavior at energies >30 MeV (Heyl & Hernquist 2005), a band of interest given model predictions of measurable synchrotron/curvature emission (Chang & Zheng 2001; Zhang & Cheng 2002).

Recently, the H.E.S.S. collaboration presented their discovery of extended TeV γ-ray emission towards the magnetar SGR 1806-20 [Rowell 11]. It is not certain that the emission is driven by the magnetar that is possibly part of the stellar cluster C1 1806-20. Both the magnetar and the stellar cluster are embedded in a synchrotron radio nebula (G10.0–0.3) [Kulkarni 94]. However, it cannot be ruled out that the magnetar contributes to the emission observed.

In Chapter 4.2 a search for the emission at very high energies (200 GeV–5 TeV) from the two magnetars 4U 0142+61 and 1E 2259+586 with the MAGIC telescopes is presented. Both sources have also been observed by the VERITAS Collaboration and corresponding upper limits above an energy of 400 GeV have been derived [Guenette 09]. MAGIC observations allowed for a lower energy threshold down to 200 GeV.

In Chapter 4.3 a search for the emission at high energies (100 MeV–300 GeV) from all known magnetars in our Galaxy with the *Fermi* Large Area Telescope (LAT) is shown.

4.2 Magnetars observations at TeV with the MAGIC telescopes

Magnetars are an extreme, highly magnetized class of isolated neutron stars whose large X-ray luminosity is believed to be driven by their high magnetic field. The aim of the following work is to study for the first time the possible very high energy γ-ray emission above 100 GeV from magnetars, observing the sources 4U 0142+61 and 1E 2259+586. The two sources were observed with atmospheric Cherenkov telescopes in the very high energy range (E> 100 GeV). 4U 0142+61 was observed with the MAGIC I telescope in 2008 for ∼25 h and 1E 2259+586 was observed with the MAGIC stereoscopic system in 2010 for ∼14 h. The data were analyzed with the standard MAGIC analysis software. Neither magnetar was detected. Upper limits to the differential and integral flux above 200 GeV were computed using the Rolke algorithm. The obtained integral upper limits to the flux are 1.52×10^{-12}cm^{-2} s^{-1} and 2.7×10^{-12}cm^{-2} s^{-1} with a confidence level of 95% for 4U 0142+61 and 1E 2259+586, respectively. The resulting differential upper limits are presented together with X-ray data and upper limits in the GeV energy range. This chapter is based on [Aleksić 13].

4.2.1 The observed magnetars

The source 4U 0142+61 is located at $\alpha_{2000}, \delta_{2000} = 01^{\rm h}46^{\rm m}22\overset{\rm s}{.}407, +61°45'03\overset{''}{.}19$ at a distance of $\sim$ 3.6 kpc. With an X-ray luminosity of $L_{\rm X} \sim 1 \times 10^{35}$erg s^{-1} it is one of

the most X-ray luminous magnetars known [McGill Pulsar Group 12]. This makes it a good target to search for persistent very high energy emission. Long term spin period variations ($P \sim 8.7\,\mathrm{s}$) were discovered during observations with *EXOSAT* [Israel 94], leading to the measurement of the period derivative $\dot{P} \sim 2\times10^{-12}\mathrm{ss}^{-1}$, and consequently of the very strong magnetic field $B \sim 1.3\times10^{14}\mathrm{G}$ [McGill Pulsar Group 12]. The bright 1-10 keV emission coming from 4U 0142+61 has been observed by many X-ray satellites [White 87, Israel 99, Patel 03, Rea 07a, Rea 07b] revealing an X-ray spectrum typical of an Anomalous X-ray Pulsar (AXP), best described by an absorbed blackbody plus a power law ($N_\mathrm{H} \sim 10^{22}\mathrm{cm}^{-2}, kT \sim 0.4\mathrm{keV}$ and $\Gamma \sim 3.62$). A very strong hard X-ray emission has been reported by *INTEGRAL* up to 250 keV, with a spectrum well modeled with a steep power-law with a photon index of $\sim$1 [Kuiper 06]. At the time of data taking with the MAGIC telescope, there were only *COMPTEL* upper limits in the MeV range suggesting a spectral break in the hard X-ray emission of this object. The upper limits, however, do not put strong constraints on the HE or VHE gamma-ray emission of the object, especially given the high systematic uncertainty of the background subtraction in the data COMPTEL analysis [Schönfelder 04]. Recently, the upper limits derived by the *Fermi*-LAT Collaboration [Abdo 10] and by [Şaşmaz Muş 10] point to a cutoff in the MeV band.

The AXP 1E 2259+586 is located at $\alpha_{2000}, \delta_{2000} = 23^\mathrm{h}01^\mathrm{m}08\overset{\mathrm{s}}{.}296, +58°52'44\overset{''}{.}45$ embedded in the SNR CTB109. The source has a magnetic field of $B \sim 0.59\times10^{14}\mathrm{G}$ and a distance of $\sim$4 kpc, making it a good candidate for MAGIC observations [McGill Pulsar Group 12]. *RXTE* measured the period ($P \sim 7\,\mathrm{s}$) and the period derivative ($\dot{P} \sim 0.5\times10^{-12}\mathrm{ss}^{-1}$) [Gavriil 02]. The X-ray spectrum is variable depending on the source emission state [Kaspi 03, Woods 04]. After undergoing an outburst in 2002, the source returned into its possible quiescence state and the corresponding spectrum is best fitted by a blackbody plus a power law ($N_\mathrm{H} \sim 10^{22}\mathrm{cm}^{-2}, kT \sim 0.4\mathrm{keV}$ and $\Gamma \sim 3.75$) [Zhu 08].

4.2.2 Analysis and Data

Like described in Chapter 2 the MAGIC Collaboration operates two 17 m diameter imaging atmospheric Cherenkov telescopes. The data sets presented here were taken in 2008, i.e. before the second MAGIC telescope was operational (mono data), and in 2010 when both telescopes were already taking stereoscopic data. Details about the performance of MAGIC in mono and stereo mode can be found in [Albert 08] and [Aleksić 12]. All data presented in this work were taken in the so-called wobble mode and were analyzed using the MARS analysis framework [Moralejo 09, Aleksić 12]. The analyses presented here have an analysis threshold of 200 GeV. The upper limits were calculated using the Rolke algorithm [Rolke 05] with a confidence level (C.L.) of 95% assuming a Gaussian background and 30% of systematic uncertainty in the flux level. Since 1E 2259+586 is embedded in a SNR and may contain more than one emission region (see below) relevant parameters for the observations are the MAGIC field of view of 3.5° and the angular resolution of $\sim$0.07° above 300 GeV [Aleksić 12].

4U 0142+61 was observed for 25.41 hours. After quality cuts 16.58 hours of effective observation time remain. These mono data were taken between August and December 2008 covering a zenith angle range between 33° and 40.6°.

Data for 1E 2259+586 were taken in stereo mode wobbling around the sky position 0.12° away from the magnetar to have the shell of the supernova remnant and the magnetar

in the same field of view. Given the angular resolution of the MAGIC telescopes, these two possible TeV sources would be spatially separable with MAGIC. The region was observed between August and November 2010 for 14.33 hours within a zenith angle range of 29°–43°. After quality cuts this amounted to 8.22 hours of effective observation time.

Table 4.1 Magnetar parameters taken from [McGill Pulsar Group 12], along with the MAGIC results presented here. Crab Units (C.U.) are defined as a fraction of the Crab Nebula flux as measured by MAGIC [Aleksić 12].

Source	Distance [kpc]	$B_{\rm surf}$ [10^{14}G]	$L_{\rm X}$ [10^{35}erg s^{-1}]	$\log(L_{\rm rot})$ [erg s^{-1}]	Eff. obs. time [hrs]	Significance σ	Upper limit (95% C.L., E>200 GeV) [cm^{-2} s^{-1}]
4U 0142+61	3.6±0.4	1.3	1.1	32.10	16.58	−2.1	1.52×10^{-12} (0.70% C.U.)
1E 2259+586	4.0±0.8	0.59	0.34	31.70	8.22	−0.5	2.70×10^{-12} (1.24% C.U.)

4.2.3 Results

Neither source was detected by MAGIC. We computed the integral flux upper limits above 200 GeV with 95% C.L. assuming a differential energy spectral shape of a power law with an index of 2.6, similar to that of the Crab Nebula spectrum. The results are given in Table 4.1. A 25% change in the photon index yields a variation of about 7%. In Fig. 4.2 we show the corresponding test statistic (TS)[1] map for 1E 2259+586. No excess was found at either the magnetar position nor at any location within the surrounding SNR. The TS map for 4U 0142+61 is not shown here, but shows the same flat behaviour. The white contours represent the X-ray emission of the surrounding SNR detected with the *XMM-Newton* satellite (0.1–15 keV). We also searched for pulsations for both magnetars. For the pulsed analysis of 1E 2259+586 we used a timing solution valid at the epoch of the MAGIC observations, as derived by [Içdem 12]. We did not detect any significant pulsation at VHE energies. In the case of 4U 0142+61, we searched for pulsation using the ephemeris of [Şaşmaz Muş 10]. We did not find any pulsation at VHE energies for this source either.

Since neither source experienced an outburst in X-rays during our observing intervals, we can compare our upper limits with data taken with different instruments during different quiescent epochs. In Fig. 4.3a (4.3b) we present the 0.1 keV–3 TeV multi-band spectral energy distribution (SED) of 4U 0142+61 (1E 2259+586), respectively. For both sources the corresponding differential and integral upper limits derived in this work are shown (red lines in Fig. 4.3). In the case of 4U 0142+61, the 0.1–200 keV data are from *XMM*-Newton-PN and *INTEGRAL*-ISGRI [Rea 07a, den Hartog 08, Gonzalez 10] plotted together with the 2σ COMPTEL upper limits [den Hartog 06, Kuiper 06]. For 1E 2259+586 we show data points from *XMM*-Newton-PN [Woods 04] together with COMPTEL upper limits [Kuiper 06]. The upper limits provided by the *Fermi*-LAT Collaboration were calculated for three different energy ranges [Abdo 10] and are presented in the next chapter. For the overall energy bin from 0.1–10 GeV a photon index of 2.5 was assumed. A cutoff is mimicked by splitting this energy bin into two parts with photon indices of 1.5 and 3.5, respectively. The assumed slopes are indicated in Fig. 4.3. The results derived by the VERITAS Collaboration on the two sources are also shown for comparison (grey dashed lines). They correspond to 99% C.L. integral flux upper

[1] Our test statistic is [Li 83] eq. 17, applied on a smoothed and modeled background estimation. Its null hypothesis distribution mostly resembles a Gaussian function, but in general can have a somewhat different shape or width.

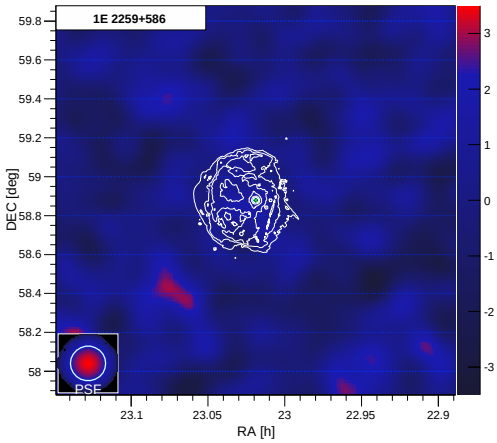

Figure 4.2 TS map of 1E 2259+586. The green cross represents the magnetar position. The white contours show the X-ray emission of the surrounding SNR CTB 109 detected with the *XMM-Newton* satellite. The color scale represents the TS value.

limits of $8.68 \times 10^{-13}\mathrm{cm}^{-2}\mathrm{s}^{-1}$ for 4U 0142+61 and $2.49 \times 10^{-12}\mathrm{cm}^{-2}\mathrm{s}^{-1}$ for 1E 2259+586 by assuming a power-law with a photon index of 2.5 above 400 GeV [Guenette 09]. The upper limits for both sources are compatible with a break in the power law at ∼1 MeV. However, the SED lacks any measurements above hard X-rays, what gives complete freedom under the corresponding instrumental sensitivity.

[Cheng 01] presented a model for the very high energy radiation from magnetars. They predicted emission of γ-rays in the GeV band coming from the outer gap for the two sources we studied. This model has been recently revised by [Tong 11], who updated the observational parameters to calculate the γ-ray radiation properties of all AXPs and SGRs using the models by [Zhang 97] and [Cheng 01]. The scenario by [Tong 11] predicts that 4U 0142+61 should have been detected by *Fermi*-LAT, although they explain the lack of a detection by Fermi-LAT [Abdo 10, Şaşmaz Muş 10] by invoking accretion. For 1E 2259+586 the model does not predict GeV emission. We note that although none of the current models predict TeV range emission for either magnetar, the existence of diffuse emission around 1E 2259+586 could lead to the appearance of an extra component in the SED besides any magnetospheric emission.

Using the MAGIC telescopes we studied for the first time the possibility of magnetars to be a new TeV source class on the examples of 4U 0142+61 and 1E 2259+586. This exploratory work led to a non-detection of the VHE gamma-ray emission from either of them. This result indicates that magnetars are probably not VHE emitters during their quiescent state, as expected from the various theoretical models. However, the possibility of magnetars being VHE emitters during flaring episodes cannot be ruled out because of the lack of VHE observations during these high-activity periods. Consequently, our future searches for VHE emission of magnetars will be performed during outbursts [2].

[2] In order to provide fast reactions to such events in the future, MAGIC has installed an alert system, which receives alerts provided by several satellites and points the telescopes to the flaring source automatically, as it is also done for observations of Gamma Ray Bursts.

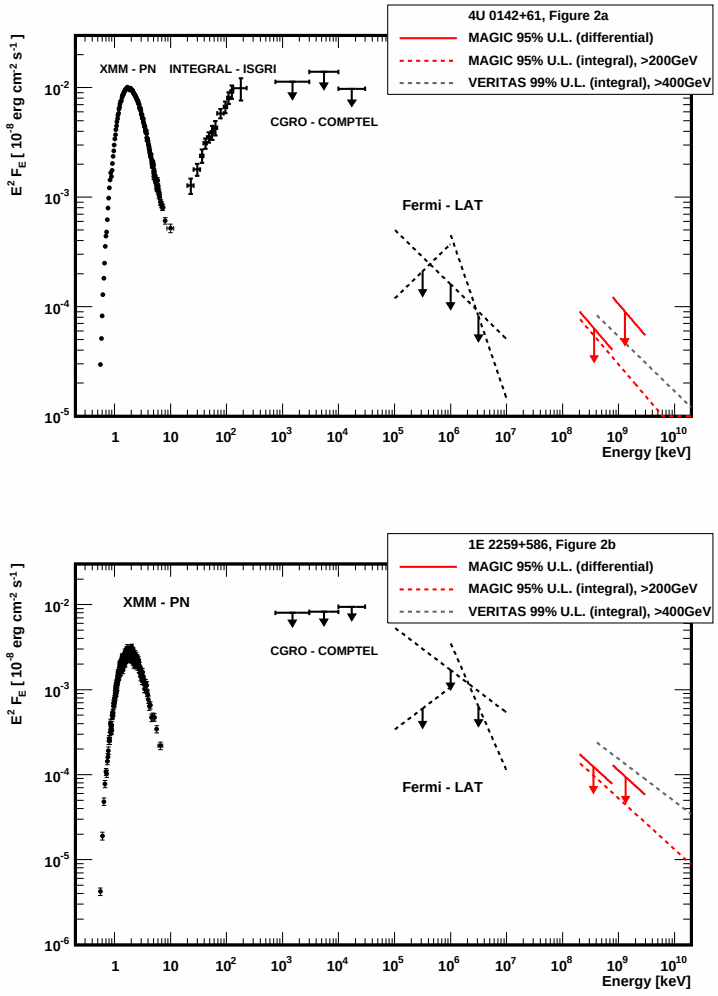

Figure 4.3 Spectral energy distributions of 4U 0142+61 (2a) and 1E 2259+586 (2b) from X-rays to TeV energies. In black the points and upper limits in the keV up to the GeV energy range are shown. The upper limits derived by the VERITAS Collaboration are shown in gray and the upper limits from this work are shown in red. See text for further details on the data and upper limits presented here.

Table 4.2. *Fermi*-LAT upper limits on magnetars obtained from likelihood analysis.

Source	d* kpc	log(B) Gauss	log(L_X)* erg s^{-1}	log(L_{rot}) erg s^{-1}	TS	0.1–10 GeV ($\Gamma = 2.5$)	0.1–1 GeV ($\Gamma = 1.5$)	1–10 GeV ($\Gamma = 3.5$)	1FGL srcs within 3°
1E 1048.1−5937	3.0	14.78	34.00	33.90	0.0	<5.3 (12.0)	<3.9 (7.7)	<1.7 (0.7)	7
SGR 1900+14	15	14.81	35.44	34.34	0.0	<0.4 (0.9)	<0.8 (2.0)	<0.6 (0.2)	5
SGR 0418+5729	2.0	<12.70	31.77	<29.47	2.3	<0.4 (0.9)	<0.2 (0.4)	<0.1 (0.04)	2
SGR 1806–20	8.7	15.15	35.21	34.40	2.8	<0.6 (1.4)	<0.5 (0.9)	<0.12 (0.05)	1
4U 0142+614	5.0	14.11	35.32	32.10	3.6	<0.9 (2.0)	<0.5 (0.9)	<0.3 (0.11)	1
1E 1841−045	8.5	14.85	35.34	32.99	7.5	<3.0 (6.0)	<6.3 (13.0)	<2.4 (0.92)	8
XTE J1810–197	4.0	14.46	33.58	33.60	13.1	<5.0 (10.0)	<12.0 (23.0)	<2.0 (0.7)	7
1E 2259+586	3.0	13.76	34.43	31.70	15.6	<1.7 (3.9)	<0.6 (1.0)	<0.63 (0.24)	2
SGR 0501+4516	5.0	14.23	34.77	33.49	16.3	<1.9 (4.3)	<0.6 (1.0)	<0.5 (0.18)	1
1RXS J1708−4009	8.0	14.67	35.27	32.75	32.1	<10.0 (20.0)	<5.0 (9.0)	<9.0 (4.0)	8
CXOU J1647–4552	5.0	14.20	34.41	31.89	33.7	<10.0 (20.0)	<10.0 (20.0)	<19.0 (7.2)	7
SGR 1627–41	11	14.34	33.39	34.63	36.0	<20.0 (50.0)	<20.0 (30.0)	<5.0 (2.0)	8
1E 1547−5408	9.0	14.32	34.16	35.00	36.2	<10.0 (20.0)	<7.9 (16.0)	<2.1 (0.8)	6

Note. — Properties of the magnetars studied in this work ordered by the measured TS values derived from the binned analysis (for further info on the first 4 columns see Mereghetti (2008) and reference therein; Rea et al. (2009, 2010) for the newly discovered SGR 0501+4516 and SGR 0418+5729, respectively). The GeV upper limits are reported at 95% confidence level (see Sect. 4.3.4 for details). Fluxes are in units of 10^{-11}erg s^{-1}cm^{-2}(or 10^{-8} photons cm^{-2} s^{-1} for numbers in brackets). The last 4 sources and 1E 1841−045 are discussed in detail in the text. * Note that most of the sources have very variable X-ray luminosities, and very uncertain distances, hence those values should be taken as indicative.

4.3 Magnetars observations at GeV with the *Fermi* Large Area Telescope

IN THIS WHOLE SECTION PUT REFERENCE IN BIBTEX FORMAT!!!

In this chapter it is reported on the search for 0.1–10 GeV emission from magnetars in 17 months of *Fermi* Large Area Telescope (LAT) observations. No significant evidence for gamma-ray emission from any of the currently-known magnetars is found. The most stringent upper limits to date on their persistent emission in the *Fermi* energy range are estimated between $\sim 10^{-12} - 10^{-10}$erg s^{-1}cm^{-2}, depending on the source. It was also searched for gamma-ray pulsations and possible outbursts, also with no significant detection. The upper limits derived support the presence of a cut-off at an energy below a few MeV in the persistent emission of magnetars. They also show the likely need for a revision of current models of outer gap emission from strongly magnetized pulsars, which, in some realizations, predict detectable GeV emission from magnetars at flux levels exceeding the upper limits identified here using the *Fermi*-LAT observations. This chapter is based on the work [Abdo 10].

4.3.1 Observation and data reduction

The data analyzed here were taken in survey mode with the *Fermi* Large Area Telescope, from 4 August 2008 until 1 January 2010. We analyzed the data using the Fermi Science Tools `v9r15` package. Events from the "Pass 6 Diffuse" event class are selected, i.e. the event class with the greatest purity of gamma rays, having the most stringent background rejection (Atwood et al. 2009). The "Pass 6 v3 Diffuse" instrument response functions

(IRFs) are applied in the analysis. For each analyzed source we select events with energy E>100 MeV in a circular region of interest (ROI) of 10° radius. The good time intervals are defined such that the ROI does not go below the gamma-ray-bright Earth limb (defined at 105° from the Zenith angle), and that the source is always inside the LAT field of view, namely in a cone angle of 66°.

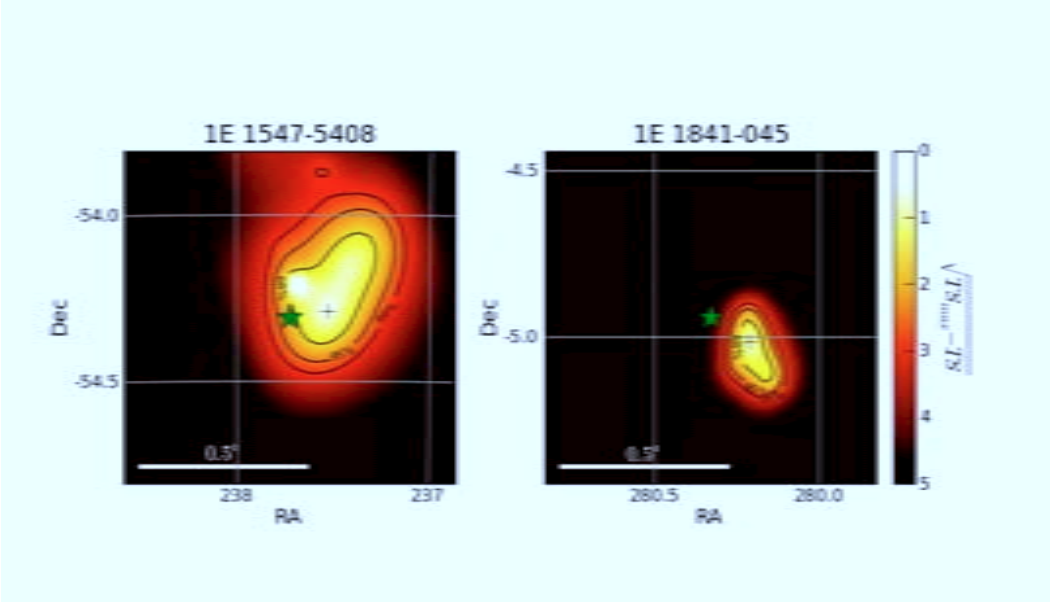

Figure 4.4 Test Statistic maps of the *Fermi*-LAT fields of 1E 1547−5408 and 1E 1841−045 (RA and Dec are referenced at J2000). The green stars represent the X-ray position of each magnetar. TS_{max} is the maximum TS value inferred around the two magnetars, measured in the position labelled by the crosses. Solid lines are the positional confidence levels around the maximum TS value in each field of view. See text for details.

4.3.2 Likelihood analysis and results

Gamma-ray emission was analyzed at the positions of all the magnetars known in 2010, excluding yet unconfirmed candidates. Extragalactic magnetars located in the Large and Small Magellanic Clouds are also excluded due to their large distances and the difficulty of resolving them from their host galaxies (see Abdo et al. 2010, 2010a). See Table 4.2 for the 13 selected magnetars.

The Test Statistic was employed to evaluate the significance of the gamma-ray fluxes coming from the magnetars. The TS value is used to assess the goodness of a fit, and it is defined as twice the difference between the log-likelihood function maximized by adjusting all parameters of the model, with and without the source, and under the

assumption of a precise knowledge of the Galactic and extragalactic diffuse emission. A TS=25 roughly corresponds to a 4.6σ detection significance (Abdo et al. 2010b).

Binned and unbinned likelihood analysis are applied on the data, using the official tool (`gtlike`) released by the *Fermi*-LAT collaboration. The binned likelihood uses events selected in a square inscribed inside the circular ROI (see § 2), aligned with celestial coordinates.

For each magnetar, a spectral-spatial model containing diffuse and point-like sources is created, and the parameters are obtained from a maximum likelihood fit to the data. For the Galactic diffuse emission we use the spectral-spatial model "gll_iem_v02.fit", used by the *Fermi* collaboration to build the First *Fermi* Source Catalog (Abdo et al. 2010b; 1FGL hereafter). The extragalactic diffuse emission was modeled as an isotropic emission using the spectrum described in the "isotropic_iem_v02.txt" file[2]. This spectrum also takes into account the residual background of charged particles in the LAT.

In the spectral-spatial model of each magnetar we fixed its position at the localization determined by X-ray observations (in all cases with uncertainties $<2''$; see Mereghetti 2008 and the McGill catalog[3]), and also included all the point-like sources from the 1FGL list closer than 15°. Each of those point sources was modeled with a simple power-law, with the exceptions of the pulsars closer than 3° from the magnetars, for which a power-law with an exponential cut-off was used. The spectral parameters of those sources were fixed at the 1FGL values or those from the *Fermi*-LAT First Pulsar Catalog (Abdo et al. 2010c), while the flux parameters of all the point-like sources closer than 3° to the magnetar were left free in the likelihood fit (see also Table 1, last column).

We modeled the magnetar emission using power-law spectral distributions with two free parameters: the flux and spectral index. The likelihood ratio test indicated values of TS less than 25 for most of the analyzed magnetars (see Table 1). For 1RXS J1708−4009, CXOU J1647–4552, and 1E 1547−5408 the calculated TS values were in the range 25–50, while SGR 1627–41 and 1E 1841−045 had TS>70. The latter cases are addressed in Sect. 4.3.3.

For those magnetars for which X-ray outbursts were detected during the *Fermi*-LAT observing period (namely SGR 0501+4516, SGR 0418+5729 and 1E 1547−5408; e.g. Rea et al. 2009; Esposito et al. 2010; Israel et al. 2010), we re-ran the analysis considering subsets of data taken one day, one week or two weeks around the peaks of their X-ray outbursts. All TS values during those outbursts were <25.

4.3.3 Sources with high TS values

Given the relatively high TS values found in five cases by the likelihood analysis, we checked whether the X-ray positions of these magnetars are compatible with the most probable origin of the gamma-ray excesses. For this purpose, we performed a localization process similar to the one used for the 1FGL catalog, using the `pointlike` tool, which returns the TS map around each source, where the TS is calculated at any putative source position. See Figure 4.4 for two examples of these maps, around 1E 1547−5408 and 1E 1841−045. This tool is applied leaving as free the spectral parameters of the

[2] All the data, software, and diffuse models used for this analysis are available from the Fermi Science Support Center. http://fermi.gsfc.nasa.gov/ssc/

[3] www.physics.mcgill.ca/∼pulsar/magnetar/main.html

modeled sources within 1° of each magnetar. The results for the magnetar positions with TS> 25 are summarized below. We remember here that all these high-TS sources are in the inner Galaxy close to the Galactic plane, where the diffuse emission is strong and highly structured, and this could affect our results.

1E 1841−045

The `gtlike` analysis of 1E 1841−045 resulted in a high TS value (> 70). In this case the `pointlike` TS map showed a new source very close to the magnetar at an angular distance of 0.11° (RA=280.23°, Dec=-4.99°. See Figure 4.4 right panel). This source is not present in the 1FGL catalog, probably due to the longer time interval analyzed here (17 months vs. 11 months for 1FGL). The TS value of 1E 1841−045 falls below 25 when the new source is added to the spectral-spatial model used for the likelihood analysis, and thus we find no evidence to claim the magnetar as a gamma-ray emitter.

SGR 1627–41

The `pointlike` analysis for SGR 1627–41 indicated that the position of the magnetar was not a maximum of TS when the coordinates of the modeled source were optimized in the fit. In particular, we found that the high TS derived by the `gtlike` analysis could have been caused by the presence of the rather strong unidentified source (1FGL J1636.4-47371), which lies as close as 0.12° from the magnetar (although positionally incompatible with it). If the spectral parameters of the modeled 1FGL sources are held fixed at their values in the 1FGL catalog, SGR 1627–41 ends up having a TS∼36. This is what is reported in Table 4.2. While this is still greater than 25, the flatness of the TS map around this source suggests that in this region the diffuse Galactic emission could be underestimated by the model adopted in the likelihood analysis.

1RXS J1708−4009 and CXOU J1647–4552

The `gtlike` analyses of these two magnetars resulted in TS values of ∼30 for both sources. For each source we performed a `pointlike` analysis which in both cases indicated that the position of the two magnetars were not a maximum of TS when the coordinates of the modeled source were optimized in the fit. We cannot exclude that the likelihood excesses of 1RXS J1708−4009 and CXOU J1647–4552 are caused by the uncertainties of the Galactic diffuse model.

1E 1547−5408

1E 1547−5408 is the only source for which the TS map calculated by `pointlike` indicated that the position of the magnetar was indeed consistent with a local maximum of TS (see Figure 4.4 left panel). In particular, 1E 1547−5408 has a TS∼35, and it is observed inside the 95% positional error contour around the TS_{max} of the field. With the current *Fermi* observations a firm association between this excess and 1E 1547−5408 cannot be made. Furthermore, we found that the TS of 1E 1547−5408 falls below 20 if the level of the Galactic diffuse emission is increased by only 2%.

4.3.4 Upper limits evaluation

Before starting with the upper limit determination, we note that for all but one magnetar, the local maximum of TS was not coincident with the magnetar position. Furthermore, by increasing the level of the Galactic diffuse emission by 2-4%, all of the TS values determined would decrease below 20. These percentages are well inside the systematics of the assumed Galactic diffuse emission model (see the cases of the supernova remnants W51C and W49, and § 4.7 of the 1FGL catalog; Abdo et al. 2009, 2010d, 2010a).

The discovery of GeV gamma-rays from magnetars would have major implications, hence would require very strong evidence. The evidence so far does not seem to reach more than the circumstantial level, and while the *Fermi*-LAT exposure continues to accumulate on these sources, we find it appropriate for the time being to report only upper limits.

The upper limits are evaluated by applying the binned likelihood analysis, and using the spectral-spatial models described above. We derived 95% flux upper limits by fitting a point source at the X-ray magnetar position, for which we increase the flux until the maximum likelihood decreases by 2.71/2 in logarithm.

In the 0.1–10 GeV energy range we fix the photon index value of the magnetars to 2.5, which is the mean of the photon indexes obtained by the previous likelihood analyses. The other two upper limits are evaluated using spectral index values that mimic a cutoff in the spectrum at ~ 1 GeV, as common in pulsar spectra. Accordingly, in the range 0.1–1 GeV we fix the spectral index to 1.5, while for 1–10 GeV it is set as 3.5.

The uncertainties of the *Fermi*-LAT effective area and of the Galactic diffuse emission are the two main sources of systematics that can affect the evaluation of the upper limits. We estimated the effect of these systematics by repeating the upper limits analysis using modified instrument response functions that bracket the "Pass 6 v3 Diffuse" effective areas, and changing the normalization of the Galactic diffuse model artificially by ±6%. The results of this analysis are reported in Table 4.2.

4.3.5 Timing analysis

A timing analysis was performed for each of the 13 magnetars studied in this work. With this aim we used the X-ray data available for these objects to build their ephemerides to fold the *Fermi*-LAT data, or we searched around their X-ray periods when a long-baseline ephemeris could not be derived. In particular, using *R*XTE and *Swift*-XRT data, ephemerides[3] have been derived for 4U 0142+614, 1E 2259+586, 1E 1048.1−5937, 1RXS J1708 −4009, 1E 1841−045, 1E 1547−5408, and SGR 0501+4516 (Dib et al. in prep; Israel et al. 2010; Bernardini et al. in prep; Rea et al. 2009; Rea et al. in prep.). For each of the other magnetars, an ephemeris valid throughout the 17 months of *Fermi*-LAT observations is not derivable either given the paucity of X-ray observations or because the source is too dim to have long-term measurements of its spin period. For these we searched directly in the gamma-ray data, performing a semi-blind search around plausible values of spin period and its derivative (see Mereghetti 2008). With the help of PRESTO software (Ransom 2001), we also tried to improve the signal including trials

[3]Only in a few cases a single ephemeris could be derived over the entire time-baseline, while in other cases 4-5 different ephemerides were needed to cover the whole *Fermi*-LAT data span.

for the second derivative of the period. No significant signal has been detected either searching in *Fermi*-LAT data around the X-ray period, or, when possible, folding at the X-ray ephemeris derived from current X-ray monitoring observations.

4.3.6 Results and Discussion

In this work we searched for GeV emission from magnetars using the most sensitive data to date. We did not find evidence beyond reasonable doubt that would allow us to claim the detection of any of these magnetars. In a few cases, putative detections were marked for further studies, but they are not significant enough to claim a new population of gamma-ray emitters.

For all of the studied magnetars we calculated the deepest upper limits derived to date in the 0.1–10 GeV energy range. In Figure 4.3 we show the 0.1 keV–10 GeV multi-band spectrum of 4U 0142+614, the persistent magnetar having the brightest emission and steepest spectral decomposition in the hard X-ray band. Comparing the *Fermi*-LAT upper limits to the hard X-ray measured fluxes for all the studied magnetars, it is clear that the spectral energy distribution of these objects should necessarily have a cut-off below the MeV band, as already pointed out for a few sources by *COMPTEL* observations (den Hartog et al. 2006; Kuiper et al. 2006).

In particular, fitting a log-parabolic functions to the hard X-ray spectrum of 4U 0142+614 (Kuiper et al. 2006; Rea et al. 2007b; den Hartog et al. 2008) as an example resulted in a peak energy of 279^{+65}_{-41} keV (den Hartog et al. 2008). This kind of spectral model has been successfully applied to many pulsars such as the Crab or Vela (Kuiper et al. 2001; Massaro et al. 2006a,b; Rea et al. 2007b). Such log-parabolic spectra can be approximately obtained when relativistic electrons are accelerated by some mechanism and competitively cool via synchrotron or by inverse Compton scattering losses. The narrow energy range of each log-parabolic component might then reflect a tight balance between cooling and acceleration in a relatively confined emission locale.

On the other hand, in some cases the hard X-ray tail at > 10 keV can be equally well-modeled with a flat power-law with an exponential cutoff (e.g., den Hartog et al. 2007, 2008) as opposed to a log-parabolic form. One possibility suggested by this is that resonant inverse Compton scattering by a population of highly relativistic electrons energized at altitudes below around ten stellar radii may provide this hard X-ray component of magnetars (see Thompson & Beloborodov 2005; Baring & Harding 2007; Nobili, Turolla & Zane 2008), probably using seed thermal photons emanating from the stellar surface. In this scenario, the *Fermi*-LAT and *COMPTEL* spectroscopic constraints, implying a turnover around $200 - 500$ keV, profoundly limit a combination of the Lorentz factor of the radiating electrons and the typical viewing angle of the observer (Baring & Harding 2007). Accordingly, phase-resolved spectroscopy will provide important diagnostics on more refined models of such a scenario (see e.g., den Hartog et al. 2008). Note that Trümper et al. (2010) recently invoked a bulk-Comptonization, fallback disk model as an alternative, non-magnetar explanation for these tails.

The low *Fermi*-LAT upper bounds provide interesting constraints on postulated magnetar synchrotron/curvature emission from high altitudes. The emerging paradigm for young pulsars that are bright in the 100 MeV – 10 GeV energy range (Abdo et al. 2010c) is that they emit due to acceleration in a slot-gap or outer-gap potential not far from

their light cylinders. Much earlier, Cheng & Zhang (2001) and Zhang & Cheng (2002) proposed an outer-gap model for magnetar emission above 30 MeV, mediated by pairs created at high altitudes in collisions between X-rays originating on or near the surface, and GeV-band primary photons from electrons accelerated in the gap. Given the nominal *Fermi*-LAT sensitivity, their model predicted that SGR 1900+14 and five AXPs (see Fig. 5 of Cheng & Zhang 2001) would have been observable within a year with fluxes of the order of $10^{-7} - 10^{-9}$ photons cm^{-2} s^{-1}, depending on the assumed parameters. However, *Fermi*-LAT does not detect any of these magnetars in 17 months of data. This strong observational diagnostic necessarily forces a revision of the parameter space applicable for the viability of their outer gap model to each magnetar. Repeating the analysis described above for a larger data set of 3.5 years did not yield to a detection of a magnetar in the GeV regime neither.

Recently, [Wu 13] claimed a possible pulsed γ-ray emission above 200 MeV from the magnetar 1E 2259+586 using 3.5 years of LAT-data. This detection is doubtful since the pulse profile has 3 peaks, which are not consistent with the X-ray pulse profile. Furthermore, the pulse did not show up in some epochs. This could be due to a possible glitch and has to be checked with a careful analysis of available X-ray data. Furthermore, this pulsed signal was not found within the Fermi collaboration using a similar data set. Meanwhile, the SNR CTB 109 surrounding the magnetar 1E 2259+586 could be detected with the *Fermi*-LAT [Castro 12]. Due to spatial considerations the authors exclude the association with 1E 2259+586.

Chapter 5

PART III: Prospects

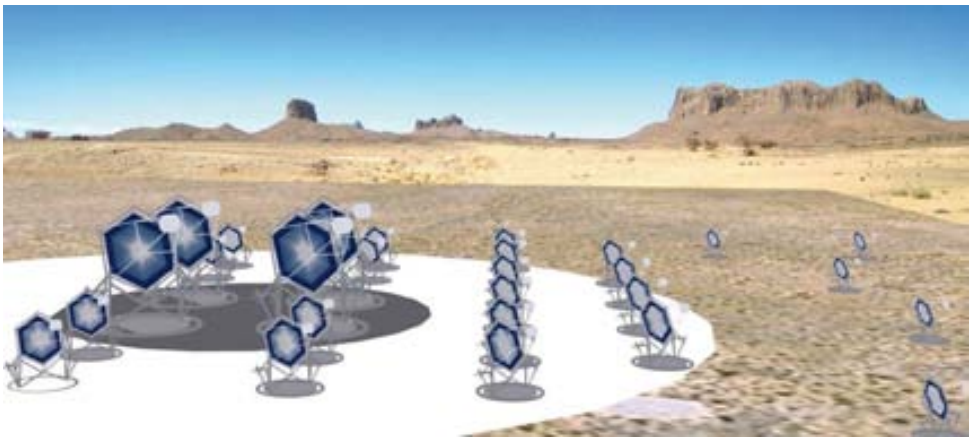

Figure 5.1 Artistic view of the future Cherenkov telescope array. Figure taken from [Actis 11]

5.1 Description of CTA

The Cherenkov telescope array (CTA) will be the successor of the current generation of Imaging Cherenkov telescopes (IACTs) introduced in Chapter 2. It is planned to run it as an open observatory to study gamma rays in the wide energy range from 10s of GeV to 100s of TeV with an unprecedented flux sensitivity as well as angular and energy resolutions. In 2010 the CTA Consortium completed a Design Study and started a three-year Preparatory Phase which leads to production readiness of CTA in 2014 [Actis 11]. The main aims of this new project (as described in the Design Study) are:

- increase sensitivity of current instruments by another order of magnitude for deep observations around 1 TeV
- boost significantly the detection area and hence detection rates, particularly important for transient phenomena and at the highest energies,
- increase the angular resolution and hence the ability to resolve the morphology of extended sources,

- provide uniform energy coverage for photons from some tens of GeV to beyond 100 TeV,
- enhance the sky survey capability, monitoring capability and flexibility of operation.

It is planned to built two arrays for full sky coverage: one in the Northern and one in the Southern hemisphere.. The Northern one will be mainly focused on Active Galactic Nuclei (AGN) physics, EBL studies, study of nearby Galaxy clusters and intensive studies of the Crab nebula with its pulsar. The Southern array will focus more on sources in the Galactic plane to study their morphological features and to detect a lot of more sources for population studies. It has still to be decided where exactly these observatories will be built and which layout of the telescope array will be realized at the end. Several studies and simulations were done and are still undergoing. Some of them are presented here.

To investigate which array fulfills best the scientifical and economical requirements, a 275 telescope configuration has been simulated. It consists of different kinds of telescopes: Small size telescopes of 5-8 m diameter (SST); Medium size telescopes of 10-12 m diameter (MST); and Large size telescopes of 20-30 m diameter (LST). 11 subsets of this huge configuration are candidates for the future CTA array and are investigated in the following.

The different subsets were characterized based on their differential sensitivity, energy and angular resolutions. For the differetial sensitivity a significant detection (above 5% of the background level, with $\geq 5\sigma$ statistical significance and at least 10 events) is required in each energy bin, whereas there is a convention to use 5 bins per decade in energy. We grouped the array candidates according to their differential sensitivity: one group with good response at low energies, one at high energies and one with a good response along the whole energy range. The purpose was to work in the following only with one representative configuration of each group to make the analysis of different sources easier. These three representatives are the setups B (low energies), *D* (high energies) and *I* (whole energy range) shown in Figure 5.2. They show the best differential sensitivity within their corresponding group and are also good representatives comparing angular and energy resolution within their group. Their characteristics are shown in Figure 5.3 and can be explained by looking at the different setups in Figure 5.2:

- Configuration *B* consists of 5 LSTs in the center, which makes the setup very sensitive to low energies, surrounded by a closely spaced MST array. It provides superior hadron rejection and angular resolution at low energies due to the compact design. The array does not cover a big area by lacking SSTs. Therefore, it provides a more modest effective collection area at energies >1 TeV and looses sensitivity there.
- Configuration *D* covers a large area and is therefore sensitive at high energies. Since it lacks LSTs this setup has very little sensitivity below 100 GeV and looses angular resolution already below 1 TeV.
- Configuration *I* is the compromise array, which attempts to do well in the broad energy range using all three telescope types and multiple spacings. Such an array comes closest to achieving the CTA performance goals and sensitivity, which is

shown as the black line in the bottom plot of Figure 5.3. If the budget constraints allow, the configuration *I* could constitute, therefore, a possible CTA array.

The simulations and studies in the following chapter were done using the compromise array *I*.

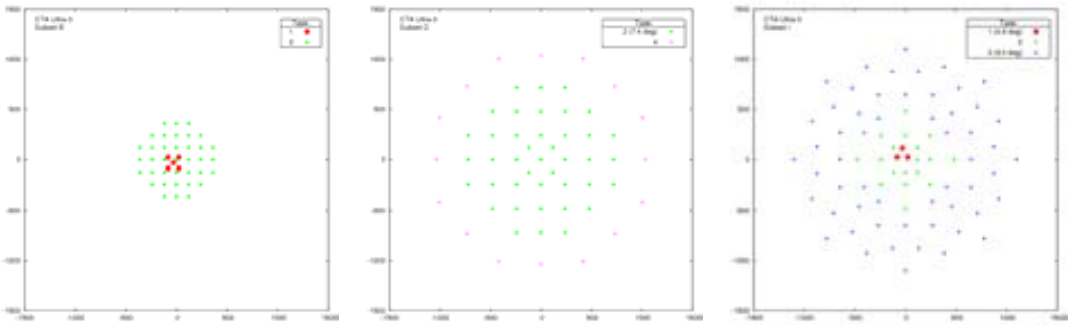

Figure 5.2 Three example candidate configurations (B, D & I) which are subsets of the 275 telescope array. *Red:* Large size telescopes, *Green and Pink:* Medium size telescopes, *Blue:* Small size telescopes. Figures taken from [Bernlöhr 10].

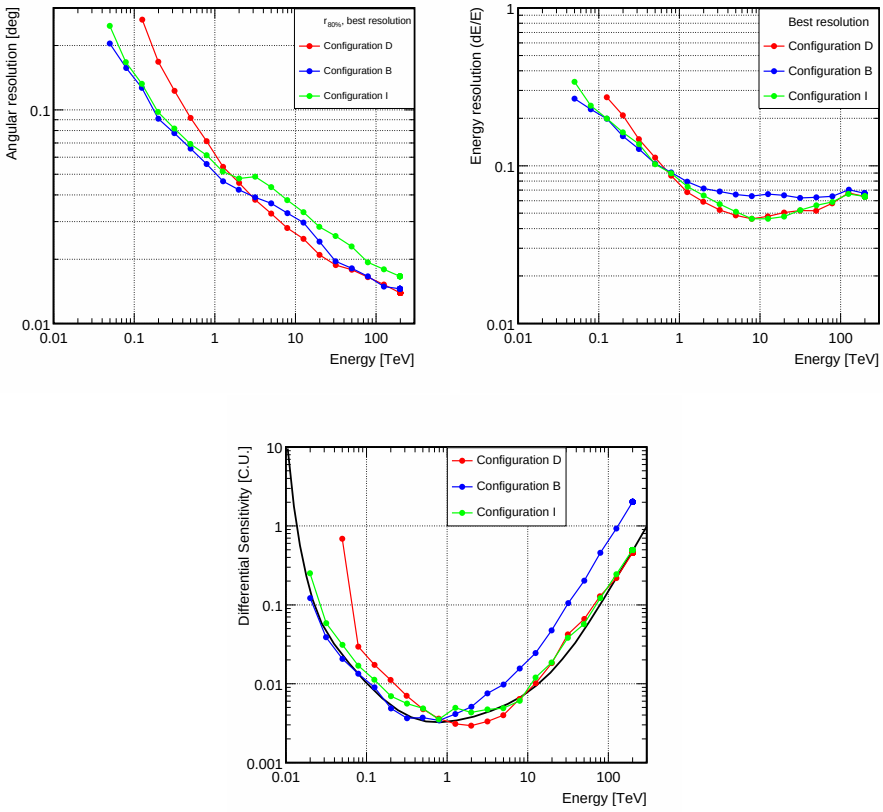

Figure 5.3 *Top:* Angular and energy resolution. *Bottom:* Differential sensitivity curves for the three represantatives of each group. *Black:* aimed sensitivity.

5.2 Motivation

> We evaluate the potentialities of the Cherenkov telescope array (CTA) to study the non-thermal physics of gamma-ray binaries, which requires the observation of high-energy phenomena at different time and spatial scales. We analyze the capability of CTA to probe the spectral, temporal and spatial behavior of gamma-ray binaries in the context of the known or expected physics of these sources. CTA will be able to probe with high spectral, temporal and spatial resolution the physical processes behind the gamma-ray emission in binaries, significantly increasing as well the number of known sources. This will allow the derivation of information on the particle acceleration and emission sites qualitatively better than what is currently available. The work on the following chapters is based on [Paredes 13].

It is expected that CTA will find new gamma-ray binaries, allowing population studies that will have an impact on evolutionary models of high-mass binary systems. With a few exceptions, most of the gamma-ray binaries detected, either accreting or non-accreting sources, are all within 3 kpc of the Sun, in a volume equal to about $\sim 10\%$ of the volume of our Galaxy. Assuming a uniform distribution, although they should follow population I stars with more objects in the spiral arms, this is consistent with > 50 or so gamma-ray binaries in our Galaxy. This number is also dependent on the duty cycle of gamma-ray emission: VHE emission in HESS J0632+057, LS I +61 303, PSR B1259−63 is strongly dependent on orbital phase and in some sources the orbital periods can be (very) long. With a ten times improvement in sensitivity, CTA should be able to probe for gamma-ray binaries of comparable luminosities up to the Galactic center. CTA can thus be reasonably expected to detect a couple of dozen gamma-ray binaries. The VHE counterparts of LS 5039, HESS J0632+057 and (possibly) 1FGL 1018.6−5856 were discovered in the H.E.S.S. Galactic Plane survey. The ten times more sensitive Galactic Plane survey planned for CTA should thus enable many discoveries of such systems, which are otherwise very difficult to uncover by X-ray, optical or radio surveys. A survey of the central portion of the galactic plane is planned for the beginning of CTA operation (see [**?**]), which will pinpoint new gamma-ray binaries candidates.

The study of known and/or new compact binary systems at VHE is of primary importance because their complexity allows us to probe several physical processes that are still poorly understood. Some of these systems are extremely efficient accelerators that could shed new light, and eventually force a revision of, particle acceleration theory (see e.g. [**?**]). The particle injection and radiation emission mechanisms in binary systems vary periodically due to an eccentric orbit and/or interaction geometry changes. This may provide information on the location of the high energy particles, on the energy mechanism(s) powering relativistic outflows, on the nature of the accelerated particles, and on the physical conditions of the surrounding environment. The presence of strong photon fields allows the study of photon-photon absorption and electromagnetic cascades. All these processes occur on timescales $\lesssim 1000$ s, a proper study of which would require at least a 5σ (standard deviations) detection for $\sim$ one hour exposure times.

The interaction of binary systems with the Interstellar medium (ISM) could also be powering a new class of TeV sources, which could be resolved/detected with enough resolution/sensitivity. For a deep study of the processes taking place in compact binary systems we need to go beyond the present IACT's capabilities. Below, we report on examples of numerical simulations performed to show how the forthcoming CTA observatory [Actis 11] could fulfill these objectives.

The structure is as follows: First, we portray shortly the source class of colliding wind binaries, which was not introduced yet. In Section 5.2.1 we study the CTA flux error reduction at the example of LS 5039 . Afterwards, in Section 5.2.2, we explore the shortest time scales in which CTA can resolve a flare. The sensitivity to spectral shape variations is studied in Section 5.2.3. Finally, before the summary, we present the simulations of the energy spectrum of Eta Carinae in Section 5.2.4.

Colliding wind binaries

Hot stars can generate strong winds and form colliding wind binary systems (CWB). Shocks are expected to form in massive star binaries, in the region where the winds from both stars collide. Non-thermal synchrotron emission from the colliding wind region in one source has been detected [**?**], which indicates the presence of highly relativistic electrons (see also [**?**]). These systems may also be embedded in dense photon fields where IC losses would be unavoidable, making CWBs potential high-energy emitters [**?** **?**].

An extreme example is the Eta Carinae system [**?**]. Gamma-ray emission has been theoretically predicted from this source (see e.g. [**?** **?**]) and the emission has been tentatively confirmed recently by the *Fermi*/LAT [**?** **?**] and *AGILE* [**?**] instruments. The predominant GeV emission of Eta Carinae, shown in the top panel of Fig. 5.4, seems to agree with what is expected from IC and/or neutral pion decay processes in such type of system. At VHE, Eta Carinae has not been detected so far [**?**]. The reported HE flux levels and the spectrum make however this source a good target for CTA, since it will provide a significantly improved sensitivity at energies in the range 30 to 100 GeV as compared to present IACTs. MAGIC observations of WR 146 and WR 147 produced the first bounds on the high-energy emission from Wolf-Rayet binary systems [**?**].

VHE emission is theoretically expected from binary systems with high-mass loss and high-velocity winds. These systems display some of the strongest sustained winds among Galactic objects and have the highest known mass-loss rate of any stellar type. Colliding winds of massive star binary systems are potential VHE gamma-ray emitters, via leptonic and/or hadronic processes after acceleration of primary particles in the collision shocks.

The detection of VHE emission from colliding winds requires an improved sensitivity with respect to current IACTs. To further study these systems in case of detection, phase-resolved light curves and spectra would be required. Such spectra could give us a clue to understanding the physical processes behind the emission, since the non-thermal particle distribution strongly depends on the shock conditions at each orbital phase. A low-energy array is favoured; a cutoff at a level of $\sim$100 GeV due to the modest shock velocity and finite size of the acceleration zone is predicted, and CTA should be able to operate at a lower energy threshold than present IACTs. Finally, the orbital distances between the two stars ($\sim 10^{13} - 10^{15}$ cm) make the emission region too small to be resolved out by the current designs of CTA configurations. Angular resolution is therefore not a requirement in this case.

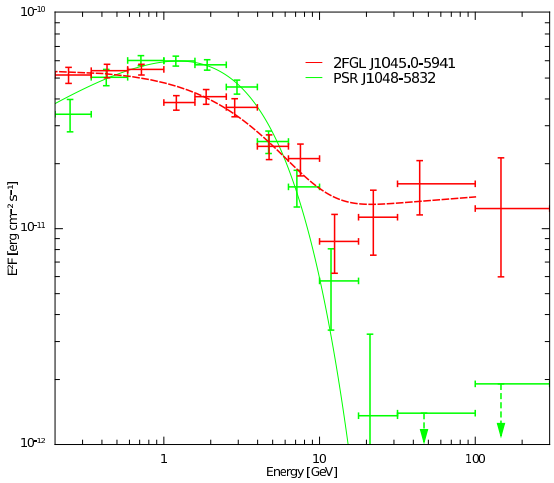

Figure 5.4 Spectral energy distributions (SED) of two *Fermi*/LAT sources at the position of Eta Carinae: 2FGL J1045.0−5941 (red points) and PSR J1048−5832 (green points). The best-fit model for the average spectrum is shown as a red dashed line ([**?**]).

5.2.1 CTA flux error reduction in known TeV sources

Accurate estimates of the flux, spectral shape, and evolution of known TeV sources are very important for constraining the physical parameters of the high-energy emitting region. This is even more needed when there are several parameters that have to be left free when fitting data. To explore the CTA capability to derive observables and constrain theoretical models, we simulated the CTA response on LS 5039. This source might not be representative of the class of binaries, but will allow us to compare the improvement from CTA data on the present generation of IACTs. We based our simulations on the results obtained by H.E.S.S. on the source, simulating the CTA response under similar conditions (above 1 TeV). Since the H.E.S.S. data were taken over a long time span and under different zenith angles, the energy threshold was not constant. To make a fair comparison with the H.E.S.S. analysis, we treated our simulated data the same way as the H.E.S.S. collaboration did [**?**]. The simulated counts and the flux normalization were extracted above 1 TeV assuming an average photon index derived from all data: $\Gamma = 2.23$ for $\mathrm{d}N/\mathrm{d}E \sim E^{-\Gamma}$. Based on the H.E.S.S. results we assumed a sinusoidal shape of the light curve with a period of 3.9 d. For each phase point, and using configuration `I`, we then evaluated the light curve and simulated spectra of the form described above as seen by CTA, for a certain observation time in each phasogram bin. By integrating these spectra, we got the flux above 100 GeV in each bin. We then extrapolated the obtained flux value to the integral flux above 1 TeV and propagated the error correspondingly. The result for 70 hours of exposure time of CTA is shown in Figure 5.5. The improvement of observations by CTA is clearly visible. The error bars are reduced by a factor of ∼2–4 with respect to the H.E.S.S. data points, assuming the average photon index of Γ =2.23. This can be taken as a direct comparison to the published H.E.S.S. results. However, the spectral index of the LS 5039 VHE emission changes as a function of orbital phase. A variation of the spectral index affects the error estimate. Softening the assumed photon index (Γ ∼3), CTA data would improve the errors by up to a factor of 7, whereas a harder spectrum (Γ ∼2) results in a minor error reduction of less than a factor of 2. We have also performed similar simulations but taking a time binning of 10, 20, 50 and 100 bins per full phase period and using a

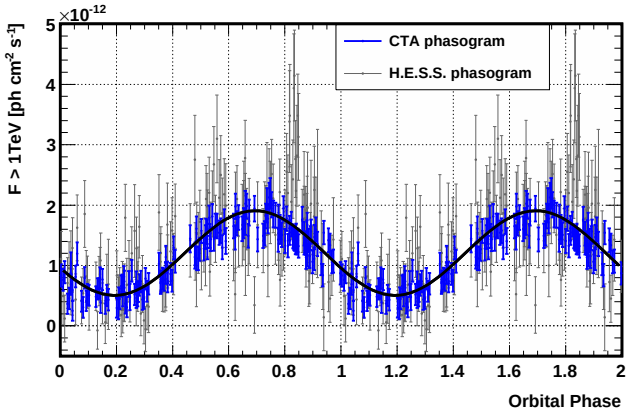

Figure 5.5 CTA simulations of LS 5039. Phasograms of H.E.S.S. (gray) and simulated CTA observations (blue). With CTA observations the error on the flux can be reduced by a factor 2 – 4 above 1 TeV.

binning of 14 and 28 minutes. The resulting plots are shown in Figure 5.6. With 10 bins per full orbital period the sinusoidal shape can hardly be seen, whereas with 20 bins a sine function can be fitted to the data points. Taking 50 bins of 28 minutes even substructures can be resolved. To obtain the same results and similar error bars like those reported by H.E.S.S., CTA would only need ∼1/6th of its observation time, that is, 50 bins of 14 min each, pointing towards the possibility of performing a long-term monitoring of the global behavior of the source, and accessing the duty cycle of the observed features, if any.

Furthermore we studied the minimum observation time for CTA to detect the period of LS 5039 in comparison with the H.E.S.S. one. To do so, we simulated CTA observations using a sine function over time that reproduces the time structure of the H.E.S.S. flux points. From the simulated CTA observations we derived flux points for each time bin and used those to construct the power spectrum of LS 5039. Whereas H.E.S.S. used 160 bins of 28 minutes (∼70 hours in total) to detect the 3.9 days period of the system, CTA could detect the period with more than 5 σ with only 160 bins of 3 min (8 hours in total). This would be a significant reduction of observation time for CTA. It has to be kept in mind that the significance of the period estimation in the H.E.S.S. data is larger than 5 σ (i.e. 8 σ), as all the data available at the time were used.

We studied the modulation of the photon index and the flux normalisation with the orbital period for a source like LS 5039. To compare with the H.E.S.S. measurements, we assumed 7 hours of observation time for each phase bin and simulated the CTA spectra for each phase bin with the spectral parameters obtained by H.E.S.S. (photon index and differential flux at 1 TeV). By fitting these simulated spectra, we obtained the fit parameters with the corresponding error. The results are shown in Figure 5.7. The direct comparison of the errors of the H.E.S.S. and CTA measurements shows that observations with CTA can reduce the errors on the spectral parameters by a factor between 2 and 4.5.

The larger sensitivity of CTA would allow tracking the behavior of a source in shorter timescales. In particular, it would allow comparing with predictions of the spectral evolution of a source such as LS 5039, even at the minimum of its TeV flux. As an example,

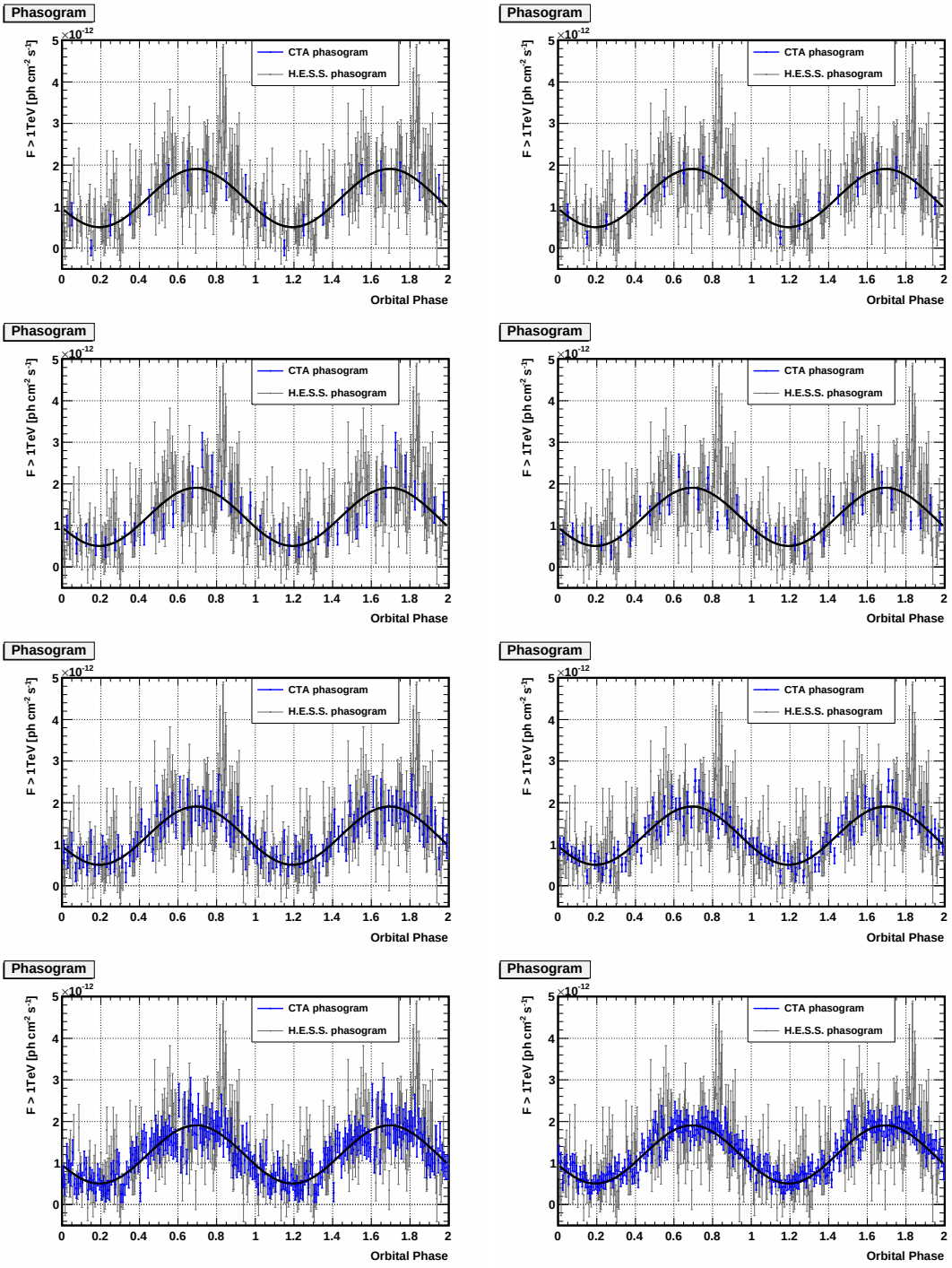

Figure 5.6 Folded simulated lightcurves detected by CTA (blue) plotted over the lightcurve obtained by H.E.S.S. (gray). From top to bottom panel the simulated bins increase from 10, 20, 50 to 100 bins per phase period. In the left column the CTA simulated data points represent 14 minutes, in the right column the points represent 28 minutes of observation time.

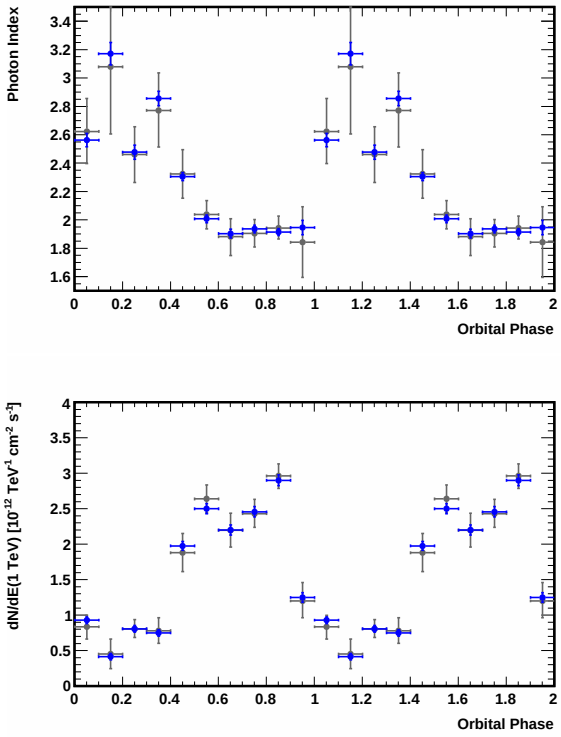

Figure 5.7 CTA simulations of LS 5039. *Top:* Photon index versus phase (CTA blue, H.E.S.S. gray). *Bottom:* Flux normalisation versus phase (CTA blue, H.E.S.S. gray).

we used the spectra in phases 0.2 and 0.3 as derived by [**?**], where electromagnetic cascades were included. In Figure 5.8 we show the results of our simulations: in the top panel, the two simulated spectra are plotted, assuming an observation time of 5 hours. Since the reconstruction of the energy spectra in true energy requires a complicated unfolding procedure we conservatively choose to compare the two spectra on the level of the excess events as a function of reconstructed energy. The two corresponding distributions are shown in the middle panel of Figure 5.8. The distributions are compared to each other by calculating the residuals between the two, which is shown in the bottom panel. The probability of these spectra to be consistent (i.e. to originate from the same original distribution) is $\ll$1%. We conclude that CTA would easily distinguish between spectra at different phase bins.

5.2.2 Short timescale flux variability

To further explore the shortest time scales in which CTA can resolve a flare, we simulated a 20 hours event whose flux variation follows a Gaussian distribution and assuming the best-fit spectral shape reported by MAGIC for the Cygnus X-1 signal [**?**]:

$$\frac{\mathrm{d}N}{\mathrm{d}A\mathrm{d}t\mathrm{d}E} = (2.3 \pm 0.6) \times 10^{-12} \frac{E}{1\,\mathrm{TeV}}^{-3.2\pm0.6} \mathrm{cm}^{-2}\mathrm{s}^{-1}\mathrm{TeV}^{-1} \tag{5.1}$$

20 hours represent the total duration of the flare (i.e. the mean of the Gaussian distribution is at 10 hours from the start of the observation). With a binning of 5 min for each data point, CTA could clearly resolve this assumed Gaussian-shaped flare (see

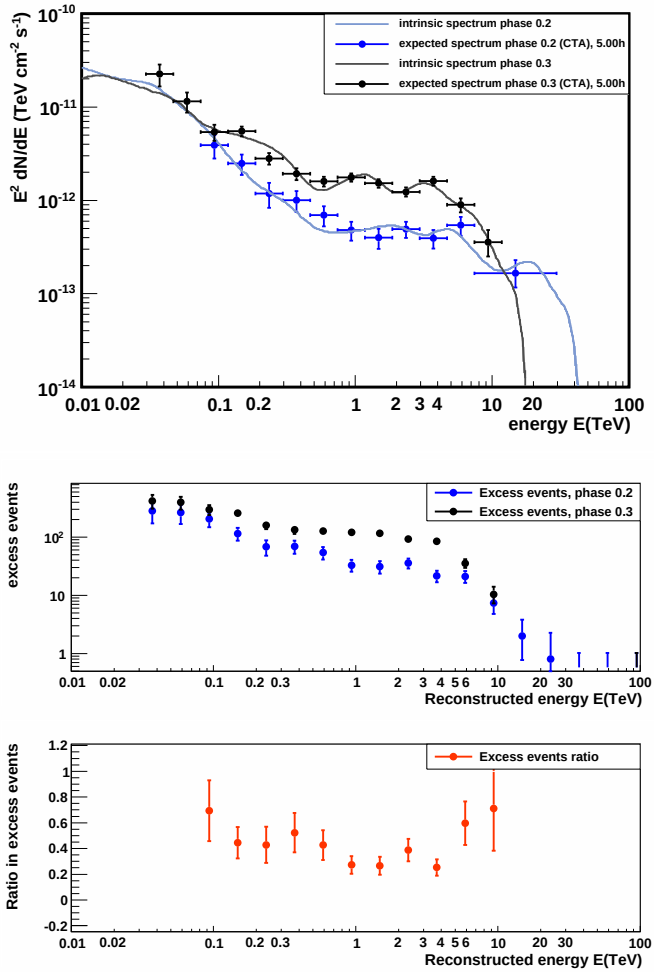

Figure 5.8 CTA simulations of LS 5039. *Top:* Intrinsic (line) and simulated (data points) energy spectra for phases 0.2 (blue) and 0.3 (black). The assumed integration time is 5 h. *Middle:* Excess events obtained from the simulations above versus reconstructed energy. *Bottom:* Residuals of the excess events distributions from the two distributions above. In all three panels a very clear difference between the two spectra can be seen.

Figure 5.9). A 5 min integration would result in a detection with a significance of 7σ at the assumed low state and 25σ in high state, whereas with the sensitivity of MAGIC it is only possible to detect the peak of this flare. This is a clear example of the better sensitivity of CTA with respect to the existing IACTs. Although the limited duty cycle of Cherenkov telescopes prevents them to observe a source for 20 hours in a row, a realistic exposure time of 5 hours would be enough for CTA to resolve parts of the flare in bins of $\sim$10 min.

As a conclusion from this simulation exercise, we see that the full CTA array will be a powerful tool to probe into the fast flux variability of gamma-ray binaries, which could allow the characterization of the dynamical processes taking place in the emitting plasma.

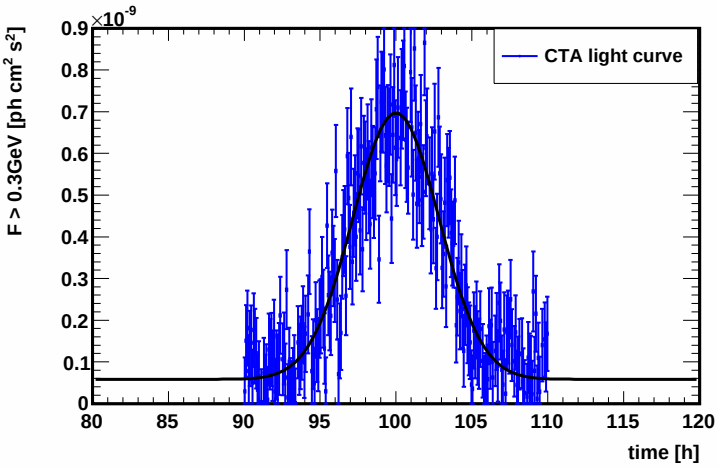

Figure 5.9 Simulated Gaussian shaped flare for Cygnus X-1. The simulated data points in blue correspond to a time binning of 5 min.

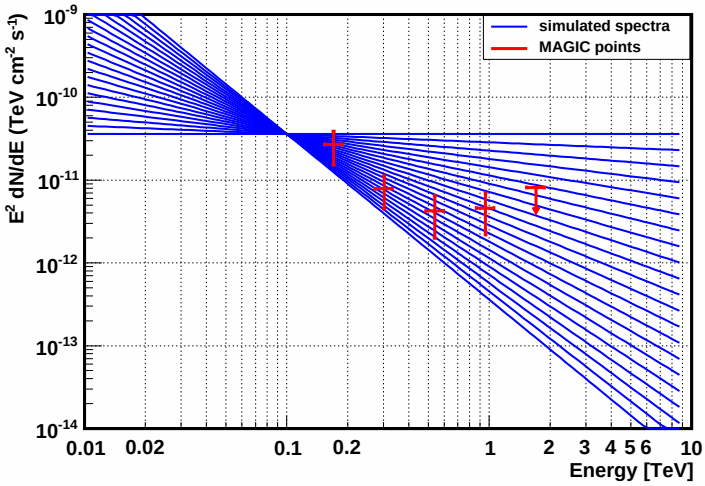

Figure 5.10 In blue the intrinsic spectra used for the simulations together with the data points of MAGIC for the source Cygnus X-1 are shown.

5.2.3 Sensitivity to spectral shape variations

To further test the CTA spectral capabilities, we have used the derived spectrum of Cygnus X-1 during the flare to simulate 20 energy spectra with photon indices ranging from -2 to -4 (see Figure **??**). We have also simulated different exposure times: 5, 15, 30 and 60 min, to study the minimum time scale to distinguish between the slope of different spectra. Figure **??** left shows the photon index error versus the simulated photon index in the fitting of the resulting CTA spectra. CTA would be able to distinguish the different spectral slopes in all cases except those showing the softest spectra, where the error bars are too large to properly distinguish them at a high confidence level. In that case, the observation of a flare as that reported in Cygnus X-1 would require exposures ≥ 15 min. Should such a kind of flare happen again, the minimum timescale for a 5 standard

deviations detection of a flare within 10% of the reported spectrum from Cygnus X-1 is in the range of 2–3 min. However, in order to have a spectrum determination, one can consider a 10σ detection threshold. With this constraint, the minimum timescale accessible is in the range of 8.5–12.5 min. This is shown in Fig **??** right. The above estimates hold, provided that the responses of the array are as stable as simulated for 30 minutes exposure and that the timescales are probed a priori.

It is clear that CTA will be a powerful tool for the detection of spectral variations in gamma-ray binaries. The statistical errors we obtained for these simulations are nearly an order of magnitude lower than the ones obtained with MAGIC in 2007, thus demonstrating the capability of CTA to deliver new and exciting science in the following years.

5.2.4 Exploring the colliding winds of massive star binary systems

We performed numerical simulations of the response of CTA for a CWB like Eta Carinae. We based our simulations on the measurements of the energy spectrum of Eta Carinae (see top panel of Fig. 5.4) by the *Fermi*/LAT [**?**] and the upper limits derived by the H.E.S.S. Collaboration [**?**]. The spectrum between 0.1 and 100 GeV is best fit by a power law with an exponential cutoff plus an additional power law at high energies. In the TeV range, Eta Carinae has not been detected. In Figure 5.11 (left) we show the Fermi/LAT data points and the H.E.S.S. upper limits in gray. From these measurements, it seems that there must be a cutoff in the spectrum at high energies. For our simulations we assume exponential cutoffs at $E = 100, 150, 200$ GeV and test how well CTA could detect those. We produced simulations at increasing observation times in order to study the minimal time required to detect the source and to get a meaningful spectra with such CTA observations. In Figure 5.11 (left), we show the simulated energy spectra with different cutoffs as they would be measured by CTA. Simulations for 10 hours of observation time are displayed. To detect Eta Carinae, CTA would need 2–10 hours of observations, depending on the energy cutoff in the spectrum; together with Fermi/LAT data, it should be possible to determine the cutoff energy using a combined fit. However, it would take a longer time to determine the cutoff energy using CTA data alone. The minimum observation time needed to significantly determine the cutoff energy, i.e. to distinguish between a simple power law and a cutoff power law, is established using the likelihood ratio test for the two hypothesis. In Figure 5.11 (right), we show the resulting significance that a cutoff power law is a better fit to the data than a pure power law versus integration time for the different energies of the cutoff. For this study we simulated 100 spectra for each cutoff energy and for different observation times as shown in the plot. Taking 3σ as a limit to distinguish between the two different spectral hypothesis, one can see that 20 hours are enough to detect the cutoff only if it is above 150 GeV. For a cutoff $\leq$150 GeV, 30 to 50 hours are needed. From our simulations, we can conclude that CTA observation times of $>$15 hours are necessary to make meaningful physics interpretation and modeling, whereas $>$20 hours are necessary to precisely measure the energy cutoff in the spectrum. A proper characterization of the highest energy cutoff will give important clues on the acceleration efficiency of the source, which may be operating close to the limit predicted by diffusive shock acceleration, and on the nature of the radiation mechanism, either leptonic (IC) or hadronic (proton-proton interactions). It is noteworthy that other colliding wind binary systems hosting powerful WR and O stars may be also powerful non-thermal emitters, as hinted by hard X-ray observations or WR 140 with Suzaku [**?**].

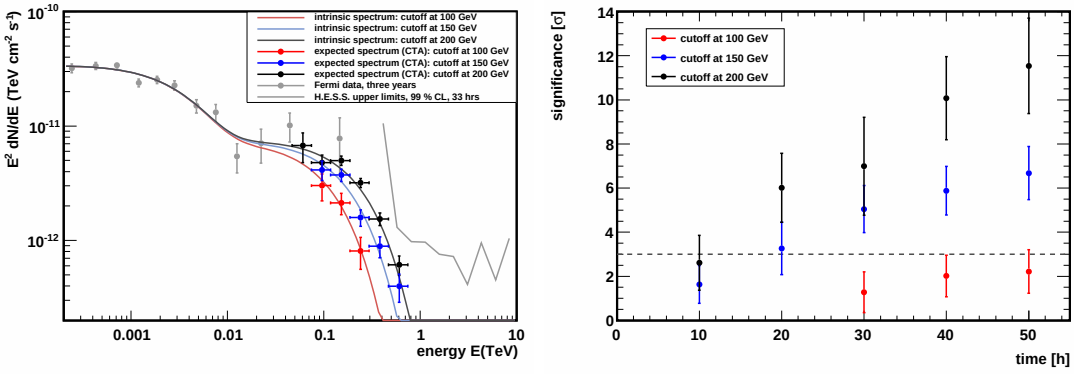

Figure 5.11 CTA simulations of Eta Carinae. *Left:* Intrinsic and CTA simulated spectra after 10 hours of observation time with high energy cutoffs at 100, 150 and 200 GeV. *Right:* Significance at which the corresponding cutoffs (color coded, see legend) can be resolved (i. e. are a better fit when compared to a simple power law) versus observation time. The dashed line at 3σ is to guide the eye.

5.3 Summary and conclusion

The sensitivity of CTA will lead to a very good sampling of light curves and spectra on very short timescales. It will allow as well long source monitoring using subarrays, still with a sensitivity 2–3 times better than any previous instrument operating at VHE energies. In particular, it is noteworthy that CTA will reduce by a factor of a few the errors in the determination of fluxes and spectral indexes. The high sensitivity and good angular resolution will allow also for imaging of possible extended emission in gamma-ray binaries, expected at the termination of the generated outflows. The low energy threshold will also permit to study the maximum particle energy achievable in massive star binaries, trace the effects of electromagnetic cascades in the spectra of gamma-ray binaries, or catch the most luminous part of the spectrum in some sources. Finally, under CTA the population of gamma-ray binaries (and their different subclasses) may easily grow by one order of magnitude, which will imply a strong improvement when looking for patterns and trends, tracing the physical mechanisms behind the non-thermal activity in these sources. For all this, CTA, either in highly sensitive observations of the whole array, or under the more suitable for monitoring subarray mode, will be a tool to obtain the required phenomenological information for deep and accurate modeling of gamma-ray binaries. This can mean a qualitative jump in our physical knowledge of high-energy phenomena in the Galaxy.

Bibliography

[Abdo 09] A. A. Abdo, M. Ackermann, M. Ajello & Atwood et al. *Fermi LAT Observations of LS I +61° 303: First Detection of an Orbital Modulation in GeV Gamma Rays.* ApJ, vol. 701, pages L123–L128, August 2009.

[Abdo 10] A. A. Abdo, M. Ackermann, M. Ajello, A. Allafort, L. Baldini, J. Ballet, G. Barbiellini, M. G. Baring, D. Bastieri, R. Bellazzini, R. D. Blandford, E. D. Bloom, E. Bonamente, A. W. Borgland, A. Bouvier, J. Bregeon, M. Brigida, P. Bruel, T. H. Burnett, G. A. Caliandro, R. A. Cameron, P. A. Caraveo, C. Cecchi, Ö. Çelik, S. Chaty, A. Chekhtman, C. C. Cheung, J. Chiang, S. Ciprini, R. Claus, J. Conrad, P. R. den Hartog, C. D. Dermer, A. de Angelis, F. de Palma, R. Dib, M. Dormody, E. d. C. e. Silva, P. S. Drell, R. Dubois, D. Dumora, T. Enoto, C. Favuzzi, M. Frailis, P. Fusco, F. Gargano, N. Gehrels, N. Giglietto, P. Giommi, F. Giordano, M. Giroletti, T. Glanzman, G. Godfrey, I. A. Grenier, M.-H. Grondin, S. Guiriec, D. Hadasch, Y. Hanabata, A. K. Harding, E. Hays, G. L. Israel, G. Jóhannesson, A. S. Johnson, V. M. Kaspi, H. Katagiri, J. Kataoka, J. Knödlseder, M. Kuss, J. Lande, S.-H. Lee, M. Lemoine-Goumard, F. Longo, F. Loparco, M. N. Lovellette, P. Lubrano, A. Makeev, M. Marelli, M. N. Mazziotta, J. E. McEnery, J. Mehault, P. F. Michelson, T. Mizuno, A. A. Moiseev, C. Monte, M. E. Monzani, A. Morselli, I. V. Moskalenko, S. Murgia, M. Naumann-Godo, P. L. Nolan, E. Nuss, T. Ohsugi, A. Okumura, N. Omodei, E. Orlando, J. F. Ormes, M. Ozaki, D. Paneque, D. Parent, M. Pepe, M. Pesce-Rollins, F. Piron, T. A. Porter, S. Rainò, R. Rando, M. Razzano, N. Rea, A. Reimer, O. Reimer, T. Reposeur, S. Ritz, H. F.-W. Sadrozinski, P. M. Saz Parkinson, C. Sgrò, E. J. Siskind, D. A. Smith, G. Spandre, P. Spinelli, M. S. Strickman, H. Takahashi, T. Tanaka, J. B. Thayer, D. J. Thompson, L. Tibaldo, D. F. Torres, G. Tosti, A. Tramacere, E. Troja, Y. Uchiyama, T. L. Usher, J. Vandenbroucke, V. Vasileiou, G. Vianello, V. Vitale, A. P. Waite, B. L. Winer, K. S. Wood, Z. Yang & M. Ziegler. *Search for Gamma-ray Emission from Magnetars with the Fermi Large Area Telescope.* ApJ, vol. 725, pages L73–L78, December 2010.

[Ackermann 13] M. Ackermann, M. Ajello, A. Allafort, L. Baldini, J. Ballet, G. Barbiellini, M. G. Baring, D. Bastieri, K. Bechtol, R. Bellazzini, R. D. Blandford, E. D. Bloom, E. Bonamente, A. W. Borgland, E. Bottacini, T. J. Brandt, J. Bregeon, M. Brigida, P. Bruel, R. Buehler, G. Busetto, S. Buson, G. A. Caliandro, R. A. Cameron, P. A. Caraveo, J. M.

Casandjian, C. Cecchi, Ö. Çelik, E. Charles, S. Chaty, R. C. G. Chaves, A. Chekhtman, C. C. Cheung, J. Chiang, G. Chiaro, A. N. Cillis, S. Ciprini, R. Claus, J. Cohen-Tanugi, L. R. Cominsky, J. Conrad, S. Corbel, S. Cutini, F. D'Ammando, A. de Angelis, F. de Palma, C. D. Dermer, E. do Couto e Silva, P. S. Drell, A. Drlica-Wagner, L. Falletti, C. Favuzzi, E. C. Ferrara, A. Franckowiak, Y. Fukazawa, S. Funk, P. Fusco, F. Gargano, S. Germani, N. Giglietto, P. Giommi, F. Giordano, M. Giroletti, T. Glanzman, G. Godfrey, I. A. Grenier, M.-H. Grondin, J. E. Grove, S. Guiriec, D. Hadasch, Y. Hanabata, A. K. Harding, M. Hayashida, K. Hayashi, E. Hays, J. W. Hewitt, A. B. Hill, R. E. Hughes, M. S. Jackson, T. Jogler, G. Jóhannesson, A. S. Johnson, T. Kamae, J. Kataoka, J. Katsuta, J. Knödlseder, M. Kuss, J. Lande, S. Larsson, L. Latronico, M. Lemoine-Goumard, F. Longo, F. Loparco, M. N. Lovellette, P. Lubrano, G. M. Madejski, F. Massaro, M. Mayer, M. N. Mazziotta, J. E. McEnery, J. Mehault, P. F. Michelson, R. P. Mignani, W. Mitthumsiri, T. Mizuno, A. A. Moiseev, M. E. Monzani, A. Morselli, I. V. Moskalenko, S. Murgia, T. Nakamori, R. Nemmen, E. Nuss, M. Ohno, T. Ohsugi, N. Omodei, M. Orienti, E. Orlando, J. F. Ormes, D. Paneque, J. S. Perkins, M. Pesce-Rollins, F. Piron, G. Pivato, S. Rainò, R. Rando, M. Razzano, S. Razzaque, A. Reimer, O. Reimer, S. Ritz, C. Romoli, M. Sánchez-Conde, A. Schulz, C. Sgrò, P. E. Simeon, E. J. Siskind, D. A. Smith, G. Spandre, P. Spinelli, F. W. Stecker, A. W. Strong, D. J. Suson, H. Tajima, H. Takahashi, T. Takahashi, T. Tanaka, J. G. Thayer, J. B. Thayer, D. J. Thompson, S. E. Thorsett, L. Tibaldo, O. Tibolla, M. Tinivella, E. Troja, Y. Uchiyama, T. L. Usher, J. Vandenbroucke, V. Vasileiou, G. Vianello, V. Vitale, A. P. Waite, M. Werner, B. L. Winer, K. S. Wood, M. Wood, R. Yamazaki, Z. Yang & S. Zimmer. *Detection of the Characteristic Pion-Decay Signature in Supernova Remnants.* Science, vol. 339, pages 807–811, February 2013.

[Actis 11] M. Actis, G. Agnetta, F. Aharonian, A. Akhperjanian, J. Aleksić, E. Aliu, D. Allan, I. Allekotte, F. Antico, L. A. Antonelli & et al. *Design concepts for the Cherenkov Telescope Array CTA: an advanced facility for ground-based high-energy gamma-ray astronomy.* Experimental Astronomy, vol. 32, pages 193–316, December 2011.

[Aharonian 81] F. A. Aharonian & A. M. Atoyan. *Cosmic gamma-rays associated with annihilation of relativistic e^+-e^- pairs.* Physics Letters B, vol. 99, pages 301–304, 1981.

[Aharonian 04] F. A. Aharonian. Very high energy cosmic gamma radiation. World Scientific, 2004.

[Aharonian 06] F. et al. Aharonian. *HESS Observations of the Galactic Center Region and Their Possible Dark Matter Interpretation.* Physical Review Letters, vol. 97, no. 22, pages 221102–+, December 2006.

[Albert 08] J. Albert, E. Aliu, H. Anderhub, P. Antoranz, A. Armada, C. Baixeras, J. A. Barrio, H. Bartko, D. Bastieri, J. K. Becker, W. Bednarek,

K. Berger, C. Bigongiari, A. Biland, R. K. Bock, P. Bordas, V. Bosch-Ramon, T. Bretz, I. Britvitch, M. Camara, E. Carmona, A. Chilingarian, J. A. Coarasa, S. Commichau, J. L. Contreras, J. Cortina, M. T. Costado, V. Curtef, V. Danielyan, F. Dazzi, A. De Angelis, C. Delgado, R. de los Reyes, B. De Lotto, E. Domingo-Santamaría, D. Dorner, M. Doro, M. Errando, M. Fagiolini, D. Ferenc, E. Fernández, R. Firpo, J. Flix, M. V. Fonseca, L. Font, M. Fuchs, N. Galante, R. García-López, M. Garczarczyk, M. Gaug, M. Giller, F. Goebel, D. Hakobyan, M. Hayashida, T. Hengstebeck, A. Herrero, D. Höhne, J. Hose, C. C. Hsu, P. Jacon, T. Jogler, R. Kosyra, D. Kranich, R. Kritzer, A. Laille, E. Lindfors, S. Lombardi, F. Longo, J. López, M. López, E. Lorenz, P. Majumdar, G. Maneva, K. Mannheim, O. Mansutti, M. Mariotti, M. Martínez, D. Mazin, C. Merck, M. Meucci, M. Meyer, J. M. Miranda, R. Mirzoyan, S. Mizobuchi, A. Moralejo, D. Nieto, K. Nilsson, J. Ninkovic, E. Oña-Wilhelmi, N. Otte, I. Oya, D. Paneque, M. Panniello, R. Paoletti, J. M. Paredes, M. Pasanen, D. Pascoli, F. Pauss, R. Pegna, M. Persic, L. Peruzzo, A. Piccioli, M. Poller, E. Prandini, N. Puchades, A. Raymers, W. Rhode, M. Ribó, J. Rico, M. Rissi, A. Robert, S. Rügamer, A. Saggion, A. Sánchez, P. Sartori, V. Scalzotto, V. Scapin, R. Schmitt, T. Schweizer, M. Shayduk, K. Shinozaki, S. N. Shore, N. Sidro, A. Sillanpää, D. Sobczynska, A. Stamerra, L. S. Stark, L. Takalo, P. Temnikov, D. Tescaro, M. Teshima, N. Tonello, D. F. Torres, N. Turini, H. Vankov, V. Vitale, R. M. Wagner, T. Wibig, W. Wittek, F. Zandanel, R. Zanin & J. Zapatero. *VHE γ-Ray Observation of the Crab Nebula and its Pulsar with the MAGIC Telescope.* ApJ, vol. 674, pages 1037–1055, February 2008.

[Aleksić 12] J. Aleksić, E. A. Alvarez, L. A. Antonelli, P. Antoranz, M. Asensio, M. Backes, J. A. Barrio, D. Bastieri, J. Becerra González, W. Bednarek, A. Berdyugin, K. Berger, E. Bernardini, A. Biland, O. Blanch, R. K. Bock, A. Boller, G. Bonnoli, D. Borla Tridon, I. Braun, T. Bretz, A. Cañellas, E. Carmona, A. Carosi, P. Colin, E. Colombo, J. L. Contreras, J. Cortina, L. Cossio, S. Covino, F. Dazzi, A. de Angelis, G. de Caneva, E. de Cea Del Pozo, B. de Lotto, C. Delgado Mendez, A. Diago Ortega, M. Doert, A. Domínguez, D. Dominis Prester, D. Dorner, M. Doro, D. Elsaesser, D. Ferenc, M. V. Fonseca, L. Font, C. Fruck, R. J. García López, M. Garczarczyk, D. Garrido, G. Giavitto, N. Godinović, D. Hadasch, D. Häfner, A. Herrero, D. Hildebrand, D. Höhne-Mönch, J. Hose, D. Hrupec, B. Huber, T. Jogler, H. Kellermann, S. Klepser, T. Krähenbühl, J. Krause, A. La Barbera, D. Lelas, E. Leonardo, E. Lindfors, S. Lombardi, M. López, A. López-Oramas, E. Lorenz, M. Makariev, G. Maneva, N. Mankuzhiyil, K. Mannheim, L. Maraschi, M. Mariotti, M. Martínez, D. Mazin, M. Meucci, J. M. Miranda, R. Mirzoyan, H. Miyamoto, J. Moldón, A. Moralejo, P. Munar-Adrover, D. Nieto, K. Nilsson, R. Orito, I. Oya, D. Paneque, R. Paoletti, S. Pardo, J. M. Paredes, S. Partini, M. Pasanen, F. Pauss, M. A. Perez-Torres, M. Persic, L. Peruzzo, M. Pilia, J. Pochon, F. Prada, P. G. Prada Moroni, E. Prandini, I. Puljak, I. Reichardt, R. Reinthal, W. Rhode, M. Ribó,

J. Rico, S. Rügamer, A. Saggion, K. Saito, T. Y. Saito, M. Salvati, K. Satalecka, V. Scalzotto, V. Scapin, C. Schultz, T. Schweizer, M. Shayduk, S. N. Shore, A. Sillanpää, J. Sitarek, I. Snidaric, D. Sobczynska, F. Spanier, S. Spiro, V. Stamatescu, A. Stamerra, B. Steinke, J. Storz, N. Strah, T. Surić, L. Takalo, H. Takami, F. Tavecchio, P. Temnikov, T. Terzić, D. Tescaro, M. Teshima, O. Tibolla, D. F. Torres, A. Treves, M. Uellenbeck, H. Vankov, P. Vogler, R. M. Wagner, Q. Weitzel, V. Zabalza, F. Zandanel & R. Zanin. *Performance of the MAGIC stereo system obtained with Crab Nebula data.* Astroparticle Physics, vol. 35, pages 435–448, February 2012.

[Aleksić 13] J. Aleksić, L. A. Antonelli, P. Antoranz, M. Asensio, U. Barres de Almeida, J. A. Barrio, J. Becerra González, W. Bednarek, K. Berger, E. Bernardini, A. Biland, O. Blanch, R. K. Bock, A. Boller, G. Bonnoli, D. Borla Tridon, T. Bretz, E. Carmona, A. Carosi, P. Colin, E. Colombo, J. L. Contreras, J. Cortina, L. Cossio, S. Covino, P. Da Vela, F. Dazzi, A. De Angelis, G. De Caneva, E. De Cea del Pozo, B. De Lotto, C. Delgado Mendez, A. Diago Ortega, M. Doert, D. Dominis Prester, D. Dorner, M. Doro, D. Eisenacher, D. Elsaesser, D. Ferenc, M. V. Fonseca, L. Font, C. Fruck, R. J. García López, M. Garczarczyk, D. Garrido Terrats, M. Gaug, G. Giavitto, N. Godinović, A. González Muñoz, S. R. Gozzini, A. Hadamek, D. Hadasch, D. Häfner, A. Herrero, J. Hose, D. Hrupec, B. Huber, F. Jankowski, T. Jogler, V. Kadenius, S. Klepser, M. L. Knoetig, T. Krähenbühl, J. Krause, J. Kushida, A. La Barbera, D. Lelas, E. Leonardo, N. Lewandowska, E. Lindfors, S. Lombardi, M. López, R. López-Coto, A. López-Oramas, E. Lorenz, M. Makariev, G. Maneva, N. Mankuzhiyil, K. Mannheim, L. Maraschi, B. Marcote, M. Mariotti, M. Martínez, D. Mazin, M. Meucci, J. M. Miranda, R. Mirzoyan, J. Moldón, A. Moralejo, P. Munar-Adrover, A. Niedzwiecki, D. Nieto, K. Nilsson, N. Nowak, R. Orito, S. Paiano, M. Palatiello, D. Paneque, R. Paoletti, J. M. Paredes, S. Partini, M. Persic, M. Pilia, J. Pochon, F. Prada, P. G. Prada Moroni, E. Prandini, I. Puljak, I. Reichardt, R. Reinthal, W. Rhode, M. Ribó, J. Rico, S. Rügamer, A. Saggion, K. Saito, T. Y. Saito, M. Salvati, K. Satalecka, V. Scalzotto, V. Scapin, C. Schultz, T. Schweizer, S. N. Shore, A. Sillanpää, J. Sitarek, I. Snidaric, D. Sobczynska, F. Spanier, S. Spiro, V. Stamatescu, A. Stamerra, B. Steinke, J. Storz, S. Sun, T. Surić, L. Takalo, H. Takami, F. Tavecchio, P. Temnikov, T. Terzić, D. Tescaro, M. Teshima, O. Tibolla, D. F. Torres, T. Toyama, A. Treves, M. Uellenbeck, P. Vogler, R. M. Wagner, Q. Weitzel, V. Zabalza, F. Zandanel, R. Zanin, N. Rea & M. Backes. *Observations of the magnetars 4U 0142+61 and 1E 2259+586 with the MAGIC telescopes.* A&A, vol. 549, page A23, January 2013.

[Atwood 09] W. B. Atwood, A. A. Abdo, M. Ackermann, W. Althouse, B. Anderson, M. Axelsson, L. Baldini, J. Ballet, D. L. Band, G. Barbiellini & et al. *The Large Area Telescope on the Fermi Gamma-Ray Space Telescope Mission.* ApJ, vol. 697, pages 1071–1102, June 2009.

[Bernlöhr 10] K. Bernlöhr. *CTA performance expected at 20 deg zenith angle*, 2010. http://www.mpi-hd.mpg.de/hfm/CTA/internal/MC/performance-20deg/.

[Şaşmaz Muş 10] S. Şaşmaz Muş & E. Göğüş. *Search for High-energy Gamma-ray Emission from an Anomalous X-ray Pulsar, 4U 0142+61.* ApJ, vol. 723, pages 100–103, November 2010.

[Camilo 06] F. Camilo, S. M. Ransom, J. P. Halpern, J. Reynolds, D. J. Helfand, N. Zimmerman & J. Sarkissian. *Transient pulsed radio emission from a magnetar.* Nature, vol. 442, pages 892–895, August 2006.

[Castro 12] D. Castro, P. Slane, D. C. Ellison & D. J. Patnaude. *Fermi-LAT Observations and a Broadband Study of Supernova Remnant CTB 109.* ApJ, vol. 756, page 88, September 2012.

[Cheng 01] K. S. Cheng & L. Zhang. *High-Energy Gamma-Ray Emission from Anomalous X-Ray Pulsars.* ApJ, vol. 562, pages 918–924, December 2001.

[Daum 97] A. et al. Daum. *First results on the performance of the HEGRA IACT array.* Astroparticle Physics, vol. 8, pages 1–2, December 1997.

[den Hartog 06] P. R. den Hartog, W. Hermsen, L. Kuiper, J. Vink, J. J. M. in't Zand & W. Collmar. *INTEGRAL survey of the Cassiopeia region in hard X rays.* A&A, vol. 451, pages 587–602, May 2006.

[den Hartog 08] P. R. den Hartog, L. Kuiper, W. Hermsen, V. M. Kaspi, R. Dib, J. Knödlseder & F. P. Gavriil. *Detailed high-energy characteristics of AXP 4U 0142+61. Multi-year observations with INTEGRAL, RXTE, XMM-Newton, and ASCA.* A&A, vol. 489, pages 245–261, October 2008.

[Duncan 92] R. C. Duncan & C. Thompson. *Formation of very strongly magnetized neutron stars - Implications for gamma-ray bursts.* ApJ, vol. 392, pages L9–L13, June 1992.

[et al 04] K. Tsuchiya et al. *Detection of Sub-TeV Gamma Rays from the Galactic Center Direction by CANGAROO-II.* Astrophys. J. Letters, vol. 606, pages L115–L118, May 2004.

[et al 06] J. Albert et al. *Observation of Gamma Rays from the Galactic Center with the MAGIC Telescope.* Astrophys. J., vol. 638, pages L101–L104, February 2006.

[Gavriil 02] F. P. Gavriil & V. M. Kaspi. *Long-Term Rossi X-Ray Timing Explorer Monitoring of Anomalous X-Ray Pulsars.* ApJ, vol. 567, pages 1067–1076, March 2002.

[Gonzalez 10] M. E. Gonzalez, R. Dib, V. M. Kaspi, P. M. Woods, C. R. Tam & F. P. Gavriil. *Long-term X-ray Changes in the Emission from the Anomalous X-ray Pulsar 4U 0142+61.* ApJ, vol. 716, pages 1345–1355, June 2010.

[Guenette 09] R. Guenette*et al. VERITAS Observations of Magnetars.* for the VERITAS Collaboration, in Proc. 31st ICRC (Łodz) (arXiv:0908.0717), August 2009.

[Hadasch 12] D. Hadasch, D. F. Torres, T. Tanaka, R. H. D. Corbet, A. B. Hill, R. Dubois, G. Dubus, T. Glanzman, S. Corbel, J. Li, Y. P. Chen, S. Zhang, G. A. Caliandro, M. Kerr, J. L. Richards, W. Max-Moerbeck, A. Readhead & G. Pooley. *Long-term Monitoring of the High-energy γ-Ray Emission from LS I +61° 303 and LS 5039.* ApJ, vol. 749, page 54, April 2012.

[Hadasch 13] D. Hadasch & Torres et al. *Long-term modulation of the gamma-ray emission from LS I +61° 303.* in prep., 2013.

[Hess 12] V. Hess. *Observation of Penetrating Radiation of seven Balloon Flights.* Physikalische Zeitschrift, vol. 13, page 1084, 1912.

[Hinton 09] J. A. Hinton & W. Hofmann. *Teraelectronvolt Astronomy.* ARA&A, vol. 47, pages 523–565, September 2009.

[Horns 05] D. Horns. *Tev gamma-radiation from Dark Matter annihilation in the Galactic center.* Physics Letters B, vol. 607, pages 225–232, 2005.

[Içdem 12] B. Içdem, A. Baykal & S. Ç. Inam. *RXTE timing analysis of the anomalous X-ray pulsar 1E 2259+586.* MNRAS, vol. 419, pages 3109–3114, February 2012.

[Israel 94] G. L. Israel, S. Mereghetti & L. Stella. *The discovery of 8.7 second pulsations from the ultrasoft X-ray source 4U 0142+61.* ApJ, vol. 433, pages L25–L28, September 1994.

[Israel 99] G. L. Israel, T. Oosterbroek, L. Angelini, S. Campana, S. Mereghetti, A. N. Parmar, A. Segreto, L. Stella, J. van Paradijs & N. E. White. *It BeppoSAX monitoring of the "anomalous" X-ray pulsar 4U 0142+61 SAX monitoring of the "anomalous" X-ray pulsar 4U 0142+61.* A&A, vol. 346, pages 929–935, June 1999.

[Israel 10] G. L. Israel, P. Esposito, N. Rea, S. Dall'Osso, F. Senziani, P. Romano, V. Mangano, D. Götz, S. Zane, A. Tiengo, D. M. Palmer, H. Krimm, N. Gehrels, S. Mereghetti, L. Stella, R. Turolla, S. Campana, R. Perna, L. Angelini & A. de Luca. *The 2008 October Swift detection of X-ray bursts/outburst from the transient SGR-like AXP 1E1547.0-5408.* MNRAS, vol. 408, pages 1387–1395, November 2010.

[Kaspi 03] V. M. Kaspi, F. P. Gavriil, P. M. Woods, J. B. Jensen, M. S. E. Roberts & D. Chakrabarty. *A Major Soft Gamma Repeater-like Outburst and Rotation Glitch in the No-longer-so-anomalous X-Ray Pulsar 1E 2259+586.* ApJ, vol. 588, pages L93–L96, May 2003.

[Kildea 07] J. Kildea, R. W. Atkins & H. M. et al. Badran. *The Whipple Observatory 10 m gamma-ray telescope, 1997 2006.* Astroparticle Physics, vol. 28, pages 182–195, October 2007.

[Kneiske 07] T. M. Kneiske. *Gamma-ray background: a review.* ArXiv e-prints, vol. 707, July 2007.

[Kosack et al 04] K. Kosack et al. *TeV Gamma-Ray Observations of the Galactic Center.* Astrophys. J., vol. 608, pages L97–L100, June 2004.

[Kouveliotou 98] C. Kouveliotou, S. Dieters, T. Strohmayer, J. van Paradijs, G. J. Fishman, C. A. Meegan, K. Hurley, J. Kommers, I. Smith, D. Frail & T. Murakami. *An X-ray pulsar with a superstrong magnetic field in the soft γ-ray repeater SGR1806 - 20.* Nature, vol. 393, pages 235–237, May 1998.

[Kuiper 06] L. Kuiper, W. Hermsen, P. R. den Hartog & W. Collmar. *Discovery of Luminous Pulsed Hard X-Ray Emission from Anomalous X-Ray Pulsars 1RXS J1708-4009, 4U 0142+61, and 1E 2259+586 by INTEGRAL and RXTE.* ApJ, vol. 645, pages 556–575, July 2006.

[Kulkarni 94] S. R. Kulkarni, D. A. Frail, N. E. Kassim, T. Murakami & G. Vasisht. *The radio nebula of the soft γ-ray repeater 1806 - 20.* Nature, vol. 368, pages 129–131, March 1994.

[Li 83] T.-P. Li & Y.-Q. Ma. *Analysis methods for results in gamma-ray astronomy.* ApJ, vol. 272, pages 317–324, September 1983.

[Li 11] J. Li, D. F. Torres, S. Zhang, Y. Chen, D. Hadasch, P. S. Ray, P. Kretschmar, N. Rea & J. Wang. *Long-term X-Ray Monitoring of LS I +61°303: Analysis of Spectral Variability and Flares.* ApJ, vol. 733, page 89, June 2011.

[Li 12] J. Li, D. F. Torres, S. Zhang, D. Hadasch, N. Rea, G. A. Caliandro, Y. Chen & J. Wang. *Unveiling the Super-orbital Modulation of LS I +61°303 in X-Rays.* ApJ, vol. 744, page L13, January 2012.

[Longair 92] M. S. Longair. High energy astrophysics, particles, photons and their detection, volume 1. Cambridge University Press, 2 edition, February 1992.

[Mazin 07] D. Mazin. *A study of very high energy gamma-ray emission from AGNs and constraints on the extragalactic background light.* PhD thesis, Technische Universität München, 2007.

[McGill Pulsar Group 12] McGill Pulsar Group. *McGill SGR/AXP Online Catalog*, June 2012. http://www.physics.mcgill.ca/~pulsar/magnetar/main.html.

[Mereghetti 95] S. Mereghetti & L. Stella. *The very low mass X-ray binary pulsars: A new class of sources?* ApJ, vol. 442, pages L17–L20, March 1995.

[Mereghetti 09] S. Mereghetti, D. Götz, G. Weidenspointner, A. von Kienlin, P. Esposito, A. Tiengo, G. Vianello, G. L. Israel, L. Stella, R. Turolla, N. Rea & S. Zane. *Strong Bursts from the Anomalous X-Ray Pulsar 1E 1547.0-5408 Observed with the INTEGRAL/SPI Anti-Coincidence Shield.* ApJ, vol. 696, pages L74–L78, May 2009.

[Moralejo 09] A. Moralejo, M. Gaug, E. Carmona, P. Colin, C. Delgado, S. Lombardi, D. Mazin, V. Scalzotto, J. Sitarek, D. Tescaro & for the MAGIC collaboration. *MARS, the MAGIC Analysis and Reconstruction Software.* in Proc. 31st ICRC (Łodz) (arXiv:0907.0943), July 2009.

[Paredes 13] J. M. Paredes, W. Bednarek, P. Bordas, V. Bosch-Ramon, E. De Cea del Pozo, G. Dubus, S. Funk, D. Hadasch, D. Khangulyan, S. Markoff, J. Moldón, P. Munar-Adrover, S. Nagataki, T. Naito, M. de Naurois, G. Pedaletti, O. Reimer, M. Ribó, A. Szostek, Y. Terada, D. F. Torres, V. Zabalza, A. A. Zdziarski & CTA Consortium. *Binaries with the eyes of CTA*. Astroparticle Physics, vol. 43, pages 301–316, March 2013.

[Patel 03] S. K. Patel, C. Kouveliotou, P. M. Woods, A. F. Tennant, M. C. Weisskopf, M. H. Finger, C. A. Wilson, E. Göğüş, M. van der Klis & T. Belloni. *Chandra Observations of the Anomalous X-Ray Pulsar 4U 0142+61*. ApJ, vol. 587, pages 367–372, April 2003.

[Rea 07a] N. Rea, E. Nichelli, G. L. Israel, R. Perna, T. Oosterbroek, A. N. Parmar, R. Turolla, S. Campana, L. Stella, S. Zane & L. Angelini. *Very deep X-ray observations of the anomalous X-ray pulsar 4U0142+614*. MNRAS, vol. 381, pages 293–300, October 2007.

[Rea 07b] N. Rea, R. Turolla, S. Zane, A. Tramacere, L. Stella, G. L. Israel & R. Campana. *Spectral Modeling of the High-Energy Emission of the Magnetar 4U 0142+614*. ApJ, vol. 661, pages L65–L68, May 2007.

[Rea 09] N. Rea, G. L. Israel, R. Turolla, P. Esposito, S. Mereghetti, D. Götz, S. Zane, A. Tiengo, K. Hurley, M. Feroci, M. Still, V. Yershov, C. Winkler, R. Perna, F. Bernardini, P. Ubertini, L. Stella, S. Campana, M. van der Klis & P. Woods. *The first outburst of the new magnetar candidate SGR0501+4516*. MNRAS, vol. 396, pages 2419–2432, July 2009.

[Rea 10a] N. Rea, P. Esposito, R. Turolla, G. L. Israel, S. Zane, L. Stella, S. Mereghetti, A. Tiengo, D. Götz, E. Göğüş & C. Kouveliotou. *A Low-Magnetic-Field Soft Gamma Repeater*. Science, vol. 330, pages 944–, November 2010.

[Rea 10b] N. Rea, D. F. Torres, M. van der Klis, P. G. Jonker, M. Méndez & A. Sierpowska-Bartosik. *Deep Chandra observations of TeV binaries - I. LS I +61° 303*. MNRAS, vol. 405, pages 2206–2214, July 2010.

[Rea 11] N. Rea, D. F. Torres, G. A. Caliandro, D. Hadasch, M. van der Klis, P. G. Jonker, M. Méndez & A. Sierpowska-Bartosik. *Deep Chandra observations of TeV binaries - II. LS 5039*. MNRAS, vol. 416, pages 1514–1521, September 2011.

[Rea 12] N. Rea, G. L. Israel, P. Esposito, J. A. Pons, A. Camero-Arranz, R. P. Mignani, R. Turolla, S. Zane, M. Burgay, A. Possenti, S. Campana, T. Enoto, N. Gehrels, E. Göğüş, D. Götz, C. Kouveliotou, K. Makishima, S. Mereghetti, S. R. Oates, D. M. Palmer, R. Perna, L. Stella & A. Tiengo. *A New Low Magnetic Field Magnetar: The 2011 Outburst of Swift J1822.3-1606*. ApJ, vol. 754, page 27, July 2012.

[Rea 13] N. Rea. *Magnetars: neutron stars with huge magnetic storms*. In IAU Symposium, volume 291 of *IAU Symposium*, pages 11–18, March 2013.

[Rolke 05] W. A. Rolke, A. M. López & J. Conrad. *Limits and confidence intervals in the presence of nuisance parameters*. Nuclear Instruments and Methods in Physics Research A, vol. 551, pages 493–503, October 2005.

[Rowell 11] G. Rowell*et al.* *Discovery of steady and extended TeV gamma-ray emission towards the magnetar SGR 1806-20 and stellar cluster C1 1806-20*. for the H.E.S.S. Collaboration, Phases of Late Stage Stellar Evolution, Macquarie Univ. Sydney 5-7 Dec. 2011, August 2011.

[Schönfelder 04] V. Schönfelder. *Lessons learnt from COMPTEL for future telescopes*. New A Rev., vol. 48, pages 193–198, February 2004.

[Sidro 08] N. Sidro. *Discovery and Characterization of the Binary System LSI +61303 in Very High Energy Gamma-Rays with MAGIC*. PhD thesis, 2008.

[Thompson 93] C. Thompson & R. C. Duncan. *Neutron star dynamos and the origins of pulsar magnetism*. ApJ, vol. 408, pages 194–217, May 1993.

[Thompson 95] C. Thompson & R. C. Duncan. *The soft gamma repeaters as very strongly magnetized neutron stars - I. Radiative mechanism for outbursts*. MNRAS, vol. 275, pages 255–300, July 1995.

[Thompson 96] C. Thompson & R. C. Duncan. *The Soft Gamma Repeaters as Very Strongly Magnetized Neutron Stars. II. Quiescent Neutrino, X-Ray, and Alfven Wave Emission*. ApJ, vol. 473, page 322, December 1996.

[Tong 11] H. Tong, L. M. Song & R. X. Xu. *Anomalous X-Ray Pulsars and Soft Gamma-Ray Repeaters in the Outer Gap Model: Confronting Fermi Observations*. ApJ, vol. 738, page 31, September 2011.

[Vink 06] J. Vink & L. Kuiper. *Supernova remnant energetics and magnetars: no evidence in favour of millisecond proto-neutron stars*. MNRAS, vol. 370, pages L14–L18, July 2006.

[Wakely 13] S. Wakely & D. Horan. *Catalog of detected VHE sources*, June 2013. http://tevcat.uchicago.edu/.

[Weekes 03] T. Weekes. Very High Energy Gamma-Ray Astronomy. Institute of Physics Publishing Bristol and Philadelphia, 2003.

[White 87] N. E. White, K. O. Mason, P. Giommi, L. Angelini, G. Pooley, G. Branduardi-Raymont, P. G. Murdin & J. V. Wall. *A 25 min modulation from the vicinity of the unusually soft X-ray source X0142+614*. MNRAS, vol. 226, pages 645–654, June 1987.

[Woods 04] P. M. Woods, V. M. Kaspi, C. Thompson, F. P. Gavriil, H. L. Marshall, D. Chakrabarty, K. Flanagan, J. Heyl & L. Hernquist. *Changes in the X-Ray Emission from the Magnetar Candidate 1E 2259+586 during Its 2002 Outburst*. ApJ, vol. 605, pages 378–399, April 2004.

[Woods 06] P. M. Woods & C. Thompson. Soft gamma repeaters and anomalous X-ray pulsars: magnetar candidates, pages 547–586. April 2006.

[Wu 13] J. H. K. Wu, C. Y. Hui, R. H. H. Huang, A. K. H. Kong, K. S. Cheng, J. Takata, P. H. T. Tam, E. M. H. Wu & C.-Y. Liu. *Pulsed γ-ray emission from magnetar 1E 2259+586.* In IAU Symposium, volume 291 of *IAU Symposium*, pages 555–557, March 2013.

[Zhang 97] L. Zhang & K. S. Cheng. *High-Energy Radiation from Rapidly Spinning Pulsars with Thick Outer Gaps.* ApJ, vol. 487, page 370, September 1997.

[Zhu 08] W. Zhu, V. M. Kaspi, R. Dib, P. M. Woods, F. P. Gavriil & A. M. Archibald. *The Long-term Radiative Evolution of Anomalous X-Ray Pulsar 1E 2259+586 After its 2002 Outburst.* ApJ, vol. 686, pages 520–527, October 2008.